# PADERBORN UNIVERSITY

# Exploring Roads to Functionality of Polaritons in Semiconductor Microcavities

Dissertation

submitted in partial fulfillment of the requirements for the degree of

Dr. rer. nat.

to the Department of Physics at Paderborn University, Germany

by Matthias Pukrop

Paderborn, January 2022

**Examination Board:**

Prof. Dr. Stefan Schumacher

Prof. Dr. Torsten Meier

Prof. Dr. Cedrik Meier

Dr. Uwe Gerstmann

Submitted on January 7, 2022.

# Abstract

Optoelectronic devices have become increasingly important in recent years due to possible applications in information processing and data communication. Accordingly, research activities towards functional photonic structures have increased. The Key point is the fundamental understanding of the underlying physics of the light-matter interaction. In this context, semiconductor microcavities turn out to be excellent platforms to study fundamental aspects of the light-matter interaction as well as to explore functional aspects for possible applications. In semiconductor microcavities light-matter quasiparticles arise due to a strong coupling between the cavity light field and the excitons (electron-hole pairs bound by Coulomb forces) in the semiconductor material. These hybrid quasiparticles are termed polaritons and are characterized by a small effective mass, a long coherence time, and strong repulsive interactions, rendering them experimentally accessible and well-suited to investigate nonlinear optical phenomena. This thesis focuses on three different functional aspects of polaritons in semiconductor microcavities. With the help of extensive numerical and analytical calculations, we explore application-driven configurations and reveal the underlying mechanisms.

In the first part, we investigate a recently proposed all-optical switching scheme in a resonantly excited spinor polariton fluid. This scheme is based on spatial pattern formation driven by polariton-polariton interactions. Besides numerical simulations that demonstrate the reversible on-demand process, we utilize a simplified population competition model to gather insight into the switching mechanism from a nonlinear dynamical systems perspective. We find that the simplified model has the form of a generalized Lotka-Volterra model extended with external control. Importantly, we perform a complete steady-state analysis and determine the phase boundaries in the relevant parameter subspace of the anisotropy and the external control. The dynamical behavior is characterized by representative trajectories in the state space. Importantly, all model parameters can be directly calculated from the physical quantities used in the numerical simulations, and we recover all key features of the all-optical switching scheme observed in the simulations.

In the second part, we investigate vortices in nonresonantly excited spinor polariton condensates. In semiconductor microcavities, a polariton vortex directly transfers its orbital angular momentum to the emitted light field. This additional degree of freedom

potentially enables applications in data storage and processing. We show that under ring-shaped excitation a rich multistability of various localized vortex states arises including so-called full-, spin-, and half-vortices. Importantly, we introduce a method to switch between different half-vortex states by applying a short resonant pulse. This all-optical switching method results in the reversal of the circular polarization peak in the half-vortex core.

In the last part, we focus on a more general characterization of polariton condensates in terms of potential applications in quantum-information tasks. Within a theory-experiment cooperation, we determine the quantum coherence of a polariton condensate under spatially broad excitation. The quantum coherence quantifies the amount of polariton number-state superpositions and represents a resource for quantum-information protocols. In agreement with the experiment, we find a significant amount of quantum coherence in the numerical simulations based on a phase-space formalism. Moreover, we find a way to enhance the quantum coherence by spatial pump shaping and we study the transition from a broad to a narrow excitation spot. Finally, we perform an explicit reconstruction of the system's density matrix in Fock space. We calculate the quantum coherence directly from the off-diagonal elements and demonstrate its temporal decay.

# Zusammenfassung

Optoelektronische Bauelemente gewannen in den letzten Jahren immer mehr an Bedeutung zwecks ihrer möglichen Anwendungen im Bereich Informationsverarbeitung und Datenkommunikation. Dementsprechend wuchsen die Forschungsaktivitäten mit einem Fokus auf funktionale photonische Strukturen. Der Schlüssel hierbei ist ein fundamentales Verständnis der zugrundeliegenden Licht-Materie Wechselwirkung. In diesem Zusammenhang haben sich Halbleitermikrokavitäten als exzellente Plattformen für die Untersuchung fundamentaler Aspekte der Licht-Materie Wechselwirkung sowie für die Erforschung funktionaler Aspekte herausgestellt. In Halbleitermikrokavitäten entstehen Licht-Materie Quasiteilchen aus der starken Kopplung zwischen dem Lichtfeld in der Kavität und den elektronischen Anregungen im Halbleitermaterial. Diese hybriden Quasiteilchen werden Polaritonen genannt und zeichnen sich durch eine kleine effektive Masse, eine lange Kohärenzzeit und starke repulsive Wechselwirkungen aus, was sie experimentell zugänglich und zudem gut geeignet für die Untersuchung nichtlinearen optischer Phänomene macht. Die vorliegende Arbeit konzentriert sich auf drei verschiedene funktionale Aspekte von Polaritonen in Halbleitermikrokavitäten. Mit der Hilfe von detaillierten numerischen und analytischen Berechnungen untersuchen wir anwendungsorientierte Konfigurationen und decken die zugrundeliegenden Mechanismen auf.

Im ersten Teil untersuchen wir einen kürzlich vorgeschlagenen rein-optischen Schalter in einem resonant angeregten Polariton System. Dieses Schalt-Schema basiert auf räumlicher Musterbildung, die von den nichtlinearen Wechselwirkungen der Polaritonen getrieben wird. Neben numerischen Simulationen, die den reversiblen Schaltvorgang demonstrieren, nutzen wir ein vereinfachtes Modell für die konkurrierenden Besetzungen der Muster, um Einblicke in den Schaltmechanismus aus der Perspektive nichtlinearer dynamischer Systeme zu bekommen. Dieses vereinfachte Modell hat die Form eines verallgemeinerten Lotka-Volterra Modells erweitert mit einer externen Kontrolle. Wir analysieren die stationären Zustände des Systems und bestimmen die Phasengrenzen im Parameterraum der Anisotropie und der externen Kontrolle. Das dynamische Verhalten wird durch representative Trajektorien im Zustandsraum charakterisiert. Die Modellparameter können direkt aus den physikalischen Größen der numerischen Simulationen berechnet werden und wir finden alle Schlüsselmerkmale des Schaltvorgangs aus den numerischen Simulationen

in dem vereinfachten Modell wieder.

Im zweiten Teil untersuchen wir Vortex Zustände in einem nicht-resonant angeregten Spinor Polariton Kondensat. In Halbleitermikrokavitäten führen Vortex Zustände zu endlichem Bahndrehimpuls des emittierten Lichts. Dieser zusätzliche Freiheitsgrad ermöglicht potentielle Anwendungen im Bereich der Datenspeicherung und -verarbeitung. Wir zeigen, dass unter einer ringförmigen Anregung eine reichhaltige Multistabilität verschiedener lokalisierter Vortex Zustände auftritt, inklusive Full-, Spin- und Half-Vortex Zuständen. Darüberhinaus führen wir eine Methode ein, um mithilfe eines resonanten Pulses zwischen verschiedenen Half-Vortex Zuständen reversibel zu schalten. Dieser ebenfalls rein-optische Schaltvorgang führt zu einer Umkehrung der zirkularen Polarisation innerhalb des Vortex Kerns.

Zuletzt fokussieren wir uns auf eine allgemeinere Charakterisierung von Polariton Kondensaten mit Hinblick auf mögliche Anwendungen im Bereich Quanteninformationstheorie. Innerhalb einer Theorie-Experiment Zusammenarbeit bestimmen wir die Quantenkohärenz eines Polariton Kondensats unter räumlich breiter Anregung. Die Quantenkohärenz quantifiziert die Menge an Fock-Zustand Superpositionen und stellt eine Quelle für Protokolle innerhalb der Quanteninformationsverarbeitung dar. In Übereinstimmung mit den experimentellen Ergebnissen finden wir ein signifikantes Maß an Quantenkohärenz in den numerischen Simulationen basierend auf einem Phasenraumformalismus. Darüberhinaus demonstrieren wir eine Methode zur Steigerung der Quantenkohärenz durch Variation des räumlichen Anregungsprofils. Desweiteren untersuchen wir den Übergang von einer räumlich breiten zu einer räumlich schmalen Anregung. Schließlich führen wir eine explizite Rekonstruktion der Dichtematrix im Fock Raum durch. Wir berechnen die Quantenkohärenz direkt aus den nicht-diagonal Elementen und demonstrieren ihr zeitliches Abklingen.

# Contents

# 1. Introduction

Living in a data-driven world has led to an all-encompassing focus on information and communication in our daily lives. The information technology sector is thriving with its dominating companies leading the markets all around the world. The sheer unlimited demand for new communication-based technologies has long found its impact into many different scientific research areas. The invention of the laser and advances in semiconductor fabrication have paved the way for possible applications based on nonlinear optical phenomena. A promising direction are light-based functional structures with the goal of step-wise replacing and expanding their traditional electrical-only counterparts. Optoelectronic devices play the important role of necessary light-matter interfaces with the potential of combining the best of both worlds. On the one hand, the light part enables optical excitation, signal transmission, and sensing. On the other hand, the matter part gives rise to various nonlinear phenomena. Together, both facets have been combined to unlock the application potential of photonic structures in recent years. This thesis focuses on functional aspects of polaritons in semiconductor microcavities. We explore three promising roads to functionality in the main chapters. Key starting point is the understanding of the underlying light-matter interaction on a fundamental level. To this end, we perform detailed numerical and analytical investigations.

Amongst the most versatile platforms to realize and investigate light-matter interaction phenomena are semiconductor microcavities [1]. With their broad implementation possibilities in terms of different material systems, experimental accessibility, and numerous linear and nonlinear optical effects, they have been studied extensively in the last three decades. Planar semiconductor microcavities commonly consist of a thin layer of semiconductor material embedded inside an optical resonator; see Fig. 1.1(a). The latter is usually realized with distributed Bragg reflectors (DBRs) which are planar structures made up of thin layers with alternating refractive indices. Light with its quarter-wavelength equal to the optical path length of each layer is efficiently reflected due to constructive interference of all partial reflections. The optical path length between the DBRs determines the possible resonant cavity modes. Here, we consider semiconductor microcavities where one or more quantum wells (QWs) are placed at the antinodes of the cavity light field as an optically active medium. A QW is a planar heterostructure where a thin semiconductor layer

is surrounded by material with a wider band gap leading to carrier confinement in one spatial direction. The latter gives rise to quantized energy sub bands. Within a single sub band, the system is effectively two-dimensional due to the remaining two spatial degrees of freedom. In a semiconductor QW electrons can be excited from the valence band into the conduction band by absorption of light with energies greater than the band gap. An excited electron in the conduction band can form a bound state with a missing electron in the valence band, effectively acting as a positively charged hole, via Coulomb interaction. The resulting quasiparticle states in semiconductors are termed Wannier-Mott excitons; referred to as just excitons in the following. Despite their strong formal analogy to the hydrogen atom, excitons are characterized by small binding energies $(1-100 \text{ meV})$ and large Bohr radii $(10-1000 \text{ Å})$ [1, p. 132]. Importantly, these material-specific values also depend on the dimension of the system. For the case of two-dimensional quantum wells, the exciton ground state is characterized by a four times higher binding energy and half of the Bohr radius compared to the three-dimensional case [2].

Placing a QW inside a microcavity, where the cavity mode is tuned spectrally close to the exciton resonance, enables the system to coherently transfer energy between its light and matter constituents by photon absorption (excitation of an exciton) and photon emission (recombination of an exciton); see sketch in Fig. 1.1(a). This light-matter coupling is proportional to the exciton dipole moment times the cavity field amplitude at the position of the QW. Additionally, if the coupling rates between photons and excitons exceed their decay rates, the system is in the strong-coupling regime where exciton-photon superpositions are the elementary excitations. This gives rise to the introduction of the exciton-polariton as a hybrid light-matter quasiparticle; referred to as just polariton in the following. The coupling leads to a normal-mode splitting in the dispersion relation into an upper and lower polariton branch as the system's new eigenstates; see Fig. 1.1(b). Following the theoretical works of Hopfield [3], Pekar [4], and Agranovich [5], the strong coupling was first experimentally observed in 1992 by Weisbuch et. al. [6]. Since then, a lot of efforts have been made to explore the peculiar properties of polaritons in semiconductor microcavities. Due to their photonic part, polaritons in semiconductor microcavities have very small effective masses usually about four orders of magnitude smaller than the free electron mass and lifetimes up to hundreds of picoseconds depending on the quality of the microcavity. Importantly, the light escaping from the cavity contains all information of the hybrid light-matter polariton state and ensures full experimental accessibility. Additionally, the photonic part enables external optical excitation of polaritons. The matter part gives rise to strong nonlinearities mediated by exciton-exciton scattering, and the resulting broad range of nonlinear effects are the fundamental basis of the different functional aspects of polaritons in semiconductor microcavities presented throughout this thesis. The polariton's polarization dependence, also referred to as the polariton's pseudospin
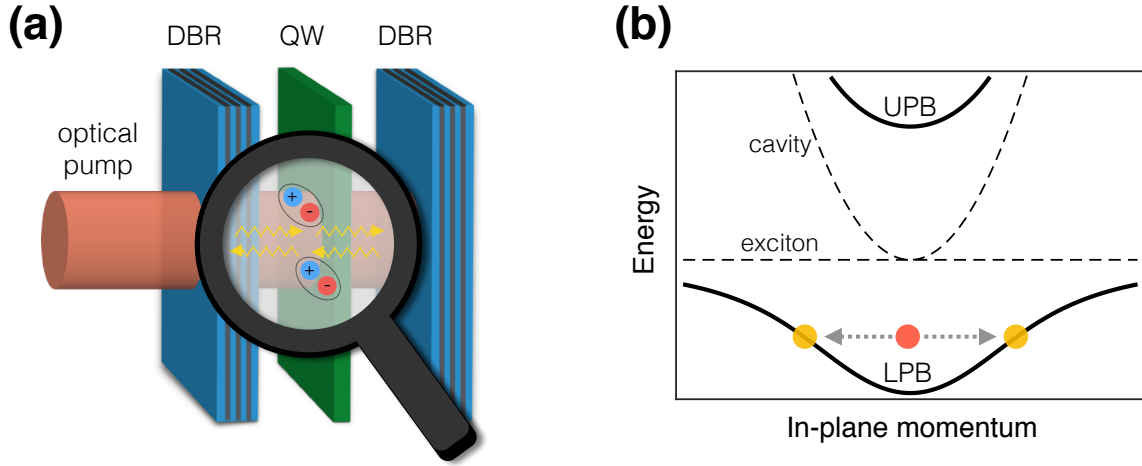
**Figure 1.1.** (a) Sketch of a planar semiconductor microcavity consisting of a quantum well (QW) embedded inside an optical resonator realized with distributed Bragg reflectors (DBRs). Schematically shown are the cavity light field and the QW excitons as bound electron-hole pairs. (b) Dispersion relation, i.e. energy as a function of the in-plane momentum. Dashed lines mark the bare cavity and exciton dispersion relations. Solid lines show the normal-mode splitting into an upper (UPB) and lower polariton branch (LPB) that arises from the strong light-matter coupling. Also sketched is an example of an optical parametric oscillator configuration where two pump polaritons (red) at zero in-plane momentum slightly above the minimum of the lower polariton branch scatter into signal and idler polaritons (yellow) on the dispersion with opposite momenta.

structure, stems from the polarization within the light part as well as the spin within the matter part. In this thesis we consider two-dimensional GaAs structures in the limit where the 1s-heavy-hole exciton is the dominant excitation. The latter has spin projections $m_J = \pm 2, \pm 1$ of which only the $\pm 1$ transitions are optically active and can be excited by $\sigma^\pm$ circularly polarized light. Thus, the polaritons inherit a two-component spinor character. With the polarization dependence mainly come two effects: (i) In the linear regime the splitting of the cavity dispersion for TE/TM-polarized modes introduces a momentum-dependent coupling between opposite circular polarization components, and (ii) in the nonlinear regime spin-dependent exciton-exciton interaction can possibly lead to attractive interactions between opposite circularly polarized polaritons. The interplay of polarization-dependent effects leads to numerous intriguing phenomena, e.g. the optical spin Hall effect [7,8], half-vortices [9], polarization-dependent spatial anisotropy of polariton amplification [10], and the nonlinear optical spin Hall effect [11]; see also Ref. [12] for a detailed review. In this thesis we also investigate various effects based on the polariton's polarization dependence. To this end, the proper tools have to be selected. In Chapter 2 we review a few relevant properties of polaritons and present the theoretical framework of the different models we use to describe the polariton's dynamical behavior under different excitation conditions throughout the thesis.

Many important phenomena observed for polaritons in semiconductor microcavities are

based on phase-matched wave-mixing processes of coherent polariton fields in the vicinity of the lower polariton branch. These processes are also commonly interpreted as energy- and momentum-conserving polariton scattering. Exciting a semiconductor microcavity resonantly slightly above the minimum of the lower polariton branch enables different optical parametric oscillator configurations. For example, if the incident pump field impinges onto the cavity under the so-called magic angle, which refers to the inflection point of the lower polariton branch, phase-matched four-wave mixing processes can lead to a strong signal field at the zero-momentum ground state and an idler field at twice the pump's momentum [13–15]; see also Ref. [16] for a review. Another example uses a pump field at normal incidence, i.e. at zero in-plane momentum, slightly above the minimum of the lower polariton branch; see Fig. 1.1(b). Here, above a certain excitation threshold, four-wave mixing processes result in strong signal and idler fields at opposite in-plane momenta resonantly scattered onto the lower polariton branch. At sufficiently large densities the circular symmetry is spontaneously broken, and stationary patterns with a reduced symmetry arise, which are visible in the far-field emission of the microcavity [17, 18]. Various applications based on these optical parametric oscillator configuration of polaritons have been proposed and experimentally demonstrated, e.g. low-intensity all-optical switching [19], spontaneous formation and control of spatiotemporal patterns [17], generation of two strongly correlated beams [20], and transfer of orbital angular momentum [21]. Recently, a method for directional transistor-like switching of two-spot patterns under linearly polarized excitation was proposed [22]. In Chapter 3 we study in depth the pattern competition dynamics that arise in the aforementioned switching scheme. The underlying mechanism is based on the polarization-dependent spatial anisotropy. The focus of our investigation is to gather further insight into the switching dynamics with the help of a simplified population competition model. For the latter a complete steady-state and bifurcation analysis is done from a nonlinear dynamical systems perspective to reveal the key features of the switching process.

Another striking phenomenon is condensation of polaritons in semiconductor microcavities under incoherent excitation. The macroscopic coherent occupation of the ground state excited by a nonresonant pump was experimentally demonstrated [23, 24], and has led to many interesting studies since then; see Refs. [25, 26] for detailed reviews. Being a distinct bosonic feature, condensation of polaritons indicates their bosonic character. Note that in the low-excitation limit where the mean distance of excitons is much larger than their Bohr radius, they can be approximated as bosons. In this regime, the resulting microcavity polaritons are also characterized as bosonic quasiparticles since they are a superposition of photon and exciton. However, this approximation is not valid in the general case, and it neglects various effects due to the fermionic constituents [27]. In the incoherent excitation scheme, the pump is far above the exciton resonance and excites free

carriers which form excitons and relax down to the lower polariton branch via phonon emission creating an excitonic reservoir. From the latter, a fraction of polaritons scatters down to the ground state at zero in-plane momentum via stimulated polariton-polariton scattering, building up a macroscopic coherent condensate. Because of the finite lifetime of polaritons, the system needs constant pumping. Thus, in contrast to atomic Bose-Einstein condensates (BEC), a polariton condensate is intrinsically out of equilibrium. Nevertheless, if a balance between gain and loss is achieved, a stationary quasi-equilibrium state is reached. Owing to the photonic part, the very small effective polariton mass enables possible condensation at room temperatures [28–30], which is an advantage over conventional BECs in terms of experiments and applications. Due to both the similarities and the differences to conventional BECs, polariton condensates provide a platform to study properties of quantum phases in two-dimensional driven-dissipative systems. For example, a Berezinskii–Kosterlitz–Thouless (BKT) transition characterized by a power-law decay of the first-order spatial coherence was experimentally and numerically reported [31–35]. The BKT transition involves the unbinding of bound vortex-antivortex pairs. A vortex is a phase defect with a density minimum in the center and a circular movement around the core known in numerous physical systems. In polariton condensates a vortex results in finite orbital angular momentum of the emitted light. In order to exploit this additional degree of freedom in terms of functionality, reliable formation and control of vortices in polariton condensates is required. A necessary prerequisite is the creation of a spatially localized condensate at a desired target position. To this end, various methods of spatial potential engineering to trap polariton condensates at a predefined location can be utilized; see Ref. [36] for a review. A versatile trapping method is to utilize the optically pump-induced potential experienced by the polaritons. We employ this method in Chapter 4 where we investigate localized vortices under nonresonant ring-shaped excitation. We study the multistability of various vortex states including the polariton's polarization dependence. Importantly, the latter provides a mechanism to switch between different vortex states using a resonant control beam.

With the recent focus on quantum applications, polaritons as a prominent light-matter system are studied with increasing interest regarding also their quantum properties [37–42]. Importantly, due to their hybrid nature, polaritons provide a platform to probe the underlying matter system for quantum superpositions by analyzing the emitted light via quantum optical measurements. Recently, together with coworkers we established an interdisciplinary access to polariton condensates combining quantum-information theory, numerical simulations, and quantum optical measurements. The results were published in the joint work Ref. [43], and they are discussed in detail as part of Chapter 5. Adapting a general concept from quantum-information science, we investigate the quantum coherence of a polariton condensates, and hence determine its resourcefulness regarding quantum-

information tasks. The quantum coherence complements common coherence measures, such as first- and second-order correlation functions, and allows a more general characterization of quantum features within polariton condensates. We employ a phase-space method to determine the quantum coherence in different spatial excitation geometries, and explicitly reconstruct the system's density matrix in Fock space. Additionally, we dynamically track the decay of coherence indicated by the decreasing off-diagonal matrix elements.

# 2. Theoretical framework

In this chapter we lay down the theoretical framework developed and used to describe polaritons in semiconductor microcavities and discuss general properties of the strong coupling regime. We briefly review the derivation of the equations of motion for different types of excitation conditions which provide the platform for our analytical investigations and numerical simulations.

## 2.1. Semiclassical model for resonant excitation

In this section we introduce a semiclassical model to describe the dynamics of resonantly excited polaritons in planar semiconductor microcavities. It is based on a classical description of the light field passing through the structure via Maxwell's equations within a transfer matrix formalism and a microscopic description of the exciton polarization in the quantum well via semiconductor Bloch equations. Finally, these descriptions lead to a set of coupled dynamical equations for the coherent light-matter interaction inside the semiconductor microcavity which then can be solved numerically. First, we neglect the photonic polarization degree of freedom and the excitonic spin degree of freedom for clarity. We re-include and discuss this aspect at the end of this section.

Starting with the propagation of the light field, we follow the derivation given in Ref. [44]. For nearly normal incidence and an infinitely thin planar cavity located in the $xy$-plane at $z = 0$, the wave equation for the external electric field $\mathcal{E}(\mathbf{r}, t)$ passing through the microcavity structure can be denoted as

$$\frac{n_s}{c^2} \partial_t^2 \mathcal{E}(\mathbf{r}, t) - \nabla^2 \mathcal{E}(\mathbf{r}, t) = \frac{\hbar t_c \delta(z)}{\epsilon_0 c^2} \partial_t^2 E(\mathbf{r}, t), \tag{2.1}$$

where $E(\mathbf{r}, t)$ is the internal cavity field which couples to the external field via the coupling constant $t_c$. Furthermore, $n_s$ is the refractive index of the substrate, $c$ is the vacuum speed of light, $\epsilon_0$ is the vacuum dielectric constant, and $\hbar$ is the reduced Planck constant. Expanding the external field and cavity field in momentum space and separating the incident, transmitted, and reflected field components relates the internal cavity field to

the external field by [44]

$$E_{\mathbf{k},\text{trans}} = E_{\mathbf{k},\text{inc}} - E_{\mathbf{k},\text{refl}}, \tag{2.2}$$

$$E_{\mathbf{k},\text{refl}} = -\frac{\hbar t_c}{2\epsilon_0 c n_s}\partial_t E_{\mathbf{k}}. \tag{2.3}$$

Note that $\mathbf{k} \equiv (k_x, k_y)$ denotes the in-plane momentum from here on. The transmitted field $E_{\mathbf{k},\text{trans}}$ is the part of the external field which is present at the location of the cavity. Assuming a much higher pump frequency $\omega_p$ than the variation of the envelope in time allows us to approximate $\partial_t E_{\mathbf{k}} \approx -i\omega_p E_{\mathbf{k}}$ and further write $E_{\mathbf{k},\text{trans}} = E_{\mathbf{k},\text{inc}} + \frac{i\hbar\omega_p t_c}{2\epsilon_0 c n_s}E_{\mathbf{k}}$. Hence, the equation of motion for the cavity field including an external source term and coupling to the exciton polarization $p_{\mathbf{k}}$ is postulated as [44]

$$i\hbar\partial_t E_{\mathbf{k}} = \hbar\omega_{\mathbf{k}} E_{\mathbf{k}} - \Omega p_{\mathbf{k}} + \hbar t_c E_{\mathbf{k},\text{trans}}, \tag{2.4}$$

where $\hbar\omega_{\mathbf{k}}^c$ is the cavity dispersion and $\Omega$ describes the coupling between the cavity field and exciton polarization and it is assumed to be constant; see details further below. The square modulus $|E_{\mathbf{k}}|^2$ can be interpreted as photon density for a given mode $\mathbf{k}$. Identifying $\gamma_c/\hbar \equiv \frac{\hbar\omega_p t_c^2}{2\epsilon_0 c n_s}$ as the cavity decay rate and $E_{\mathbf{k},\text{pump}} \equiv \hbar t_c E_{\mathbf{k},\text{inc}}$ as the external pump field finally leads to the following equation of motion for the cavity field

$$i\hbar\partial_t E_{\mathbf{k}} = (\hbar\omega_{\mathbf{k}} - i\gamma_c)E_{\mathbf{k}} - \Omega p_{\mathbf{k}} + E_{\mathbf{k},\text{pump}}. \tag{2.5}$$

Due to the planar geometry, the system becomes effectively two-dimensional. The confinement in the $z$-direction leads to a discrete mode $k_z$, whereas the in-plane momentum $\mathbf{k} = (k_x, k_y)$ remains continuous; we drop the preceding adjective "in-plane" in the following. For excitation in nearly normal incidence (small $|\mathbf{k}|$) the cavity dispersion can be expanded as [1]

$$\hbar\omega_{\mathbf{k}} = \frac{\hbar c}{n_b k_z}\sqrt{1 + \frac{|\mathbf{k}|^2}{k_z^2}} \approx \frac{\hbar c}{2n_b k_z}\left(1 + \frac{|\mathbf{k}|^2}{k_z^2}\right) \equiv \hbar\omega_{\mathbf{0}} + \frac{\hbar^2|\mathbf{k}|^2}{2m_c}, \tag{2.6}$$

where $n_b$ is the background refractive index of the cavity material, $m_c = \hbar n_b k_z/c$ is the effective photon mass and $\hbar\omega_{\mathbf{0}} = \hbar k_z c/n_b$ is the zero-momentum energy.

The optically induced exciton polarization in a quantum well can be described microscopically via semiconductor Bloch equations [2,45]. Here we only give a very brief overview of the main results. The starting point is a many-particle Hamiltonian

$$\hat{H} = \hat{H}_{\text{e}} + \hat{H}_{\text{h}} + \hat{H}_{\text{C}} + \hat{H}_{\text{lm}}, \tag{2.7}$$

which consists of the energies of electrons in the conduction band and holes in the valence band, their Coulomb interaction, and the light-matter coupling. The individual terms are explicitly given by

$$\hat{H}_{\mathrm{e}} = \sum_{\mathbf{k}} E_{\mathrm{e},\mathbf{k}} \hat{c}_{\mathbf{k}}^{\dagger} \hat{c}_{\mathbf{k}}, \tag{2.8}$$

$$\hat{H}_{\mathrm{h}} = \sum_{\mathbf{k}} E_{\mathrm{h},\mathbf{k}} \hat{d}_{-\mathbf{k}}^{\dagger} \hat{d}_{-\mathbf{k}}, \tag{2.9}$$

where $\hat{c}_{\mathbf{k}}$ ($\hat{d}_{-\mathbf{k}}$) is the electron (hole) annihilation operator at momentum $\mathbf{k}$ ($-\mathbf{k}$) and $E_{\mathrm{e/h},\mathbf{k}}$ is the band structure,

$$\hat{H}_{\mathrm{C}} = \frac{1}{2} \sum_{\mathbf{k},\mathbf{k'},\mathbf{q}\neq\mathbf{0}} V_{\mathbf{q}} \left( \hat{c}_{\mathbf{k}+\mathbf{q}}^{\dagger} \hat{c}_{\mathbf{k'}-\mathbf{q}}^{\dagger} \hat{c}_{\mathbf{k'}} \hat{c}_{\mathbf{k}} + \hat{d}_{\mathbf{k}+\mathbf{q}}^{\dagger} \hat{d}_{\mathbf{k'}-\mathbf{q}}^{\dagger} \hat{d}_{\mathbf{k'}} \hat{d}_{\mathbf{k}} - 2\hat{c}_{\mathbf{k}+\mathbf{q}}^{\dagger} \hat{d}_{\mathbf{k'}-\mathbf{q}}^{\dagger} \hat{d}_{\mathbf{k'}} \hat{c}_{\mathbf{k}} \right), \tag{2.10}$$

where $V_{\mathbf{q}}$ is the Fourier transform of the Coulomb potential, and

$$\hat{H}_{\mathrm{lm}} = \sum_{\mathbf{q},\mathbf{k}} E_{\mathbf{q}} \left( \mu_{\mathrm{eh}} \hat{c}_{\mathbf{k}+\mathbf{q}}^{\dagger} \hat{d}_{-\mathbf{k}}^{\dagger} + \mathrm{h.c.} \right), \tag{2.11}$$

where $E_{\mathbf{q}}$ is the cavity field and $\mu_{\mathrm{eh}}$ is the projection of the interband dipole matrix element on the polarization vector of the cavity field. The dipole matrix element is assumed to be momentum independent. The dynamical evolution of a given observable $\hat{A}$ which is stationary in the Schrödinger picture is described by the Heisenberg equation of motion

$$i\hbar \partial_t \hat{A} = \left[ \hat{A}, \hat{H} \right]. \tag{2.12}$$

Here, we assume a low-excitation regime with exciton densities on the order of $10^{10}$ cm$^{-2}$ or smaller, and a near-resonant excitation where contributions of the $1s$ heavy-hole exciton to the interband polarization are dominant. In this approximation, the interband polarization in the exciton basis reads [44, 46]

$$p_{\mathbf{q}} = \sum_{\mathbf{k}} \phi_{1s}(\mathbf{k} + \beta\mathbf{q}) \left\langle \hat{d}_{-\mathbf{k}} \hat{c}_{\mathbf{k}+\mathbf{q}} \right\rangle, \tag{2.13}$$

where $\phi_{1s}$ is the two-dimensional $1s$ excitonic wave function and $\beta = m_{\mathrm{h}}/(m_{\mathrm{h}} + m_{\mathrm{e}})$ with electron and hole masses $m_{\mathrm{e}}$, $m_{\mathrm{h}}$. Evaluating the Heisenberg equation leads to a hierarchy problem [47] in the Coulomb-interaction part, because the time evolution of the 2-point-operator expectation value couples to the 4-point-operator expectation value et cetera. To tackle this problem, a common approach is the so-called "dynamics-controlled truncation scheme" (DCT), which is based on a expansion in powers of the excitation light field [46–48]. This approximation method is valid in the low-excitation regime in the

coherent limit and allows to calculate a closed set of equations for the desired nonlinear response order. For the moment, we restrict the investigation to the $\chi^{(3)}$ Hartree-Fock level and correlations beyond mean-field will be included further below where we discuss the polarization degree of freedom. For our semiconductor microcavity system, the equation of motion for the exciton polarization $p_{\mathbf{k}}$ in the $\chi^{(3)}$ regime in Hartree-Fock approximation reads [44, 46]

$$i\hbar\partial_t p_{\mathbf{k}} = (\epsilon_{\mathbf{k}}^x - i\gamma_e)p_{\mathbf{k}} - \Omega E_{\mathbf{k}} + \sum_{\mathbf{k}',\mathbf{k}''} p_{\mathbf{k}'+\mathbf{k}''-\mathbf{k}}^* p_{\mathbf{k}'}(\alpha_{\mathrm{PSF}}\Omega E_{\mathbf{k}''} + V_{\mathrm{HF}} p_{\mathbf{k}''}), \qquad (2.14)$$

where $\epsilon_{\mathbf{k}}^x \equiv \epsilon_{\mathbf{0}}^x + \frac{\hbar^2 k^2}{2m_x}$ is the exciton dispersion with $\epsilon_{\mathbf{0}}^x$ being the zero-momentum energy. Compared to the photonic dispersion, Eq. (2.6), it is approximately flat $\epsilon_{\mathbf{k}}^x \approx \epsilon_{\mathbf{0}}^x$ for small values of $|\mathbf{k}|$ since the exciton mass is much larger than the effective photon mass $m_x \gg m_c$. In the following, we also refer to $p_{\mathbf{k}}$ as the coherent exciton field and interpret the square modulus $|p_{\mathbf{k}}|^2$ as exciton density for a given mode $\mathbf{k}$. Moreover, $\gamma_e/\hbar$ is a phenomenologically added decay rate representing all nonradiative losses of the coherent exciton field. The coupling between the cavity and exciton field is explicitly given by [44]

$$\Omega = \phi_{1s}^*(\mathbf{r}{=}\mathbf{0})\mu_{eh}f_\gamma(0)\sqrt{\hbar\omega_{\mathbf{k}}/\epsilon_0\epsilon_b}, \qquad (2.15)$$

where $f_\gamma(0)$ is the photon wave function at $z = 0$ (QW plane) and $\epsilon_b$ is the permittivity of the cavity material. This coupling is assumed to be a constant parameter in the following. The third-order nonlinearity describes all phase-matched scattering processes stemming from two interactions: (i) repulsive Hartree-Fock Coulomb interaction $V_{\mathrm{HF}}$, which describes the exciton-exciton scattering on a mean-field level and (ii) repulsive (for the considered spectral range) phase-space filling interaction $\alpha_{\mathrm{PSF}}$, which describes Pauli blocking due to the fermionic nature of the electrons and holes. These two system parameters are given explicitly in the $1s$ heavy-hole exciton limit by [46] $V_{\mathrm{HF}} = 2\pi(1 - \frac{315\pi^2}{4096})a_0^2 E_b^{(2D)}$ and $\alpha_{\mathrm{PSF}} = \frac{\sqrt{32\pi}}{7}a_0$, where $a_0$ is the excitonic Bohr radius and $E_b^{(2D)}$ the two-dimensional exciton binding energy.

In summary, the coupled Equations (2.5) and (2.14) self-consistently describe the coherent light-matter interaction of a semiconductor microcavity within a semiclassical formalism. The linearized coupled equations of motion without decay read

$$i\hbar\partial_t \begin{pmatrix} E_{\mathbf{k}} \\ p_{\mathbf{k}} \end{pmatrix} = \begin{pmatrix} \hbar\omega_{\mathbf{k}} & -\Omega \\ -\Omega & \epsilon_{\mathbf{k}}^x \end{pmatrix} \begin{pmatrix} E_{\mathbf{k}} \\ p_{\mathbf{k}} \end{pmatrix}. \qquad (2.16)$$

The light-matter coupling yields a normal-mode splitting of the dispersion relation into two branches: The upper polariton branch (UPB) and the lower polariton branch (LPB)

which are given by the eigenvalues of the matrix defined in Eq. (2.16)

$$E^{\text{UPB}}_{\text{LPB}}(\mathbf{k}) = \frac{1}{2}\left(\hbar\omega_{\mathbf{k}} + \epsilon^x_{\mathbf{k}}\right) \pm \sqrt{\frac{1}{4}\left(\hbar\omega_{\mathbf{k}} + \epsilon^x_{\mathbf{k}}\right)^2 + \Omega^2}. \tag{2.17}$$

Figure 2.1 shows both UPB and LPB alongside the bare exciton and cavity dispersion for
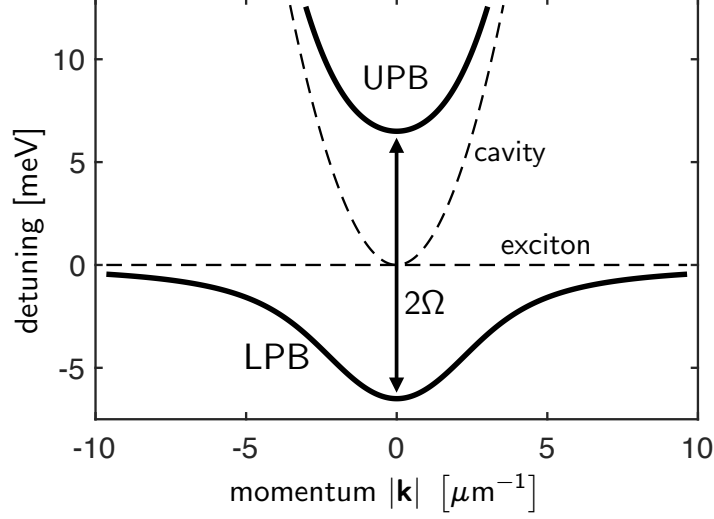


**Figure 2.1.** Polariton normal-mode splitting. Solid lines show upper (UPB) and lower polariton branch (LPB). At $\mathbf{k} = \mathbf{0}$ both branches are split by $2\Omega$. Dashed lines mark bare cavity and exciton dispersion. Parameters are $\Omega = 6.5$ meV, $\epsilon^x_{\mathbf{0}} = 0$, and $m_c = 3.78 \times 10^{-5} m_e$ where $m_e$ is the free electron mass.

the resonant case where cavity and exciton dispersion coincide at $\mathbf{k} = \mathbf{0}$. In that case, the energy splitting at zero momentum is given by $2\Omega$. While being approximately parabolic around $\mathbf{k} = \mathbf{0}$, the LPB becomes more excitonic at higher $k$-values which leads to its characteristic shape with an inflection point. In general, cavity and exciton dispersion can be detuned against each other and the transformation into the polariton eigenbasis reads

$$\begin{pmatrix} \psi^{\text{LPB}}_{\mathbf{k}} \\ \psi^{\text{UPB}}_{\mathbf{k}} \end{pmatrix} = \begin{pmatrix} X_{\mathbf{k}} & C_{\mathbf{k}} \\ -C_{\mathbf{k}} & X_{\mathbf{k}} \end{pmatrix} \begin{pmatrix} E_{\mathbf{k}} \\ p_{\mathbf{k}} \end{pmatrix}, \tag{2.18}$$

where the squared moduli of the Hopfield coefficients [3] correspond to the excitonic and photonic fractions which constitute the polariton and explicitly read

$$|X_{\mathbf{k}}|^2 = \frac{1}{2}\left(1 + \frac{\delta_{\mathbf{k}}}{\sqrt{\delta^2_{\mathbf{k}} + 4\Omega^2}}\right), \tag{2.19}$$

$$|C_{\mathbf{k}}|^2 = \frac{1}{2}\left(1 - \frac{\delta_{\mathbf{k}}}{\sqrt{\delta^2_{\mathbf{k}} + 4\Omega^2}}\right), \tag{2.20}$$

with detuning $\delta_{\mathbf{k}} \equiv \epsilon_{\mathbf{k}}^x - \hbar\omega_{\mathbf{k}}$ and normalization condition $|X_{\mathbf{k}}|^2 + |C_{\mathbf{k}}|^2 = 1$. As a result, with positive (negative) detuning polaritons become more excitonic (photonic). In the nonlinear regime a blueshift of the polariton energies can be observed due to repulsive Coulomb and phase-space filling interactions. Importantly, the nonlinearity mediated by the exciton-exciton and phase-space filling interactions gives rise to various phase-matched wave-mixing processes of coherent polariton fields. These processes are the focus of Chapter 3 where polariton pattern formation due to four-wave mixing is studied.

All numerical simulations in the present work are performed in real space. To this end, we additionally Fourier transform both Eqs. (2.5) and (2.14) to obtain the coupled set of equations of motion to describe the light-matter interaction of a semiconductor microcavity in real space

$$i\hbar\partial_t E(\mathbf{r}, t) = (H_c - i\gamma_c)E(\mathbf{r}, t) - \Omega p(\mathbf{r}, t) + E_{\text{pump}}(\mathbf{r}, t), \qquad (2.21)$$

$$i\hbar\partial_t p(\mathbf{r}, t) = (H_e - i\gamma_e)p(\mathbf{r}, t) - \Omega(1 - \alpha_{\text{PSF}}|p(\mathbf{r}, t)|^2)E(\mathbf{r}, t) + V_{\text{HF}}|p(\mathbf{r}, t)|^2 p(\mathbf{r}, t), \quad (2.22)$$

where $H_c = \hbar\omega_0 - \frac{\hbar^2}{2m_c}\nabla^2$ is the cavity Hamiltonian and $H_e = \epsilon_{\mathbf{0}}^x$ is the exciton Hamiltonian. Details of the numerical implementation are given in Appendix A.

So far, we have neglected the excitonic spin degree of freedom and the photonic polarization degree of freedom. This scalar case describes approximately (exact for zero TE-TM splitting) the dynamics of circularly polarized excitation where only co-circularly polarized photons and exciton are excited. The scalar model no longer holds, if the excitation is linearly polarized. In this case, polarization-dependent effects can strongly alter the dynamics which has to be accounted for in the equations of motion. The polariton polarization dependence is determined by its constituents. The two circular polarizations $\sigma^{\pm}$ of the light field couple to the $J = \pm 1$ exciton spin states [1]. In the following we always refer to the polarization degree of freedom for both the excitonic spin and the photonic vectorial polarization due to their one-to-one correspondence. The polarization dependence enters our model of the light-matter interaction in two ways: (i) TE-TM polarization splitting of the cavity modes in the linear regime and (ii) polarization-dependent exciton-exciton scattering in the nonlinear regime. Due to the different penetration depth inside the distributed Bragg mirrors for the TE- and TM-mode [49], they show slightly different dispersion relations, which can be characterized by two different effective masses with $m_{\text{TE}} > m_{\text{TM}}$. In other words, the effective polariton mass becomes polarization-dependent. Figure 2.2(a) shows the excitation geometry of the semiconductor microcavity. The plane of incidence defines the TE-TM basis in the two-dimensional cavity plane, as marked by the colored unit vectors $\mathbf{e}_{\text{TE}}^{\|}$ and $\mathbf{e}_{\text{TM}}^{\|}$. Figure 2.2(b) shows additionally the in-plane view of the system where $\varphi_{\mathbf{k}}$ is the angle between the $x$-axis and the in-plane component of
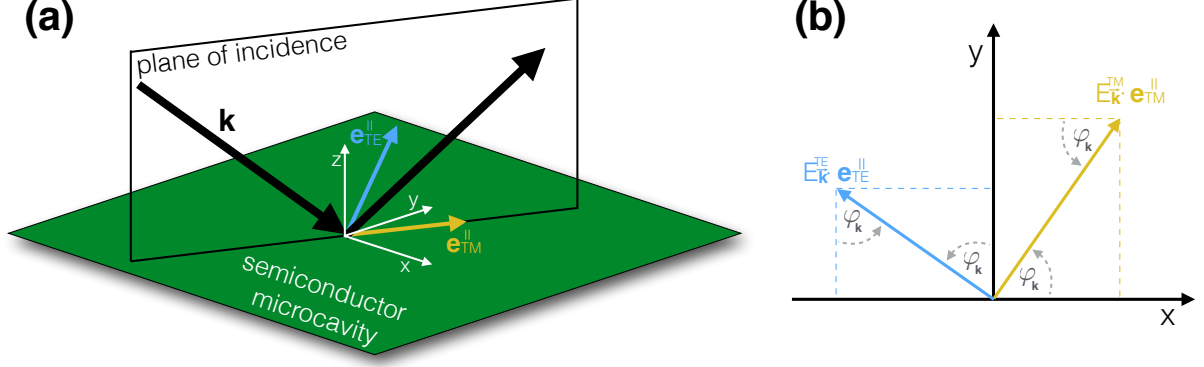
**Figure 2.2.** (a) Excitation geometry of the semiconductor microcavity. (b) Corresponding in-plane view and definition of the angle $\varphi_{\mathbf{k}}$ between the $x$-axis and the in-plane component of the incident light field. Adapted from Ref. [50].

incident mode $\mathbf{k}$. Hence, the in-plane cavity field additionally becomes two-component in the TE-TM polarization space $E_{\mathbf{k}} = (E_{\mathbf{k}}^{\text{TM}}, E_{\mathbf{k}}^{\text{TE}})^T$. The time evolution of each component is then given by Eq. (2.5) but with the different effective masses. In order to change the polarization basis to the linear $(xy)$ and the circular $(\pm)$ basis we use the definitions made in Fig. 2.2 to obtain the following transformations

$$\begin{pmatrix} E_{\mathbf{k}}^+ \\ E_{\mathbf{k}}^- \end{pmatrix} = \frac{1}{\sqrt{2}} \begin{pmatrix} e^{-i\varphi_{\mathbf{k}}} & -ie^{-i\varphi_{\mathbf{k}}} \\ e^{i\varphi_{\mathbf{k}}} & ie^{i\varphi_{\mathbf{k}}} \end{pmatrix} \begin{pmatrix} E_{\mathbf{k}}^{\text{TM}} \\ E_{\mathbf{k}}^{\text{TE}} \end{pmatrix} \quad \text{and} \quad \begin{pmatrix} E_{\mathbf{k}}^x \\ E_{\mathbf{k}}^y \end{pmatrix} = \frac{1}{\sqrt{2}} \begin{pmatrix} 1 & 1 \\ i & -i \end{pmatrix} \begin{pmatrix} E_{\mathbf{k}}^+ \\ E_{\mathbf{k}}^- \end{pmatrix}, \quad (2.23)$$

where we have used the definition of left-circular and right-circular polarized light $E_{\mathbf{k}}^{\pm} = (E_{\mathbf{k}}^x \mp iE_{\mathbf{k}}^y)/\sqrt{2}$. Applying these transformations, the equation of motion for the cavity field in the circular polarization basis reads

$$i\hbar\partial_t E_{\mathbf{k}}^{\pm} = (\hbar\omega_{\mathbf{k}} - i\gamma_c)E_{\mathbf{k}}^{\pm} + \Delta_{\mathbf{k}}^{\pm}E_{\mathbf{k}}^{\mp} - \Omega p_{\mathbf{k}}^{\pm} + E_{\mathbf{k},\text{pump}}^{\pm}, \quad (2.24)$$

where $\hbar\omega_{\mathbf{k}} = \hbar\omega_0 + \frac{\hbar^2 k^2}{4}\left(\frac{1}{m_{\text{TM}}} + \frac{1}{m_{\text{TE}}}\right)$ is the dispersion with averaged effective masses. In the circular polarization basis an additional term appears due to the TE-TM splitting which couples the two components via $\Delta_{\mathbf{k}}^{\pm} = \frac{\hbar^2}{4}\left(\frac{1}{m_{\text{TM}}} - \frac{1}{m_{\text{TE}}}\right)(k_x \mp ik_y)^2$ which leads to polarization coupling. The polarization dependence of the exciton-exciton scattering was investigated in Ref. [46] within a $T$-Matrix formalism. For excitation frequencies in the vicinity of the LPB minimum it was shown that the real part of the scattering matrix element for co-circularly polarized excitons is positive whereas it is negative for cross-circularly polarized excitons. Their imaginary parts are negligible in this regime. Thus, including the polarization degree of freedom induces a new attractive interaction between cross-circularly polarized excitons besides the repulsive interaction between co-circularly polarized excitons. The equation of motion for the exciton field including all two-exciton correlations, Hartree-Fock Coulomb

interaction, and phase-space filling within the $\chi^{(3)}$-DCT scheme in the circular polarization basis reads

$$
\begin{aligned}
i\hbar\partial_t p_{\mathbf{k}}^{\pm} =& (\epsilon_{\mathbf{k}}^x - i\gamma_e)p_{\mathbf{k}}^{\pm} - \Omega E_{\mathbf{k}}^{\pm} + \Omega\alpha_{\mathrm{PSF}}\sum_{\mathbf{k}',\mathbf{k}''} p_{\mathbf{k}'+\mathbf{k}''-\mathbf{k}}^{\pm*}p_{\mathbf{k}'}^{\pm}E_{\mathbf{k}''}^{\pm} \\
&+ \sum_{\mathbf{k}',\mathbf{k}''}(T^{++}p_{\mathbf{k}'+\mathbf{k}''-\mathbf{k}}^{\pm*}p_{\mathbf{k}'}^{\pm}p_{\mathbf{k}''}^{\pm} + T^{+-}p_{\mathbf{k}'+\mathbf{k}''-\mathbf{k}}^{\mp*}p_{\mathbf{k}'}^{\mp}p_{\mathbf{k}''}^{\pm}),
\end{aligned}
\tag{2.25}
$$

where $T^{++} > 0$ and $T^{+-} < 0$ are the scattering matrix elements for co- and cross-circularly polarized excitons. Their time dependence and therefore corresponding time retardation effects are neglected because they are assumed constant in the spectral range considered here. Again, for the purpose of numerical implementation, we transform Eqs. (2.24) and (2.25) into real space to obtain

$$
i\hbar\partial_t E^{\pm}(\mathbf{r}, t) = (H_c - i\gamma_c)E^{\pm}(\mathbf{r}, t) + H^{\pm}E^{\mp}(\mathbf{r}, t) - \Omega p^{\pm}(\mathbf{r}, t) + E_{\mathrm{pump}}^{\pm}(\mathbf{r}, t),
\tag{2.26}
$$

$$
\begin{aligned}
i\hbar\partial_t p^{\pm}(\mathbf{r}, t) =& (H_e - i\gamma_e)p^{\pm}(\mathbf{r}, t) - \Omega(1 - \alpha_{\mathrm{PSF}}|p^{\pm}(\mathbf{r}, t)|^2)E^{\pm}(\mathbf{r}, t) \\
&+ T^{++}|p^{\pm}(\mathbf{r}, t)|^2 p^{\pm}(\mathbf{r}, t) + T^{+-}|p^{\mp}(\mathbf{r}, t)|^2 p^{\pm}(\mathbf{r}, t),
\end{aligned}
\tag{2.27}
$$

where $H_c = \hbar\omega_0 - \frac{\hbar^2}{4}(\frac{1}{m_{\mathrm{TM}}} + \frac{1}{m_{\mathrm{TE}}})\nabla^2$ is the cavity Hamiltonian, $H^{\pm} = -\frac{\hbar^2}{4}(\frac{1}{m_{\mathrm{TM}}} - \frac{1}{m_{\mathrm{TE}}})(\partial_x \mp i\partial_y)^2$ is the TE-TM splitting operator and $H_e = \epsilon_{\mathbf{0}}^x$ is the the exciton Hamiltonian. In Chapter 3 the model defined by Eqs. (2.26 2.27) is used to describe a switching scheme of orthogonal two-spot patterns under resonant linearly polarized excitation. Furthermore, the full model serves as starting point for the derivation of a simplified model, which is used to further investigate the underlying mechanisms from a nonlinear dynamical systems perspective.

## 2.2. Gross-Pitaevskii model for nonresonant excitation

In the previous section we derived a model for polaritons resonantly excited in the vicinity of the LPB minimum. For the dynamics of polariton condensates which form under nonresonant excitation a different description is needed. For this purpose, it is advantageous to switch to the polariton picture via the unitary transformation given by Eq. (2.18) in the previous section. We define $\psi(\mathbf{r}, t) \equiv \psi^{\mathrm{LPB}}(\mathbf{r}, t)$ which describes the coherent polariton field at the bottom of the LPB. In the case of zero detuning $\delta_{\mathbf{0}} = 0$ at $\mathbf{k} = \mathbf{0}$, the transformation reads $\psi = (E + p)/\sqrt{2}$.

For the investigations of polariton condensates in Chapter 4 and 5, we assume a nonresonant pump far above the exciton resonance. The excited free carriers can form excitons and relax down to the lower polariton branch via exciton-phonon interactions, creating a
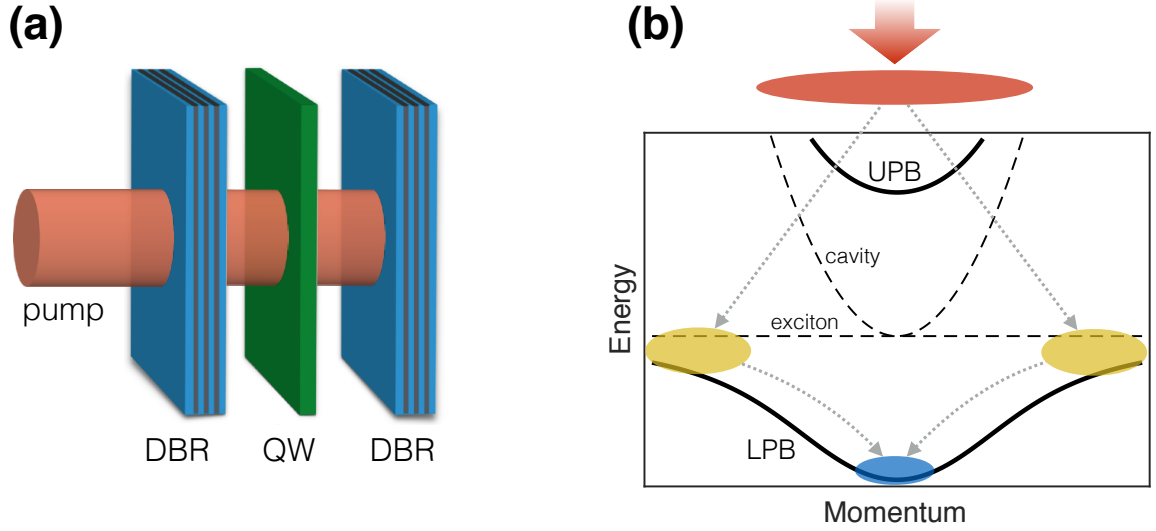
**Figure 2.3.** (a) Sketch of a semiconductor microcavity consisting of distributed Bragg reflectors (DBR) and a quantum well (QW) excited by a pump beam. (b) Schematic representation of the polariton condensation process. A nonresonant pump (red) far above the LPB excites free electrons and holes which form excitons. By phonon emission the excitons relax down to the bottleneck region of the LPB creating a reservoir (yellow). From the reservoir stimulating scattering into the ground state builds up a coherent polariton condensate (blue). Adapted from Ref. [43].

reservoir at the so-called bottleneck region. In this region polaritons accumulate due to their long relaxation times compared to their lifetimes. From this reservoir stimulated scattering of polaritons into the ground state at zero in-plane momentum builds up a macroscopic coherent condensate. Because of the finite lifetime of polaritons, the system needs constant pumping to maintain the condensate. So in contrast to atomic condensates, a polariton condensate is intrinsically out of equilibrium. To account for nonresonant excitation conditions, the model is phenomenologically extended with an equation of motion for the incoherent reservoir density $n_{\text{res}}(\mathbf{r}, t)$. The resulting driven-dissipative spinor Gross-Pitaevskii (GP) equation coupled to the density of the incoherent reservoir in circular polarization basis reads [11, 51]

$$
i\hbar\partial_t \Psi_\pm = \left[ H - \frac{i\hbar}{2}\gamma_c + g_c|\Psi_\pm|^2 - g_x|\Psi_\mp|^2 + \left( g_r + \frac{i\hbar}{2}R \right) n_{\text{res},\pm} \right] \Psi_\pm + H^\pm \Psi_\mp + E_\pm,
$$

(2.28)

$$
\partial_t n_{\text{res},\pm} = \left( -\gamma_r - R|\Psi_\pm|^2 \right) n_{\text{res},\pm} + P_\pm,
$$

(2.29)

and has been successfully used to describe various experiments [11, 52–56]. Here we omitted the space and time dependence for better visibility. The role of the reservoir in this model is two-fold. It replenishes the condensate mediated by the condensation rate $Rn_{\text{res},\pm}$ to mimic the stimulated in-scattering of polaritons and also acts as an optically induced repulsive potential $g_r n_{\text{res},\pm}$. These two processes are proportional to the constants $R$ and $g_r$,

respectively. The reservoir itself is fed by the nonresonant pump $P_\pm(\mathbf{r}, t)$ and it is depleted by the condensate density through the spatial hole-burning effect $-R|\Psi_\pm|^2 n_{\mathrm{res},\pm}$ [51]. Hence, the condensate formation depends on the spatial distribution of the nonresonant pump mediated by the reservoir density. This opens up many possibilities for creating and controlling different polariton condensate states and their properties by spatial pump shaping [36, 56–58] as we demonstrate in Chapters 4 and 5. Furthermore, $H = -\frac{\hbar^2}{2m_{\mathrm{eff}}}\nabla^2$ is the free particle Hamiltonian with the effective polariton mass $m_{\mathrm{eff}}$; $\gamma_c$ and $\gamma_r$ are the decay rates of the condensate and the reservoir. The interaction strength between co- and cross-circularly polarized polaritons are given by $g_c$ and $g_{\mathrm{x}}$, respectively. $H^\pm = \Delta_{\mathrm{LT}}\left(i\partial_x \pm \partial_y\right)^2$ is the TE-TM splitting operator. $E_\pm$ represents and optional resonant external beam. It was shown that similar models can also be derived from a density matrix formalism [59] (see Sec. 2.3) and from quantum kinetics via a Keldysh-Green formalism [60]. Note that we assume a polarized reservoir here, which transfers the polarization state to the condensate. This assumption is valid for linearly polarized excitation and is frequently used in both theoretical and experimental works [11, 52, 53, 61, 62]. In Chapter 4, this spinor GP model is applied to study localized vortex states under nonresonant linearly polarized excitation.

## 2.3. Truncated Wigner approximation

In order to study statistical and quantum properties of polariton condensates in Chapter 5, we use the truncated Wigner approximation for Bose gases [63, 64], a phase-space method which incorporates fluctuations on top of the mean field solution and allows to calculate relevant expectation values. The general idea is to use the Wigner representation for a bosonic polariton field operator. Starting with a master equation for the system's density matrix, the dynamics are transformed to the time evolution of the corresponding Wigner function via a Wigner-Weyl transformation. The time evolution of the Wigner distribution can then be truncated and mapped onto a set of stochastic partial differential equations for the complex-valued phase-space variables. The latter can be used to sample the phase space and calculate expectation values. In this section, we present a short derivation mainly based on Ref. [59]. A mathematical rigorous derivation can be found in Ref. [65].

The starting point is the bosonic polariton field operator $\hat{\psi}(\mathbf{r})$ which is defined on a finite two-dimensional spatial grid of length $L$, sampled by $N^2$ discrete points, and satisfies the commutation relation

$$\left[\hat{\psi}(\mathbf{r}), \hat{\psi}^\dagger(\mathbf{r}')\right] = \frac{\delta_{\mathbf{r}\mathbf{r}'}}{\Delta V}, \tag{2.30}$$

where $\mathbf{r} \equiv \mathbf{r}_i$, $i \in \{1, ..., N^2\}$ denotes a discrete grid point and $\Delta V = L^2/N^2$ denotes the unit cell volume. Physically, we describe the same system of nonresonant excitation as presented in the previous Sec. 2.2. Again, the dynamics are separated into coupled

descriptions for the low-energy condensate modes and a rate equation for the high-energy reservoir. Neglecting the polarization degree of freedom and suppressing the spatial argument $\hat{\psi} \equiv \hat{\psi}(\mathbf{r})$ the Hamiltonian density in second quantization for LPB polaritons can be written as [26]

$$\hat{H} = \int d\mathbf{r} \left[ \hat{\psi}^{\dagger} \left( -\frac{\hbar^2}{2m} \Delta + g_r n_{\mathrm{res}} \right) \hat{\psi} + \frac{g_c}{2} \hat{\psi}^{\dagger} \hat{\psi}^{\dagger} \hat{\psi} \hat{\psi} \right], \qquad (2.31)$$

where we assume a parabolic dispersion relation, a local interaction potential and a repulsive potential term proportional to $g_r n_{\mathrm{res}}$ due to the condensate-reservoir interaction. The dynamic evolution in time of the corresponding density matrix $\hat{\rho}$ is then given by the master equation

$$\frac{\partial \hat{\rho}}{\partial t} = -\frac{i}{\hbar} \left[ \hat{H}, \hat{\rho} \right] + \int d\mathbf{r} \, \mathcal{L}[\hat{\rho}], \qquad (2.32)$$

where gain and loss mediated through net reservoir in-scattering $R n_{\mathrm{res}}$ and cavity losses $\gamma_c$ are modeled by the following Lindblad terms

$$\mathcal{L}[\hat{\rho}] = \frac{R n_{\mathrm{res}}}{2} \left( 2\hat{\psi}^{\dagger} \hat{\rho} \hat{\psi} - \hat{\psi} \hat{\psi}^{\dagger} \hat{\rho} - \hat{\rho} \hat{\psi} \hat{\psi}^{\dagger} \right) + \frac{\gamma_c}{2} \left( 2\hat{\psi} \hat{\rho} \hat{\psi}^{\dagger} - \hat{\psi}^{\dagger} \hat{\psi} \hat{\rho} - \hat{\rho} \hat{\psi}^{\dagger} \hat{\psi} \right). \qquad (2.33)$$

Here, we assume a simplified form of the amplification rate $R n_{\mathrm{res}}$ where $R$ is constant [66]. A more sophisticated modeling of the reservoir-condensate in- and out-scattering was done in Ref. [59].

In order to map the problem onto phase space, the next step is a functional Wigner-Weyl transformation of the master equation (2.32). The transformation of the density matrix $\mathcal{W}[\hat{\rho}]$ results in the Wigner functional

$$W[\psi, \psi^*] = \frac{1}{\pi^2} \int \delta^2\lambda \, \exp \left[ \int d\mathbf{r}(-\lambda\psi^* + \lambda^*\psi) \right] \mathrm{tr} \left\{ \hat{\rho} \, \exp \left[ \int d\mathbf{r} \, (\lambda\hat{\psi}^{\dagger} - \lambda^*\hat{\psi}) \right] \right\}, \tag{2.34}$$

where $\psi(\mathbf{r})$ and $\psi^*(\mathbf{r})$ are complex functions that correspond to the field operators $\hat{\psi}(\mathbf{r})$ and $\hat{\psi}^{\dagger}(\mathbf{r})$. These complex amplitudes span the phase space and are referred to as phase-space variables. Expectation values of field operator products in symmetric ordering can be calculated using the Wigner functional as a weight (optical equivalence theorem)

$$\left\langle \left( \hat{\psi}^{\dagger m} \hat{\psi}^n \right)_{\mathrm{sym}} \right\rangle = \int \delta^2\psi \, \psi^{*m} \psi^n \, W[\psi, \psi^*]. \qquad (2.35)$$

Hence, the Wigner functional is commonly interpreted as a quasi-probability distribution. To keep the derivation clear, we transform the master equation (2.32) term by term using

the following transformation rules [65]

$$\mathcal{W}[\hat{\psi}\hat{\rho}] = \left(\psi + \frac{\delta}{2\delta\psi^*}\right)W, \quad \mathcal{W}[\hat{\psi}^\dagger\hat{\rho}] = \left(\psi^* - \frac{\delta}{2\delta\psi}\right)W,$$

$$\mathcal{W}[\hat{\rho}\hat{\psi}] = \left(\psi - \frac{\delta}{2\delta\psi^*}\right)W, \quad \mathcal{W}[\hat{\rho}\hat{\psi}^\dagger] = \left(\psi^* + \frac{\delta}{2\delta\psi}\right)W. \tag{2.36}$$

The commutator of the linear part of the Hamiltonian density $L = \left(-\frac{\hbar^2}{2m}\Delta + g_r n_{\text{res}}\right)$ including the kinetic and potential term transforms as

$$\mathcal{W}\left[\int d\mathbf{r} \ \left[\hat{\psi}^\dagger L\hat{\psi}, \hat{\rho}\right]\right] = \int d\mathbf{r} \ \left(-\frac{\delta}{\delta\psi}L\psi + \frac{\delta}{\delta\psi^*}L\psi^*\right)W, \tag{2.37}$$

where we have used the following relations [65]

$$\mathcal{W}\left[\int d\mathbf{r} \ [\hat{\psi}^\dagger\Delta\hat{\psi}, \hat{\rho}]\right] = \int d\mathbf{r} \ \left(-\frac{\delta}{\delta\psi}\Delta\psi + \frac{\delta}{\delta\psi^*}\Delta\psi^*\right)W, \tag{2.38}$$

$$\psi\frac{\delta}{\delta\psi}W = \left(\frac{\delta}{\delta\psi}\psi - \frac{1}{\Delta V}\right)W. \tag{2.39}$$

The nonlinear part of the commutator can be transformed using Eq. (2.39), resulting in

$$\mathcal{W}\left[\int d\mathbf{r} \ \frac{g_c}{2} \left[\hat{\psi}^\dagger\hat{\psi}^\dagger\hat{\psi}\hat{\psi}, \hat{\rho}\right]\right] = \int d\mathbf{r} \ g_c\left[\frac{\delta}{\delta\psi}\left(-|\psi|^2\psi + \frac{1}{\Delta V}\psi\right) + \frac{\delta}{\delta\psi^*}\left(|\psi|^2\psi^* - \frac{1}{\Delta V}\psi^*\right)\right.$$

$$\left. + \frac{1}{4}\frac{\delta^2}{\delta\psi\delta\psi^*}\left(\frac{\delta}{\delta\psi}\psi - \frac{\delta}{\delta\psi^*}\psi^*\right)\right]W. \tag{2.40}$$

The gain and loss part transform as follows using the relations given in Eqs. (2.39) and (2.36)

$$\mathcal{W}\left[\int d\mathbf{r} \ \mathcal{L}_{\text{gain}}[\hat{\rho}]\right] = \int d\mathbf{r} \ \frac{Rn_{\text{res}}}{2} \left[-\frac{\delta}{\delta\psi}(\psi W) - \frac{\delta}{\delta\psi^*}(\psi^*W) + \frac{\delta^2}{\delta\psi\delta\psi^*}W\right], \tag{2.41}$$

$$\mathcal{W}\left[\int d\mathbf{r} \ \mathcal{L}_{\text{loss}}[\hat{\rho}]\right] = \int d\mathbf{r} \ \frac{\gamma_c}{2} \left[\frac{\delta}{\delta\psi}(\psi W) + \frac{\delta}{\delta\psi^*}(\psi^*W) + \frac{\delta^2}{\delta\psi\delta\psi^*}W\right], \tag{2.42}$$

where $\mathcal{L}_{\text{gain}}$ and $\mathcal{L}_{\text{loss}}$ are defined as the first and second summand on the right-hand side of Eq. (2.33). Adapting to the finite spatial grid, we substitute $\int d\mathbf{r} \to \Delta V \sum_{\mathbf{r}}$ and $\frac{\delta}{\delta\psi} \to \frac{1}{\Delta V}\frac{\partial}{\partial\psi}$ to finally obtain the time evolution of the Wigner function

$$\frac{\partial W}{\partial t} = \sum_{\mathbf{r}} \left[-\frac{\partial}{\partial\psi}f + \frac{\partial}{\partial\psi^*}f^* + \frac{Rn_{\text{res}} + \gamma_c}{2\Delta V}\frac{\partial^2}{\partial\psi\partial\psi^*} + \frac{ig_c}{4\Delta V^2\hbar}\frac{\partial^2}{\partial\psi\partial\psi^*}\left(\frac{\partial}{\partial\psi^*}\psi^* - \frac{\partial}{\partial\psi}\psi\right)\right]W,$$

$$\tag{2.43}$$

where $f$ is given by

$$f = -\frac{i}{\hbar}\left(-\frac{\hbar^2}{2m}\Delta + g_r n_{\text{res}} + \frac{i\hbar}{2}(Rn_{\text{res}} - \gamma_c) + g_c|\psi|^2_-\right)\psi, \tag{2.44}$$

and $|\psi|^2_- = |\psi|^2 - \Delta V^{-1}$ denotes the renormalized density. If we neglect the third-order derivatives, Equation (2.43) resembles a Fokker-Planck equation with drift and diffusion, and therefore can be mapped onto a set of stochastic differential equations for the corresponding phase-space variables

$$d\psi = fdt + dW, \tag{2.45}$$

where the noise term $dW$ is a complex-valued Wiener process with correlations

$$\langle dW(\mathbf{r})dW(\mathbf{r}')\rangle = 0$$
$$\langle dW(\mathbf{r})dW^*(\mathbf{r}')\rangle = (Rn_{\text{res}} + \gamma_c)\frac{\delta_{\mathbf{rr}'}dt}{2\Delta V}. \tag{2.46}$$

Similarly to Sec. 2.2, the dynamics of the reservoir density can be added phenomenologically by the rate equation

$$\frac{\partial n_{\text{res}}}{\partial t} = (-\gamma_r - R|\psi|^2_-)n_{\text{res}} + P. \tag{2.47}$$

Equations (2.45) and (2.47) are simultaneously solved in time for many realizations to approximate expectation values as stochastic averages. In the limit $dW \to 0$, $|\psi|^2_- \to |\psi|^2$, the model resembles a scalar mean-field Gross-Pitaevskii equation coupled to an incoherent reservoir [51]. To justify the truncation of the third-order derivatives, we compare the prefactors of the second- and third-order derivatives and conclude that this approximation should be appropriate for cases where

$$\gamma_c \gg \frac{g_c}{\Delta V \hbar}. \tag{2.48}$$

In principle, the truncation condition restricts this method to cases of much larger dissipation in the system compared to the interaction strength per unit cell. Therefore, it might not be suitable to describe effects based on strong quantum correlations [64]. Nevertheless, the truncated Wigner approximation has been successfully used in various fields to report on effects beyond mean-field approximations, e.g. quantum noise in trapped Bose-Einstein condensates [67], quantum correlations of signal-idler emission in the ring-shaped luminescence of resonantly excited semiconductor microcavities [68], ferromagnetic domain formation in spinor Bose-Einstein condensates [69], analogs of black-hole Hawking radiation processes in a polariton fluid [70], and also critical exponents [34], the Kibble-Zurek mechanism [71], and the Berezinskii-Kosterlitz-Thouless phase transition [33] in

polariton condensates. In Chapter 5 the truncated Wigner model is used to study quantum coherence of polariton condensates under various spatial excitation conditions. With the help of Monte-Carlo techniques, relevant expectation values are calculated. Additionally, we explicitly reconstruct the density matrix in Fock space from the sampled Wigner phase-space distribution via pattern functions.

# 3. Externally controlled Lotka-Volterra dynamics in a spinor polariton fluid

Recently increased research activities towards all-optical components follow the high demand of functional optoelectronic devices for operation in optical communication networks. Integrated optical circuits are based on fundamental operations in analogy to electric circuits, where one of the most prominent operation is transistor-like switching. Various systems have been investigated as possible platforms for efficient all-optical switching, e.g. rubidium vapor [72], organic photonic crystals [73], photonic crystal nanocavities on a silicon chip [74], and quantum dots in photonic-crystal defect cavities [75]. The accessibility together with a low-intensity threshold, renders polaritons in semiconductor microcavities promising candidates for all-optical switching methods [17, 19, 44, 76, 77]. The first stop on the road to different functionalities for polaritons in semiconductor microcavities is an all-optical switching method in a spinor polariton fluid. It is based on a transverse pattern formation process caused by modulation instabilities which are driven by four-wave mixing processes between the coherent polariton fields. Spatiotemporal pattern formation in general has received a lot of research attention due to its broad occurrence throughout nature; see Ref. [78] for a detailed review. The origin of the pattern formation process of the polariton system at hand lies in the exciton-exciton scattering due to Coulomb interaction and Pauli blocking; see Sec. 2.1. Under certain excitation conditions, an initially homogeneous density in real space can become unstable against small periodic density fluctuations. The corresponding modes in $k$-space experience huge growth driven by four-wave mixing feedback loops, and hence spontaneously break the system's transverse symmetry. This modulation instability can result in a stable stationary pattern with a reduced symmetry determined by the underlying dominant scattering processes. The resulting patterns can be directly observed in the far-field emission of the cavity. Importantly, the emerging patterns can be manipulated by an external resonant control beam in terms of stability and orientation for example.

For the polariton system under investigation, it was found that pumping slightly above the LPB minimum at zero in-plane momentum can lead to hexagonal patterns due to the cubic order of the relevant scattering processes [18, 44, 79, 80]. The orientation of

the hexagon in $k$-space generally depends on the initial fluctuations, and hence appears random. However, it might be pinned at a fixed angle in the presence of a finite sample disorder potential. Importantly, for linearly polarized excitation, it was shown that the orientation of the hexagonal pattern aligns with the pump's polarization plane [18]. In the presence of directional anisotropy realized by tilting the pump slightly away from normal incidence for example, stable two-spot patterns are found instead of full hexagons [18, 22]. This has been exploited for all-optical transistor-like switching of two-spot patterns [22]. Recently, the polarization-dependent orientation of two-spot patterns was used to realize beam steering as a polariton lighthouse effect [81].

In this chapter we analyze the recently proposed all-optical switching scheme of two-spot patterns [22], which is based on the polariton's polarization dependence, from a nonlinear dynamical systems perspective. To this end, we present a simplified population competition (PC) model which treats the two-spot patterns in $k$-space as two competing and interacting populations. Interestingly, the PC model mathematically takes the form of a generalized Lotka-Volterra model for two competing species with an external control parameter. We present a complete steady-state analysis in dependence of spatial anisotropy and external control. Additionally, we construct the relevant phase boundaries and characterize corresponding bifurcations in the parameter space spanned by the anisotropy and external control parameters. The PC model recovers all key features of the switching process observed in the full numerical simulations. With the specific example of polariton pattern switching at hand, we demonstrate how powerful simplified PC models can be to explore the phase space of complex nonlinear dynamical systems and to characterize possible stationary solutions. The preliminary work regarding the PC model was done in my master's thesis [82], where the model was derived and analyzed only numerically via a Gröbner basis formalism and geometrically via a nullcline analysis in contrast to the fully analytical treatment presented in this chapter. The switching setup is based on the publication Ref. [22], where numerical studies of the switching performance were performed. The main results of those two references are briefly revisited in the first section below in order to better understand the analysis of the nonlinear system which is the main result of this chapter and was published in Ref. [83].

## 3.1. Orthogonal switching of two-spot patterns

In this section we present the reversible on-demand switching of two-spot patterns as it was proposed in Ref. [22]. We perform a full numerical simulation demonstrating the switching process and discuss the underlying mechanism. The system is excited with an $x$-linearly polarized continuous-wave pump slightly above the minimum of the LPB
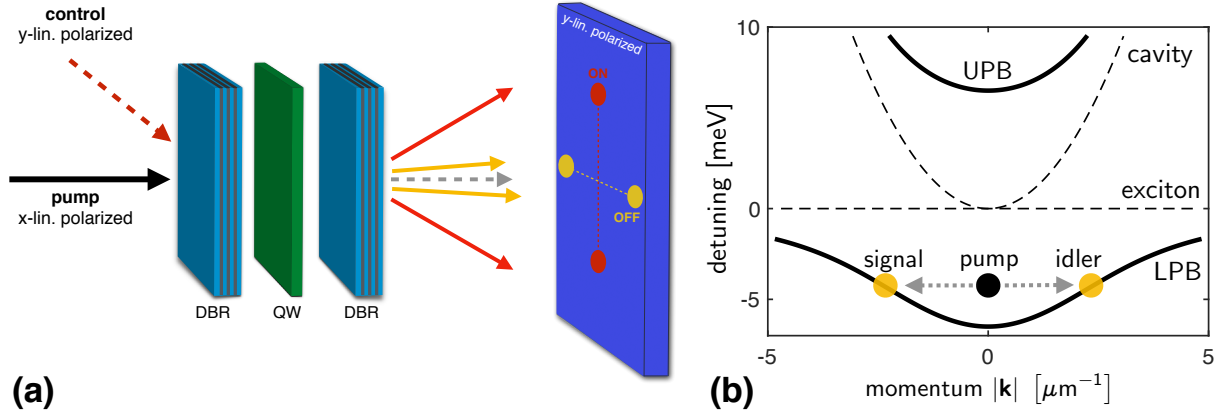
**Figure 3.1.** (a) Excitation geometry of a planar semiconductor microcavity. An $x$-linearly polarized pump in normal incidence slightly above the minimum of the LPB results in cross-linearly polarized signals at $\mathbf{k} \neq \mathbf{0}$ and $-\mathbf{k}$ oriented parallel to the pump's polarization plane. A resonant $y$-linearly polarized control beam can be utilize to switch between orthogonally oriented two-spot patterns. (b) In the dispersion relation, the pattern formation can be interpreted as a phase-matched four-wave mixing process on the LPB between the involved pump, signal, and idler fields. Parameters defined in Fig. 2.1. Adapted from Ref. [83].

at zero momentum (normal incidence onto the cavity plane); see Fig. 3.1. The pump has a super-Gaussian shape in real space and its intensity is set to be slightly above the modulation instability threshold. This threshold, where off-axis, i.e. $\mathbf{k} \neq \mathbf{0}$, modes start to grow against the decay due to efficient pairwise scattering of two pump polariton into opposite momentum modes $\mathbf{k}$ and $-\mathbf{k}$, can be determined by a linear stability analysis. The scattering into off-axis modes is most efficient for modes directly on the lower polariton branch of the dispersion relation at the pump's frequency; see Fig. 3.1(b). Alternatively, this process can be interpreted as phase-matched four-wave mixing of coherent polariton fields. Hence, the involved fields are also commonly termed pump, signal and idler.

Figure 3.2 schematically demonstrates the pattern formation process with the help of additional results from a linear stability analysis. A detailed description of the polarization-dependent linear stability analysis is given in Ref. [84] for example. Parameters used in Fig. 3.2 are explicitly given in the caption. Starting without any polarization dependence, Figures 3.2(a,b) reveal the maximum growth rates of the off-axis modes. They are located on the elastic ring in $k$-space defined by the intersection of the pump's energy plane with the LPB. Hence, the unstable off-axis modes preserve an azimuthal $O(2)$ symmetry in $k$-space. Taking the polariton's polarization dependence into account introduces anisotropic scattering and selections rules which determine the direction and polarization of the emission [10, 50, 84]. For linearly polarized excitation, the off-axis instability threshold is first reached for the four spatial directions parallel and perpendicular to the pump's polarization plane; see Fig. 3.2(c,d). Due to the polarization splitting of the cavity
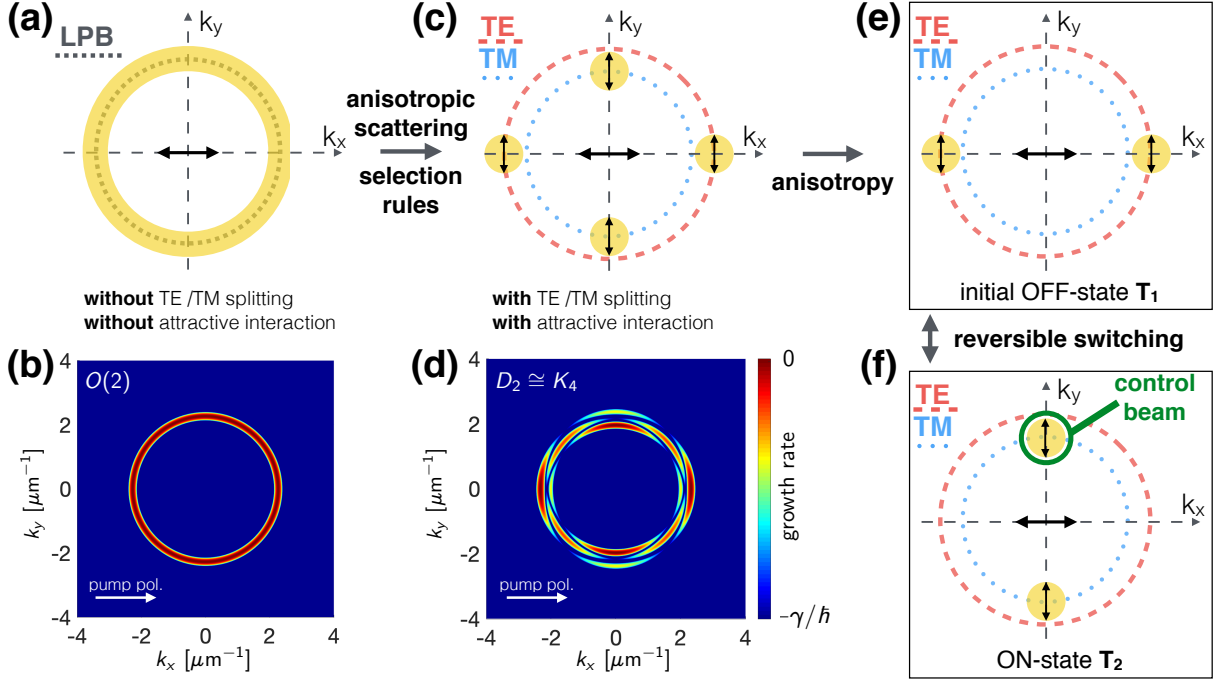
**Figure 3.2.** Sketch of the initial two-spot pattern formation and the orthogonal switching. The pump is $x$-linearly polarized and at normal incidence $k \approx 0$. (a) Elastic ring in $k$-space defined by the intersection of the pump's energy plane with the LPB. Without TE-TM splitting and without attractive cross interaction, the off-axis instability preserves an azimuthal $O(2)$ symmetry. Panel (b) shows the corresponding growth rates in $k$-space determined by a linear stability analysis. (c,d) With TE-TM splitting and attractive interaction, spatially anisotropic scattering and polarization selection rules lead to four $y$-polarized spots parallel and perpendicular to the pump's polarization plane, which preserve a $D_2$ symmetry. (e) Additional anisotropy can single out a two-spot pattern which serves as the initial OFF-state $T_1$ in the switching scheme. (f) A resonant $y$-polarized control beam can switch the pattern to the orthogonal ON-state $T_2$. Parameters are defined in the text below, except here we use $\gamma_c = \gamma_e = 0.2$ meV, (b) $T^{+-} = 0$, $m_{\mathrm{TE}} = m_{\mathrm{TM}}$, (c) $T^{+-} = -T^{++}/3$, $m_{\mathrm{TE}} = 1.4 \, m_{\mathrm{TM}}$. Adapted from Refs. [83,84]

dispersion, scattering of pump polaritons into finite momenta can occur in either TE or TM modes. Spin-dependent exciton-exciton interaction leads to additional selection rules. In the spectral range considered here, the interaction between excitons with opposite spins is attractive [46]. As a consequence, scattering of linearly polarized pump polaritons into cross-linearly polarized off-axis modes is favored. For the $x$-linearly polarized pump at hand, this results in TE polarized modes parallel and TM polarized modes perpendicular to the pump's polarization plane; see Figs. 3.2(c,d). The symmetry is reduced to the discrete symmetry of a non-equiangular rhombus described by the dihedral group $D_2$. In conclusion, linearly polarized excitation slightly above threshold leads to four cross-linearly polarized spots on the elastic circle oriented parallel and perpendicular to the pump's polarization plane; see Fig. 3.2(c,d). From here on, additional spatial anisotropy can favor one corresponding two-spot pattern. A slightly higher density of states for TE modes resembles a source of intrinsic anisotropy favoring the $x$-direction [10]. Additionally, slightly

tilting the pump away from normal incidence into the $x$-direction can artificially enhance the anisotropy. As a result, a stable two-spot pattern forms which serves as the initial OFF-state $T_1$ in the switching scheme; see Fig. 3.2(e). Now, a weak $y$-linearly polarized control beam incident on the elastic TM ring perpendicular to the pump's polarization plane can revive the orthogonal two-spot pattern $T_2$ due to stimulated scattering. Simultaneously, the occupation of the initial pattern $T_1$ decreases due to a cross-saturation effect and finally vanishes completely. The system now resides in the stable ON-state $T_2$ as long as the control beam is present; see Fig. 3.2(f). After the control beam is turned off again the system reverses to the initial OFF-state $T_1$ due to the spatial anisotropy.

As an example, Figure 3.3 shows the numerical results of the orthogonal switching obtained by simulating the equations of motions for the coherent light and exciton fields; see Eqs. (2.26) and (2.27) introduced in Sec. 2.1 above. The resonant $x$-linearly polarized pump with a super-Gaussian envelop in space is given by

$$E_{\text{pump}}^+ = E_{\text{pump}}^- = E_0 e^{-(\mathbf{r}^2/w_p^2)^{10}} e^{ik_p x} e^{-i\omega_p t} \tag{3.1}$$

where $w_p = 25$ $\mu$m and $\omega_p = -\Omega + 2.5$ meV are radius and frequency of the resonant continuous-wave pump. The chosen amplitude $E_0$ yields an excitation intensity of about $I_{\text{pump}} = |E_0|^2 \omega_{\text{full}}/\gamma_c \approx 51.68$ kWcm$^{-2}$ where $\omega_{\text{full}} = 1.5$ eV is the full frequency of the exciton resonance. The parameter $k_p = 0.2$ $\mu$m$^{-1}$ describes the small tilt in $x$-direction away from normal incidence to enhance the anisotropy. The other system parameters, typical for GaAs structures [44], are given by $m_{\text{TE}} = 1.05$ $m_{\text{TM}} = 0.215$ meVps$^2\mu$m$^{-2}$, $\Omega = 6.5$ meV, $\gamma_c = 0.8$ meV, $\gamma_e = 0.2$ meV, $\alpha_{\text{psf}} = 5.188 \times 10^{-4}\mu$m$^2$, and $T^{++} = -5T^{+-} = 5.69 \times 10^{-3}$meV$\mu$m$^2$. The set of physical parameters which defines this specific example is directly related to the corresponding case of the simplified PC model in the next section. Numerical simulations are performed via a fourth-order Runge-Kutta method with a fixed step size of $\Delta t = 0.02$ ps on a spatial grid of Length $L = 60$ $\mu$m sampled by $N^2 = 201^2$ points.

Figure 3.3 shows the normalized $k$-space emission of the cavity field in the $y$-polarization channel $|E_{\mathbf{k}}^y|^2$ for the stationary (a) OFF-state $T_1$ and (b) ON-state $T_2$. Without control beam the system remains in stable state $T_1$. The control beam has the same shape as the pump defined in Eq. (3.1) but it is $y$-linearly polarized and resonant with the TM ring on the $k_y$-axis. Its threshold amplitude in order to trigger the switching is about three orders of magnitude smaller than the pump's amplitude. While the control beam is present, the system switches to and remains in stationary ON-state $T_2$. After the control beam is switched off again, the system automatically reverses to the initial OFF-state $T_1$. Detailed performance studies in Ref. [22] revealed possible switching times in the range of 100 ps, backswitching times of 400 ps and maximum gain factors of about 25.
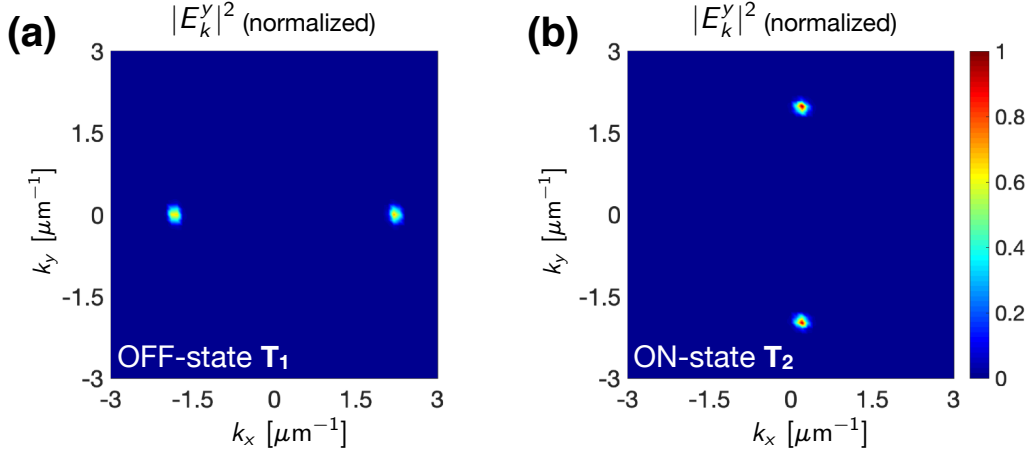
**Figure 3.3.** Numerical results for the orthogonal two-spot polariton pattern switching for the $k$-space density in the $y$-polarization channel of stationary (a) OFF-state $T_1$ which forms without control beam and (b) ON-state $T_2$ which emerges when the weak control beam is present. The emission is normalized to the maximum density of the ON-state. Parameters are given in the text. Adapted from Refs. [22, 83].

From here on, we move in a different direction to gain more insight in the underlying nonlinear system which enables the orthogonal polariton pattern switching described above. To this end, a simplified PC model for the dynamics of the relevant modes in $k$-space is directly derived from the full equations of motion for the cavity and exciton field and it is systematically studied in the next section. We investigate the existence and stability of all possible steady states in dependence of the model parameters which are related to the underlying physical processes. Furthermore, emerging bifurcations in dependence of the anisotropy and external control parameter are characterized.

## 3.2. Population competition model

In this section we systematically analyze a simplified PC model based on the orthogonal switching of two-spot patterns presented in the previous section above. A similar PC model was studied in context of polariton pattern formation in order to investigate the scalar case without polarization dependence where hexagonal patterns arise [85]. The derivation starts with the full equations of motion for the cavity field and the exciton polarization and only uses a few reasonable assumptions; see Appendix B for details. The final PC model reads

$$\partial_t A_1 = \alpha_1 A_1 - \beta_1 A_1^3 - \theta_1 A_2^2 A_1,$$
$$\partial_t A_2 = \alpha_2 A_2 - \beta_2 A_2^3 - \theta_2 A_1^2 A_2 + S, \tag{3.2}$$

where $A_1$ and $A_2$ represent the real-valued dimensionless amplitudes of the two orthogonal mode pairs in $k$-space, which constitute the elementary states of the system as introduced
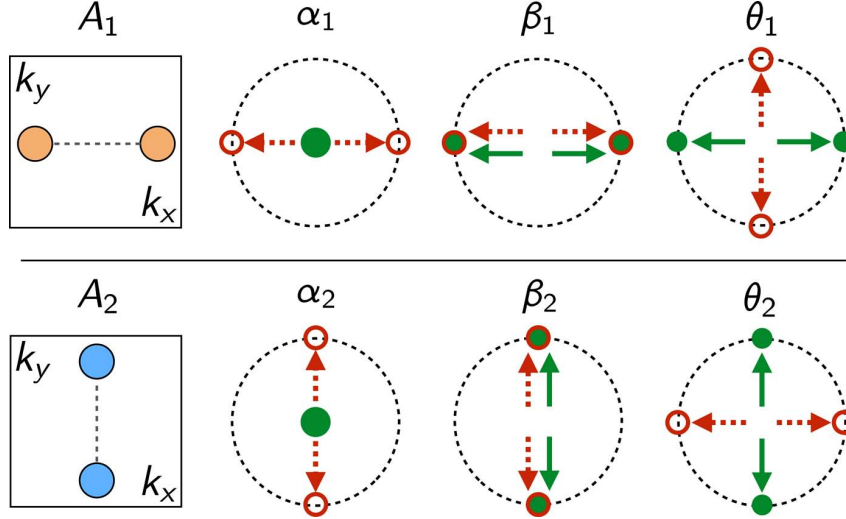
**Figure 3.4.** Sketch of the relevant polariton-polariton scattering processes on the elastic ring for the two mode pairs $A_1$ and $A_2$ in reduced $k$-space, which are described by the simplified PC model defined in Eq. (3.2). Solid green (open red) circles indicate incoming (outgoing) modes of the specific scattering processes. Additionally, solid (dashed) arrows show their corresponding incoming (outgoing) momenta. The linear process $\alpha_i$ describes growth of each mode pair due to stimulated scattering from the pump induced zero-momentum mode. The cubic processes $\beta_i$ and $\theta_i$ describe self- and cross-saturation. Reprinted from Ref. [83].

in the previous section. For the steady-state analysis ahead, it is possible to remove the time-dependent phases since they become locked for stationary states; see Appendix B for more details. All six positive and dimensionless model parameters $\alpha_i$, $\beta_i$, and $\theta_i$ directly correspond to the relevant polariton-polariton scattering processes up to third order; see Fig. 3.4. Hence, the investigation is restricted to destabilizing linear terms and stabilizing nonlinearities which resembles the conditions observed in the numerical simulations. In the presence of polarization dependence and spatial anisotropy, these parameters are intrinsically different for the two mode pairs $A_1$ and $A_2$. Importantly, all model parameters can be directly calculated from the physical quantities of the specific system as we demonstrate further below. Figure 3.4 summarizes all processes which are captured within the individual terms of the PC model defined in Eq. (3.2). The linear term proportional to $\alpha_i$ represents the growth of each mode pair and leads to exponential increase until the saturation processes become relevant. The latter are described by the cubic terms and are separated into a self-saturation process represented by $\beta_i$ and a cross-saturation process represented by $\theta_i$. Without cross-saturation $\theta_i = 0$, the dynamical equations of the PC model are decoupled and can be solved separately. Then, for both mode pairs $A_1$ and $A_2$ the exponential growth is stabilized by the self-saturation which results in a stationary four-spot pattern with independent amplitudes for $A_1$ and $A_2$. With cross-saturation $\theta_i > 0$ however, the two mode pairs are coupled and tend to suppress each other, which can lead to the complete extinction of one mode pair, possibly resulting in a

stationary two-spot pattern. Additionally, the external control parameter $S$ is a manually added source term for the particular mode pair $A_2$ leading to linear growth and triggering the switching process. In conclusion, the simplified PC model qualitatively captures the dynamics of three competing patterns: The two-spot patterns $T_1$ and $T_2$ as well as the four-spot pattern $F$. In the following we present a systematical steady-state analysis of the simplified PC model and relate the results to the numerical studies based on the full model.

First, we lay down the general procedure and the basic notation to study nonlinear dynamical systems. We rewrite the PC model given in Eq. (3.2) as

$$\begin{pmatrix} \partial_t A_1 \\ \partial_t A_2 \end{pmatrix} = \begin{pmatrix} \alpha_1 A_1 - \beta_1 A_1^3 - \theta_1 A_2^2 A_1 \\ \alpha_2 A_2 - \beta_2 A_2^3 - \theta_2 A_1^2 A_2 + S \end{pmatrix} \equiv \begin{pmatrix} f_1 \\ f_2 \end{pmatrix} = \mathbf{f}, \tag{3.3}$$

so that steady states are given by the polynomial roots $\mathbf{f}(A_1, A_2) = \mathbf{0}$. They are also referred to as fixed point, nodes, and equilibrium points in a synonymous way hereinafter. In principle, four qualitatively different types of stationary solutions occur: (i) Two-spot pattern $T_1$ ($A_1 \neq 0$, $A_2 = 0$), (ii) two-spot pattern $T_2$ ($A_1 = 0$, $A_2 \neq 0$), (iii) four-spot pattern $F$ ($A_1 \neq 0$, $A_2 \neq 0$), and (iv) trivial solution ($A_1 = 0$, $A_2 = 0$). In the following we are only interested in physical solutions $A_i \geq 0$ and hence restrict the state space to the first quadrant of the ($A_1, A_2$) plane which is equivalent to the set $\mathbb{R}^2_{\geq 0}$. As a result of the Hartman-Grobman theorem [86, p. 350], the dynamical behavior near hyperbolic fixed points is completely determined by linearization around those points. Thus, stability properties are given by the real parts of the eigenvalues of the system's Jacobian matrix which explicitly reads

$$J \equiv \left( \frac{\partial f_i}{\partial A_j} \right) = \begin{pmatrix} \alpha_1 - 3\beta_1 A_1^2 - \theta_1 A_2^2 & -2\theta_1 A_1 A_2 \\ -2\theta_2 A_1 A_2 & \alpha_2 - 3\beta_2 A_2^2 - \theta_2 A_1^2 \end{pmatrix}. \tag{3.4}$$

Regarding fixed points, hyperbolic means nonzero real parts of all eigenvalues of the corresponding Jacobian. The eigenvalues are given by

$$\lambda_\pm = \frac{\text{tr } J \pm \sqrt{\text{tr}^2 J - 4 \det J}}{2}. \tag{3.5}$$

The Jacobian matrix allows a simple characterization of all possible hyperbolic fixed points of a dynamical system; see Fig. 3.5.

We define a phase of the PC model as a set which contains the number of steady-state solutions and their corresponding stability properties. These phases depend on all seven model parameters. In this high-dimensional parameter space, a phase boundary characterizes a phase transition, i.e. a change in the number of stationary states, a change
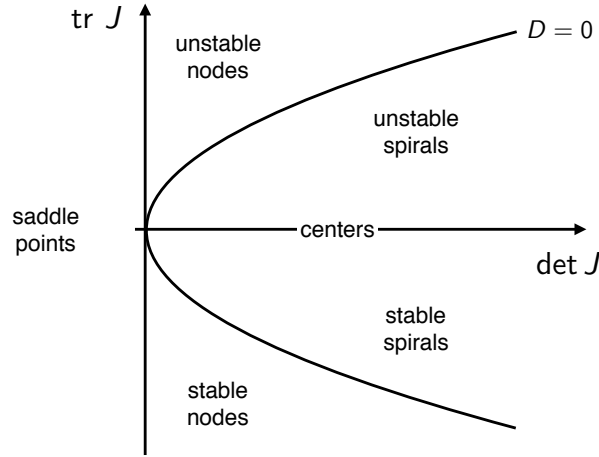
**Figure 3.5.** Classification of hyperbolic fixed points by the properties of the corresponding Jacobian matrix, i.e. by linearization. $D = \text{tr}^2 J - 4 \det J$ is the discriminant. Reproduced from Ref. [87].

in their stability properties, or both the aforementioned. This transition is only possible if at least one of the Jacobian's eigenvalues becomes zero at the boundary. Equivalently, the formal condition for a phase boundary in parameter space reads [85, 86]

$$\{\mathbf{f}, \det J\} = \mathbf{0}, \tag{3.6}$$

where the determinant is explicitly given by

$$\begin{aligned} \det(J) = & 3\beta_1\theta_2 A_1^4 + 3\beta_2\theta_1 A_2^4 - (3\beta_1\alpha_2 + \alpha_1\theta_2)A_1^2 - (3\beta_2\alpha_1 + \alpha_2\theta_1)A_2^2 \\ & - (3\theta_1\theta_2 - 9\beta_1\beta_2)A_1^2 A_2^2 + \alpha_1\alpha_2. \end{aligned} \tag{3.7}$$

Constructing phase boundaries is effectively equivalent to finding roots of the set of the three polynomial equations given in Eq. (3.6). Fortunately, in our case all solutions can be found analytically with the help of computer algebra systems for example. Having all the required tools at hand, we now start with the steady-state analysis which is separated into the homogeneous case with $S = 0$ and the inhomogeneous case with $S > 0$ and we conclude with some further remarks.

## 3.2.1. Homogeneous case

We start with the homogeneous case of the PC model and set $S = 0$ in Eq. (3.2). Interestingly, it takes the mathematical form of a generalized Lotka-Volterra (GLV) model [88] with cubic nonlinearities. Moreover, a monomial transformation $A_i \to A_i^2 \equiv \tilde{A}_i$ yields the Lotka-Volterra model for two competing species in its usual form with quadratic

nonlinearities [89]

$$\partial_t \tilde{A}_i = \tilde{A}_i \left( r_i - \sum_{j=1}^{2} c_{ij} \tilde{A}_j \right),$$ (3.8)

for $i = 1, 2$ and where $\mathbf{r} = 2(\alpha_1, \alpha_2)$ is the growth rate vector, and $C \equiv (c_{ij})$ is the community matrix, which contains the self- and cross-saturation parameters, explicitly

$$C = 2 \begin{pmatrix} \beta_1 & \theta_1 \\ \theta_2 & \beta_2 \end{pmatrix}.$$ (3.9)

Note that the monomial transformation does not qualitatively change the phase portraits, i.e. the trajectories in the $(A_1, A_2)$ state space, of the original system [88, 90]. The phase portraits of the original and the transformed system are topologically equivalent, and hence all steady states and their stability properties are conserved. Consequently, the qualitative dynamical behavior of the homogeneous case of the PC model can be completely reduced to that of the usual Lotka-Volterra (LV) model, which are very common in population dynamics, e.g. they describe predator-prey relationships or the dynamics of interspecific competition as in our case. The LV model for competing species defined in Eq. (3.8) has been investigated in various fields of science, such as physics [91], chemistry [92], ecology [93], and economics [94]. Importantly, its dynamics are limited to three different cases [95]: (i) Coexistence regime for $\mathrm{sgn}(\det C) = \mathrm{sgn}(\beta_1\beta_2 - \theta_1\theta_2) = +1$ (larger self-saturation), (ii) bistability regime for $\mathrm{sgn}(\det C) = -1$ (larger cross-saturation), and (iii) dominance regime for a sufficiently large growth rate difference $|\alpha_1 - \alpha_2|$, where the dynamics are independent of the saturation parameters. Here we can directly draw some analogies to the ecological context and apply general ideas from population dynamics. Coexistence theory [96, 97] explains the possible coexistence of two competing species by interaction of two opposing mechanisms: (i) The fitness difference (growth rate difference $|\alpha_1 - \alpha_2|$) leads to the extinction of one population (via coupling $\theta_i$) and (ii) stabilizing mechanisms (self-saturation $\beta_i$) can prevent the extinction. Hence, in order to favor the coexistence regime, the fitness difference has to be reduced (smaller $|\alpha_1 - \alpha_2|$) and the stabilizing mechanism has to be increased (larger self-saturation ($\beta_1\beta_2 > \theta_1\theta_2$). In the other regimes only one of the two populations can survive. As a result of the topological equivalence, we find the same three limiting cases described above in the homogeneous case of the PC model. Nevertheless, we present a short discussion of the homogeneous case and relate it to the polariton pattern switching process. Additionally, we discuss the differences compared to the usual LV model in terms of the emerging bifurcations.

Solving the system of polynomial equations given in Eq. (3.6) yields the following steady states and phase boundaries for the homogeneous case:

(i) Two-spot pattern $T_1$ with

$$A_1 = \sqrt{\frac{\alpha_1}{\beta_1}}, \ A_2 = 0, \ \text{stable for} \ \frac{\alpha_1}{\alpha_2} > \frac{\beta_1}{\theta_2}, \tag{3.10}$$

(ii) two-spot pattern $T_2$ with

$$A_1 = 0, \ A_2 = \sqrt{\frac{\alpha_2}{\beta_2}}, \ \text{stable for} \ \frac{\alpha_1}{\alpha_2} > \frac{\theta_1}{\beta_2}, \tag{3.11}$$

(iii) four-spot pattern $F$ which only exists in the range $\frac{\beta_1}{\theta_2} \lessgtr \frac{\alpha_1}{\alpha_2} \lessgtr \frac{\theta_1}{\beta_2}$ with

$$A_1 = \sqrt{\frac{\alpha_2\theta_1 - \alpha_1\beta_2}{\theta_1\theta_2 - \beta_1\beta_2}}, \ A_2 = \sqrt{\frac{\alpha_1\theta_2 - \alpha_2\beta_1}{\theta_1\theta_2 - \beta_1\beta_2}}, \ \text{stable for} \ \theta_1\theta_2 < \beta_1\beta_2, \tag{3.12}$$

(iv) trivial solution with

$$A_1 = 0, \ A_2 = 0, \ \text{always unstable.} \tag{3.13}$$

Both two-spot patterns and the trivial solution exist in the whole $S = 0$ parameter subspace, whereas the existence of the four-spot pattern is limited to a specific parameter region and emerges as part of pitchfork bifurcations, as we discuss further below. The trivial solution is always unstable and is not listed anymore in the following. For a better visualization and a systematic investigation, we define an anisotropy parameter $\delta\alpha$ via $\alpha_1 \rightarrow \alpha_1 + \delta\alpha$ and set $\alpha_1 = \alpha_2 = 1$ hereinafter. This parameter favors mode pair $A_1$ for $\delta\alpha > 0$ and $A_2$ for $\delta\alpha < 0$, respectively. The phase boundaries in the $S = 0$ subspace are then located at positions $\delta\alpha_1^* = \theta_1/\beta_2 - 1$ and $\delta\alpha_2^* = \beta_1/\theta_2 - 1$. Figure 3.6 shows an overview of all stationary states of the PC model, their stability properties, as well as the phase boundaries in two-dimensional parameter space spanned by the anisotropy parameter and the external control parameter. Panel (a) displays the case for larger self-saturation $\beta_1\beta_2 > \theta_1\theta_2$ and panel (b) shows the other case of larger cross-saturation $\beta_1\beta_2 < \theta_1\theta_2$. Green (red) bold letters indicate unstable (unstable) steady state in each region. Here, we are only interested in the one-dimensional $S = 0$ subspace which is enlarged at the bottom of each panel. The phase boundaries on the $\delta\alpha$-axis show the typical LV three-case structure as describe above. For sufficiently large anisotropy values $|\delta\alpha|$, we find the dominance regime of either stable two-spot pattern $T_1$ or $T_2$ that are labeled by numbers 1 and 2 in Fig. 3.6. The topology of the phase portraits, and hence the general dynamical behavior in this regime, is independent of the saturation parameters. However, for small anisotropy values $|\delta\alpha| \approx 0$ two different cases arise. For larger self-saturation we find the coexistence regime with a stable four-spot pattern $F_1$; see label number 3a in Fig. 3.6(a).

For larger cross-saturation we find the bistability regime with both stable two-spot patterns $T_1$ and $T_2$; see label number 3b in Fig. 3.6(b). Interestingly, the latter case raises the question in which of the two stable steady states the system will finally end up in. To tackle this question more information is required.

A valuable tool to further investigate the dynamics of the two-dimensional nonlinear systems is drawing the flow in the state space for the relevant cases. The PC model defines a vector field in the state space which assigns to every point $(A_1, A_2)$ a velocity vector $\mathbf{v} \equiv \mathbf{f}(A_1, A_2)$. This velocity vector field determines the system's trajectories in phase space. A good visualization of the flow is to draw some representative trajectories $(A_1(t), A_2(t))$, which can always be obtained by numerical integration methods. Figure 3.7 shows the flow in state space represented by a few characteristic trajectories for all cases shown in Fig. 3.6. Each flow panel is assigned by a label number to a specific phase. Stable (unstable) fixed points are marked by black (white) circles. Additionally, regions are color-coded to the corresponding stable stationary state the system will end up in. Cases 1 and 2 refer to the dominance regimes. In both cases two fixed points exist with opposite stability properties which correspond to the two-spot patterns $T_1$ and $T_2$. In case 3a (coexistence regime) two unstable fixed points and one stable fixed point exist. The latter refers to the stable four-spot pattern $F_1$. In these three cases above, the system's long-time dynamics are unambiguous since only one attractor exists in the whole state space. All trajectories will end up at the attractor for sufficiently long times. In contrast, in the bistability regime (case 3b) two attractors exist simultaneously, and hence the system's long-time behavior depends on its history, i.e. hysteresis occurs. In Figure 3.7 case 3b, the two basins of attraction of both two-spot patterns $T_1$ and $T_2$ are differently color-coded. Any initial condition will stay in its initial region and finally end up at the corresponding attractor. The two basins of attraction are separated by a trajectory which goes through the unstable saddle point $F_1$ and is often referred to as the separatrix. Technically, it is the stable manifold of saddle point $F_1$ and is defined as the set of all points $(A_1, A_2)$ which satisfy $(A_1, A_2) \rightarrow F_1$ for $t \rightarrow \infty$. In addition, the unstable manifold of saddle point $F_1$ consists of all points which satisfy $(A_1, A_2) \rightarrow F_1$ for $t \rightarrow -\infty$, and hence it connects the two stable nodes with the unstable saddle point.

As mentioned above, the key statement of the Hartman-Grobman theorem [86, p. 350] is that a dynamical system near hyperbolic fixed points qualitatively behaves the same as its linearization. This allows us to characterize the system's steady states by a linear stability analysis, i.e. the eigenvalues of the Jacobian matrix. However, if the real part of at least one Jacobian eigenvalue becomes zero the system does not necessarily behaves similar to its linear counterpart and the nonlinear terms become relevant, i.e. the topology of the phase portrait changes and the system bifurcates. In parameter space, we refer

to bifurcation points as phase boundaries which indicate a change in number of steady states and/or their stability properties. The emerging bifurcations can be characterize via normal forms and center manifold theory [86,87]. In the common LV model with quadratic nonlinearities transcritical bifurcations occur [98]. However, in the PC model pitchfork bifurcations arise when the anisotropy parameter is varied due to the additional $\mathbb{Z}_2 \times \mathbb{Z}_2$ symmetry from the cubic nonlinearities, explicitly $A_i \to -A_i$. Pitchfork bifurcations are common in systems with inversion symmetry [87]. They are an example of codimension-one bifurcations which means they can be triggered by varying only one parameter; here, the anisotropy parameter $\delta\alpha$. At a pitchfork bifurcation the system changes from one to three steady states while reversing its stability properties. Due to the simple steady-state structure of the PC model, the types of bifurcations can be directly read off from the changes in the phase portraits, i.e. the flow structure in the state space, while crossing phase boundaries. Nevertheless, we also present a more formal determination with the help of center manifold theory for the equilibrium point $T_2$ as an example. A detailed presentation of the general procedure can be found in Refs. [86, 99, 100]. For the fixed point $T_2$ with $A_1 = 0$ and $A_2 = \sqrt{\alpha_2/\beta_2}$, the corresponding Jacobian matrix reads

$$J|_{T_2} = \begin{pmatrix} \alpha_1 - \theta_1 \frac{\alpha_2}{\beta_2} & 0 \\ 0 & -2\alpha_2 \end{pmatrix}, \tag{3.14}$$

which is already in diagonal form. Eigenvalue $-2\alpha_2 \in \mathbb{R}_{<0}$ corresponds to the stable eigenspace of the fixed point spanned by $(0, 1)^{\mathrm{T}}$ ($A_2$-axis). However, the other eigenvalue becomes zero at the phase boundary, i.e. $\alpha_1 - \theta_1\alpha_2/\beta_2 = 0$, and corresponds to the center eigenspace of the fixed point spanned by $(1, 0)^{\mathrm{T}}$. According to the center manifold theorem [86, p. 38], there is a neighborhood of the fixed point where a stable manifold exists which is tangential to the stable eigenspace at the fixed point. The dynamical behavior on the stable manifold is simple attraction to the equilibrium point. Analogously, there is a center manifold tangential to the center eigenspace at the fixed point. This one-dimensional subspace is the important part where the bifurcation actually happens and the dynamics are qualitatively influenced by the nonlinear terms. Now we have to find an approximation for the center manifold $\tilde{A}_2 = h(\tilde{A}_1, \mu)$. First, we shift the equilibrium point to the origin, i.e. $A_2 \to A_2 - \sqrt{\alpha_2/\beta_2} \equiv \tilde{A}_2$ and $\tilde{A}_1 \equiv A_1$, and introduce the bifurcation parameter $\mu \equiv \alpha_1 - \theta_1\alpha_2/\beta_2$ which is a shifted version of the anisotropy parameter. With these definitions the equivalent PC model extended by the dimension of the bifurcation

parameter reads

$$\partial_t \tilde{A}_1 = \mu \tilde{A}_1 - \beta_1 \tilde{A}_1^3 - \theta_1 \left( \tilde{A}_2^2 + 2\tilde{A}_2 \sqrt{\frac{\alpha_2}{\beta_2}} \right) \tilde{A}_1, \tag{3.15}$$

$$\partial_t \tilde{A}_2 = -2\alpha_2 \tilde{A}_2 - 3\beta_2 \sqrt{\frac{\alpha_2}{\beta_2}} \tilde{A}_2^2 - \beta_2 \tilde{A}_2^3 - \theta_2 \tilde{A}_1^2 \left( \tilde{A}_2 + \sqrt{\frac{\alpha_2}{\beta_2}} \right), \tag{3.16}$$

$$\partial_t \mu = 0, \tag{3.17}$$

which has an equilibrium point at $(\tilde{A}_1, \tilde{A}_2) = (0,0)$ and bifurcates at $\mu = 0$. We already know that the center manifold goes through the origin tangentially to the $\tilde{A}_1$-axis. Hence, we make the following expansion ansatz

$$h(\tilde{A}_1, \mu) = a\tilde{A}_1^2 + b\mu \tilde{A}_1 + c\mu^2 + \dots . \tag{3.18}$$

In order to determine the coefficients $a, b,$ and $c$, we use two expressions for the equation of motion for $\tilde{A}_2$ near the equilibrium point on the center manifold. On the one hand, the PC model itself contains an equation of motion for $\tilde{A}_2$. We substitute the expansion of the center manifold $h(\tilde{A}_1, \mu)$ in Eq. (3.16) and obtain

$$\partial_t \tilde{A}_2 = -2\alpha_2 h(\tilde{A}_1, \mu) - 3\beta_2 \sqrt{\frac{\alpha_2}{\beta_2}} h^2(\tilde{A}_1, \mu) - \beta_2 h^3(\tilde{A}_1, \mu) - \theta_2 \tilde{A}_1^2 \left( h(\tilde{A}_1, \mu) + \sqrt{\frac{\alpha_2}{\beta_2}} \right). \tag{3.19}$$

Keeping only terms up to second order in $\tilde{A}_1$ and $\mu$ leads to

$$\partial_t \tilde{A}_2 = -2\alpha_2 \left( a\tilde{A}_1^2 + b\mu \tilde{A}_1 + c\mu^2 \right) - \theta_2 \tilde{A}_1^2 \sqrt{\frac{\alpha_2}{\beta_2}}. \tag{3.20}$$

On the other hand, from the expansion of the center manifold we obtain

$$\begin{aligned}
\partial_t \tilde{A}_2 &= \partial_t h(\tilde{A}_1, \mu) \\
&= \partial_{\tilde{A}_1} h(\tilde{A}_1, \mu) \partial_t \tilde{A}_1 + \partial_\mu h(\tilde{A}_1, \mu) \partial_t \mu \\
&= \partial_{\tilde{A}_1} h(\tilde{A}_1, \mu) \partial_t \tilde{A}_1 \\
&= \left( 2a\tilde{A}_1 + b\mu \right) \left[ \mu \tilde{A}_1 - \beta_1 \tilde{A}_1^3 - \theta_1 \left( h^2(\tilde{A}_1, \mu) + 2h(\tilde{A}_1, \mu) \sqrt{\frac{\alpha_2}{\beta_2}} \right) \tilde{A}_1 \right].
\end{aligned} \tag{3.21}$$

Since this equation has no terms of second order or lower in $\tilde{A}_1$ and $\mu$, by comparison the coefficients are given by

$$-2a\alpha_2 - \theta_2 \sqrt{\frac{\alpha_2}{\beta_2}} = 0, \quad -2b\alpha_2 = 0, \quad -2c\alpha_2 = 0, \tag{3.22}$$

and the center manifold finally reads

$$h(\tilde{A}_1) = -\frac{\theta_2}{2\alpha_2}\sqrt{\frac{\alpha_2}{\beta_2}}\tilde{A}_1^2. \tag{3.23}$$

Substituting this expression back into the equation of motion for $\tilde{A}_1$, i.e. Eq. (3.15), gives the dynamical behavior on the center manifold

$$\begin{aligned}\partial_t\tilde{A}_1 &= \mu\tilde{A}_1 - \beta_1\tilde{A}_1^3 - \theta_1\left(h^2(\tilde{A}_1) + 2h(\tilde{A}_1)\sqrt{\frac{\alpha_2}{\beta_2}}\right)\tilde{A}_1 \\ &= \mu\tilde{A}_1 + (\theta_1\theta_2 - \beta_1\beta_2)\,\tilde{A}_1^3 + \mathcal{O}(\tilde{A}_1^5),\end{aligned} \tag{3.24}$$

which resembles the normal form of a pitchfork bifurcation [87, p. 246]. Depending on the sign of the nonlinear coefficient, i.e. $\mathrm{sgn}\,(\theta_1\theta_2 - \beta_1\beta_2) = -\mathrm{sgn}(\det C)$, the pitchfork bifurcation is either supercritical for a negative sign or subcritical for a positive sign. The other pitchfork bifurcation associated with equilibrium point $T_1$ can be determined in a similar way. In the case of larger self-saturation supercritical pitchfork bifurcations occur. They are characterized by a stable fixed point becoming an unstable saddle and the appearance of two additional stable fixed points. This behavior is observed while transitioning from region 1 to 3a by increasing $\delta\alpha$; see corresponding cases in Fig. 3.6(a) and Fig. 3.7. Stable $T_2$ becomes unstable and additionally stable $F_1$ arises, entering the coexistence regime. Note that the third steady state is not shown since it lies in the fourth quadrant of $(A_1, A_2)$ state space, and hence does not correspond to a physical solution. The same behavior happens while transitioning from region 2 to 3a by decreasing $\delta\alpha$; see corresponding cases in Fig. 3.6(a) and Fig. 3.7. Stable $T_1$ becomes an unstable saddle and additionally stable $F_1$ arises. In the case of larger cross-saturation the pitchfork bifurcations are subcritical. We observe the same transitions at $\delta\alpha^*_{1,2}$, but this time with reversed stability properties; see corresponding cases in Fig. 3.6(b) and Fig. 3.7. From region 1 to 3b and from 2 to 3b, unstable saddle nodes $T_1$ and $T_2$ become stable nodes and additionally an unstable saddle $F_1$ arises, entering the bistability regime.

Coming back to the original physical system and the polariton pattern switching, we learned different important results. In the homogeneous case of the PC model ($S = 0$), the long-time dynamical behavior is equivalent to the famous LV model for two competing species. We find the same three parameter regimes of dominance, coexistence and bistability. However, due to the additional inversion symmetry in the PC model, we observe pitchfork (instead of transcritical) bifurcations at the phase boundaries. Regarding the switching process, the homogeneous case refers to the initial pattern formation before the control beam is applied and the backswitching process after the control beam is turned off again. Both processes can only work reliably in the dominance regime where two-spot pattern $T_1$ is

the only attractor. As a result, a minimum value of the anisotropy parameter $\delta\alpha$ is required, which can be achieved by slightly tilting the incidence of the pump in the desired target direction. In the case of larger self-saturation, the strong intraspecific competition leads to coexistence in a particular anisotropy range, and hence to a stable four-spot pattern $F_1$. This region should be avoided since it might prevent backswitching. In the case of larger cross-saturation, the strong interspecific competition leads to bistability in a particular anisotropy range, and hence to two stable two-spot patterns $T_1$ and $T_2$. This region should also be avoided since hysteresis behavior prevents backswitching. To verify that these results of the PC model agree with the full numerical simulation presented in Sec. 3.1, we calculate the model parameters directly from the physical quantities via Eq. (B.13) and check in which LV regime we end up in. We choose the locked phases according to the physical behavior observed in the full numerical simulations, i.e. this choice should result in destabilizing linear and stabilizing nonlinear parameters. Characteristic value choices of $\tilde{p}_{j,c}^{y} = 1$ $\mu$m, $t_c = 1$ ps, $\delta_1 = 0.2$ meV, and $\delta_2 = 0$ meV result in the following PC model parameters: $\alpha_1{=}0.49$, $\alpha_2{=}0.43$, $\beta_1{=}0.007$, $\beta_2{=}0.01$, $\theta_1{=}0.006$, and $\theta_2{=}0.005$. These parameters belong to the case of larger self-saturation and the dominance regime of $T_1$ for $S = 0$ which are preferred for the reversible on-demand switching application. The homogeneous case of the simplified PC model captures the important mechanism responsible for initial pattern buildup and the final pattern reversal. The actual switching process triggered by the control beam is the focus of the next section.
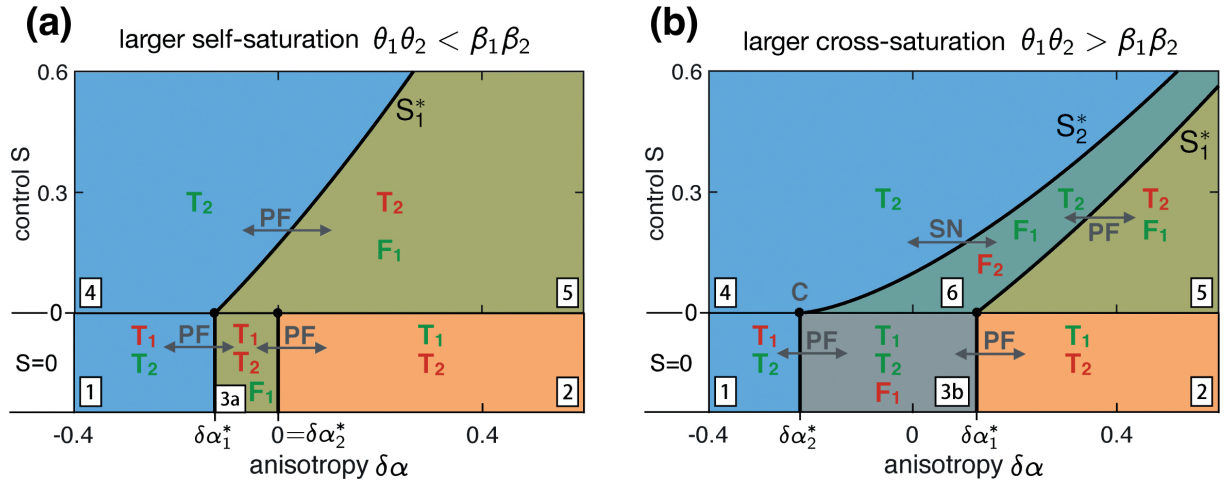


**Figure 3.6.** Overview of all possible stationary states and their stability properties of the PC model in dependence of the anisotropy and external control for two different cases: (a) Larger self-saturation with parameters $\beta_1 = 0.7$, $\beta_2 = 0.8$, and $\theta_1 = \theta_2 = 0.7$ which yield a ratio of $\beta_1\beta_2/\theta_1\theta_2 \approx 1.14$. (b) Larger cross-saturation with parameters $\beta_1 = 0.7$, $\beta_2 = 0.8$, and $\theta_1 = \theta_2 = 0.9$ which yield a ratio of $\beta_1\beta_2/\theta_1\theta_2 \approx 0.69$. Green (red) bold letters mark stable (unstable) steady states. $S_1^*$ and $S_2^*$ are the phase boundaries defined in Eqs. (3.25) and (3.25). Arrows with letters across the phase boundaries characterize the corresponding bifurcations with PF = pitchfork, SN = saddle node, C = Cusp. Reprinted from Ref. [83].
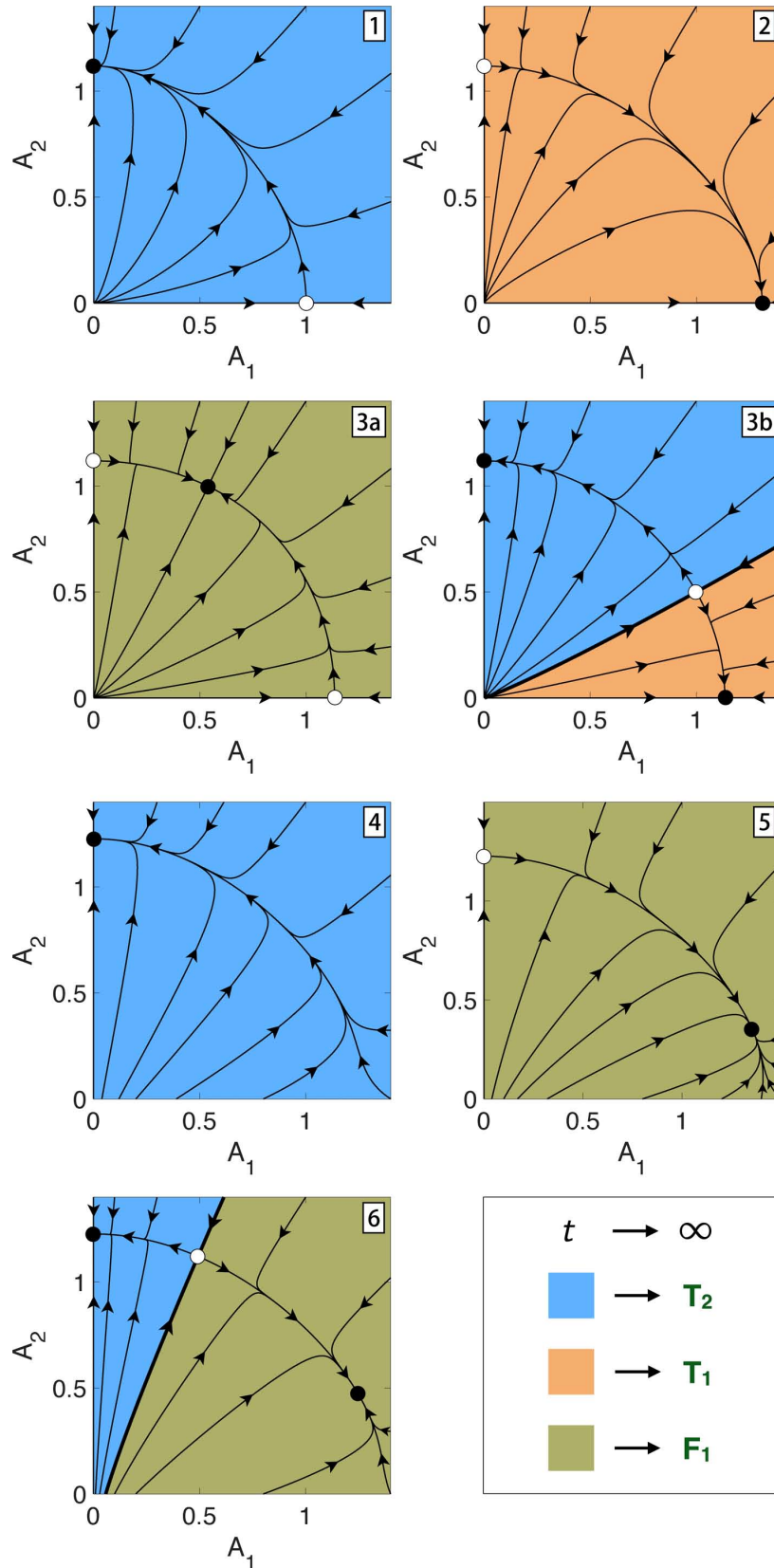
**Figure 3.7.** Phase portraits of all cases defined in Fig. 3.6 connected by label numbers top right. Each panel shows exemplary trajectories in the $(A_1, A_2)$ state space. Black (white) circles mark stable (unstable) fixed points. Color-coded regions are the basins of attraction of the corresponding attractors defined in the legend bottom right. Reprinted from Ref. [83]

## 3.2.2. Inhomogeneous case

In this section we investigate the inhomogeneous case of the PC model defined in Eq. (3.2) by including finite values for the control parameter $S > 0$. This case describes the switching process of the orthogonal two-spot patterns triggered by the external control pulse. In the past, inhomogeneous PC models have not received much attention, although a constant term in GLV models can be motivated in various fields besides the polariton pattern switching scheme, e.g. as a constant influx of a component in chemical reactions, or as constant harvesting or constant migration in ecological systems. Note that in Ref. [101] an inhomogeneous version of the usual LV model with quadratic nonlinearities was investigated from a mathematical perspective. Here, we study a GLV model with third-order nonlinearities extended with a constant term applied to the orthogonal switching of two-spot polariton patterns. Although this case has not been studied before, the results might be of general interest due to the widespread applications of GLV models.

Technically, we repeat the same steady-state analysis as for the homogeneous case, but this time it is much more difficult to find the solutions of the PC model due to the nonzero source term $S > 0$. In general, solving a set of multivariate polynomial equations is not a trivial task, but there are algebraic methods which can often reduce the polynomial order of the systems, and hence simplify the root finding problem. For example, this was done within a Gröbner basis formalism [102] for the related hexagonal pattern system [85]. Fortunately, in our case steady states and phase boundaries can still be calculated analytically as the roots of the set of Eqs. (3.6) with the help of computer algebra systems. The additional bifurcations for the inhomogeneous case are determined with the help of MATCONT [103], a software package for matlab, which is based on numerical continuation. First, by simple observations we can summarize a few qualitative changes for the inhomogeneous case of the PC model. The constant source term $S > 0$ in the time evolution of $A_2$ in Eqs. (3.2) breaks the inversion symmetry and also prevents a stationary $T_1$ solution in the whole parameter space since $A_2 = 0$ cannot be stationary. Moreover, the source term leads to linear growth of mode pair $A_2$, and hence it indirectly suppresses $A_1$ through the cross-saturation term. The latter interaction either results in a more asymmetric stable $F_1$ solution or in a stable $T_2$ solution, depending on the value of control parameter $S$. Interestingly, the following steady-state analysis reveals that a second four-spot pattern solution $F_2$ appears as part of a saddle-node bifurcation.

The parameter space under investigation is now the two-dimensional plane $(\delta\alpha, S)$, which is studied for the following two cases. In the case of larger self-saturation $\beta_1\beta_2 > \theta_1\theta_2$,

only one phase boundary exists, explicitly

$$S_1^*(\delta\alpha) = \beta_2 \sqrt{\frac{1+\delta\alpha}{\theta_1}}^3 - \sqrt{\frac{1+\delta\alpha}{\theta_1}}. \tag{3.25}$$

Figure 3.6(a) shows that the boundary $S_1^*$ starts from its root $\delta\alpha_1^*$ and it monotonically increases with the anisotropy parameter $\delta\alpha$. It separates the dominance region where only the stable two-spot pattern $T_2$ exists from the coexistence region where $T_2$ becomes unstable and a stable four-spot pattern $F_1$ appears. The dominance region 4 is the desired target region for the switching process. Hence, the phase boundary determines the minimum value of the control parameter to achieve complete switching. Again, Figure 3.7 shows the flow in the state space for the cases 4 and 5 and reveals unambiguous long-time dynamics towards the corresponding attractors. In the case of larger cross-saturation $\beta_1\beta_2 < \theta_1\theta_2$, an additional boundary appears; it reads

$$S_2^*(\delta\alpha) = 6\sqrt{\frac{3\left[(1+\delta\alpha)\theta_2 - \beta_1\right]^3}{\beta_1^2(\theta_1\theta_2 - \beta_1\beta_2)}}. \tag{3.26}$$

This boundary $S_2^*$ starts from its root $\delta\alpha_2^*$ and also monotonically increases with the anisotropy parameter $\delta\alpha$; see Fig. 3.6(b). Due to this second boundary, the parameter space is now separated into three regions. In the limit of large anisotropy $\delta\alpha$ (dominance regime), we recover the same regions as for the case of larger self-saturation. However, the new region between $S_2^*$ and $S_1^*$ includes the stable two-spot pattern $T_2$, the stable four-spot pattern $F_1$ and additionally the unstable four-spot pattern $F_2$. For this bistability region, the phase portrait in Fig. 3.7 case 6 shows the two basins of attraction similar to case 3b, but here with the stable four-spot pattern $F_1$ instead of the two-spot pattern $T_1$. Again, this bistability can imply hysteresis behavior which hinders the switching process. For example, entering region 6 by increasing or decreasing the control parameter leads to different steady states depending on the system's history. Coming from region 5 the system remains in stable $F_1$, whereas coming from region 4 the system remains in stable $T_2$. The case of larger cross-saturation also includes a further distinction into two subcases. Since two phase boundaries exists, the question about possible intersection points arises. Equating Eqs. (3.25) and (3.26) yields the relation

$$\delta\alpha_{\text{int}} = \frac{\beta_1\theta_1}{3\beta_1\beta_2 - 2\theta_1\theta_2} - 1 \iff \frac{\alpha_1}{\alpha_2} = \frac{\beta_1\theta_1}{3\beta_1\beta_2 - 2\theta_1\theta_2}, \tag{3.27}$$

i.e. $S_1^*$ and $S_2^*$ intersect at $\delta\alpha_{\text{int}}$ only if $1 < \frac{\theta_1\theta_2}{\beta_1\beta_2} < \frac{3}{2}$, otherwise they diverge or meet at infinity. If they intersect, the boundary $S_2^*$ vanishes (for the here considered state and parameter spaces) at the intersection point, i.e. for values $\delta\alpha > \delta\alpha_{\text{int}}$, whereas $S_1^*$ remains.
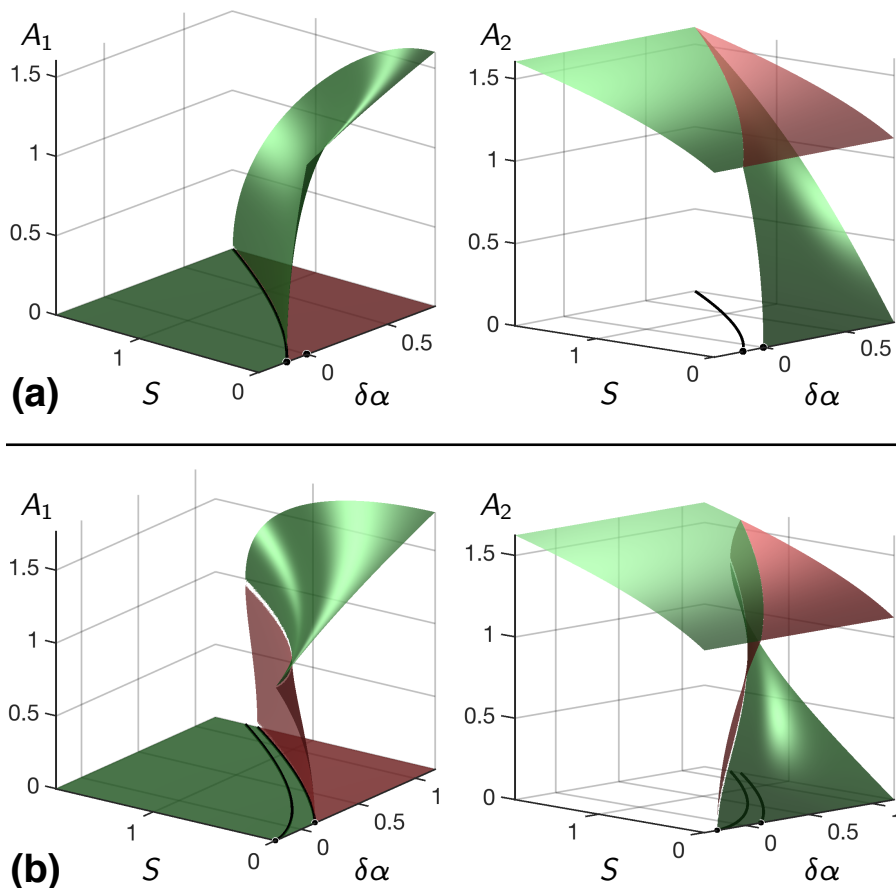
**Figure 3.8.** Equilibrium surfaces for $A_1$ and $A_2$ in the $(\delta\alpha, S)$ parameter space. Green (red) surfaces indicate stable (unstable) solutions. Black lines and dots belong to the phase boundaries projected onto the $(\delta\alpha, S)$ plane. (a) Larger self-saturation. (b) Larger cross-saturation. Reprinted from Ref. [83]

We exclude the explicit expressions for the steady states for the inhomogeneous case in this section because of their excessive length and poor readability. For the sake of completeness all solutions are listed in Appendix C. The resulting equilibrium surfaces for $A_1$ and $A_2$ on top of the $(\delta\alpha, S)$ parameter plane are shown in Fig. 3.8. For the cases of larger (a) self- and (b) cross-saturation, all possible stationary solutions and their stability properties as a function of the external control and the anisotropy are displayed. Green (red) surfaces mark stable (unstable) solutions. Figure 3.8 also acts as a two-dimensional bifurcation diagram showing the evolution of steady states in terms of existence and stability in parameter space. On the $S = 0$ line we see the pitchfork bifurcations which were already discussed in the previous section. Now, we turn our focus into the $S > 0$ direction. In the case of larger self-saturation, the supercritical pitchfork bifurcation of $A_1$ associated with $\delta\alpha_1^*$ remains stable with increasing $S$. Hence, crossing $S_1^*$ still leads to stable $T_2$ becoming unstable while stable $F_1$ appears. However, the other supercritical pitchfork bifurcation at $\delta\alpha_2^*$ vanishes for $S > 0$ since there is no longer a stationary $T_1$ solution. The situation is different in the case of larger cross-saturation; see Fig. 3.6(b)

and Fig. 3.8(b). Importantly, the inhomogeneity $S > 0$ breaks the $\mathbb{Z}_2$ symmetry of the equation of motion for $A_2$. As a result, the subcritical pitchfork bifurcation at $\delta\alpha = \delta\alpha_2^*$ on the $S = 0$ line is replaced by a saddle-node bifurcation that corresponds to boundary $S_2^*(\delta\alpha)$ in the $S > 0$ plane. In the theory of dynamical systems, this situation is often referred to as the unfolding of the pitchfork bifurcation where the external control $S$ acts as the unfolding parameter. As $S$ increases, a stable branch of the pitchfork bifurcation splits off leaving a saddle-node bifurcation behind. The latter is associated with the creation or destruction of a stable-unstable pair of fixed points. The unfolding can be observed in the evolution of the equilibrium surfaces for $A_2$ in Fig. 3.8(b). Additionally, we see a Cusp point arises which is the point where the two saddle-node boundaries $S_2^*$ and $-S_2^*$ (not shown) meet tangentially. This point is marked with letter $C$ in Fig. 3.6 and is an example of a codimension-two bifurcation which means two parameters have to be varied to trigger it. The pitchfork bifurcation for $A_1$ at $\delta\alpha_1^*$ remains for $S > 0$ because in the equation of motion for $A_1$ the inversion symmetry is conserved.

To summarize, the inhomogeneous case of the PC model is characterized by the vanishing of all $T_1$ solutions and the possible existence of a pair of four-spot solutions $F_1$ and $F_2$ with opposite stability properties. Accordingly, one of the subcritical pitchfork bifurcations unfolds into a saddle-node bifurcation. In the $(\delta\alpha, S > 0)$ parameter space, we find a dominance and coexistence region for larger self-saturation $\beta_1\beta_2 > \theta_1\theta_2$ and additionally a bistability region for larger cross-saturation $\beta_1\beta_2 < \theta_1\theta_2$. This bistability region vanishes with increasing anisotropy for parameters $1 < \theta_1\theta_2/\beta_1\beta_2 < 3/2$ or otherwise remains. The case of larger cross-saturation is problematic for the switching purposes because of the emerging saddle-node and subcritical pitchfork bifurcations. They both lead to the vanishing of a stable fixed point. As a result, the system suddenly jumps to a different fixed point and might show hysteresis behavior. Reversible on-demand switching can only work reliably if the initial (final) point in the $(\delta\alpha, S)$ parameter fall into the $T_1$ $(T_2)$ dominance region. Formally, this condition can always be satisfied by choosing sufficiently large anisotropy and control parameter values. In the previous section we showed that the physical quantities of the numerical simulations correspond to the case of larger self-saturation for the PC model. This regime has the advantage that no hysteresis can occur. In the simulations we also observe that an insufficient control beam leads to a stable four-spot pattern.

### 3.2.3. Remarks

We characterized all steady states and their stability properties in the considered state space $\mathbb{R}_{\geq 0}^2$. Furthermore, we determined all emerging bifurcations in the $(\delta\alpha, S)$ parameter space. Finally, we can also rule out any periodic solutions which might have been missed

in the steady-state analysis. A common method is to show that the dynamical system at hand can be written as a gradient of a potential function, i.e. $\mathbf{f} = \nabla V$. In a gradient system no closed orbits can exist [87, p. 199]. Here, we find that for symmetric coupling $\theta_1 = \theta_2 \equiv \theta$ a potential function can be defined as

$$V = \sum_{i=1}^{2} \frac{\alpha_i}{2} A_i^2 - \frac{\beta_i}{4} A_i^4 - \frac{\theta}{4} A_i^2 A_{i+1}^2 + S_i A_i \tag{3.28}$$

with $A_{i+2} = A_i$, $S_1 = 0$, and $S_2 \equiv S$, such that $\mathbf{f} = \nabla V$ yields the PC model given in Eq. (3.2). However, in general the coupling is asymmetric $\theta_1 \neq \theta_2$ and the PC model is no longer a gradient system. In that case, we can use Dulac's criterion to show that closed orbits are impossible [87, p. 202]. A simple version reads: If a function $g(A_1, A_2)$ exists with the property that the divergence $\nabla \cdot g\mathbf{f}$ is sign definite in the whole state space, no closed orbit can exist. Choosing $g(A_1, A_2) = (A_1 A_2)^{-1}$ and excluding the origin yields

$$\nabla \cdot g\mathbf{f} = -2 \left( \beta_1 \frac{A_1}{A_2} + \beta_2 \frac{A_2}{A_1} + \frac{S}{A_1 A_2^2} \right) < 0 \tag{3.29}$$

for the parameter range and the state space under investigation here.

Besides analyzing the steady-state structure, we also briefly comment on dynamical effects. In the PC model the effect of critical slowing down near phase boundaries occurs, i.e. the transient dynamics towards any attractor become very slow. The reason is that the real part of the Jacobian's eigenvalue that becomes zero at the boundary vanishes continuously. The critical slowing down directly corresponds to the divergence of the switching time noticed in the numerical performance study in Ref. [22]. In the case of larger self-saturation, approaching phase boundary $S_1^*$ vertically from larger values $S > S_1^*$ leads to a rapidly increasing switching time. Analogously, approaching phase boundary $\delta\alpha_2^*$ horizontally from larger values $\delta\alpha > \delta\alpha_2^*$ leads to rapidly increasing backswitching and initial buildup times. Thus, for any switching purposes a sufficient distance from the phase boundaries in parameter space is desired.

In conclusion, the PC model delivers a good qualitative description of the all-optical polariton-pattern switching process and it captures the key features observed in the full numerical simulations: Namely, minimum anisotropy to obtain stable $T_1$-pattern, minimum control to completely switch to stable $T_2$-pattern, stable $F$-pattern for finite control possible, critical slowing down near phase boundaries, and reversible on-demand switching triggered by only turning the single control beam on and off. At the same time, the PC model is simple enough for a fully analytical understanding of the underlying nonlinear dynamical system which has the form of an inhomogeneous GLV model for interspecific competition.

# 4. Creating and controlling localized vortices in spinor polariton condensates

In this chapter we investigate the multistability as well as the controllability of localized vortices in spinor polariton condensates. In contrast to the previous chapter we now consider a nonresonant excitation of a semiconductor microcavity which can lead to the formation of a polariton condensate at the ground state; see Sec. 2.2 for a detailed introduction. A captivating and well-studied phenomenon in polariton condensates is the appearance of quantized vortices [21, 55, 104, 105]. A vortex describes a state with a circular movement of the polariton fluid which is characterized by a density minimum in the center of the vortex core and a phase winding around the core quantized in multiples of $2\pi$ resulting in a central phase singularity. The corresponding integer number is commonly referred to as the topological charge. The polariton vortex results in quantized orbital angular momentum (OAM) of the emitted light from the cavity, i.e. an optical vortex [106–108], which then can be detected by measuring the phase with the help of interferometry methods. Besides arising spontaneously due to initial fluctuations and sample disorder, vortices can be imprinted resonantly into the condensate [109]. They can be pinned at a fixed position in space by the disorder potential of the sample [104]. Recent research activities aim more towards reliable creation and control of quantized vortices which is required for any application in information processing and data storage for example. In the process, the sign of the topological charge which describes the rotation direction plays the role of binary information [110]. For the application-driven approach, creation of spatially localized vortices is required. For example, external harmonic potentials can confine vortices inside polariton condensates [111]. Another promising method is to make use of the optically induced potential which acts on the condensate mediated by repulsive interaction with the incoherent reservoir [58, 112, 113]. A ring-shaped pump profile can trap a vortex inside the pump-induced potential at a predefined position [114, 115]. In this chapter we also employ the ring-shaped excitation condition. Due to the circular symmetry, vortex states spontaneously form with clockwise or counterclockwise rotation direction

(positive or negative sign of the topological charge) depending on initial fluctuations. It was found that the rotation direction of these localized vortices can be switched by a short nonresonant pulse [116]. Additionally, instead of a full ring small pump spots in a hexagonal arrangement can be utilized to trap the condensate. This setup has the advantage that different sizes and positions of pump spots can explicitly break the chiral symmetry in order to create a predefined vortex state [56]. Importantly, for localized vortices the topological charges can be measured via an OAM sorting setup [115, 117].

Taking the polariton polarization dependence into account, different types of vortices can occur in two-component condensates. In particular, the literature distinguishes between full-vortices (FVs) which are characterized by same-sign topological charges in both circular polarization components and spin-vortices (SVs) with opposite-sign topological charges in the two components. A special case are the so-called half-vortices (HVs) [9, 52, 118–122]. They are vortex states where only one of the circular polarization components carries nonzero OAM. Importantly, the component with nonzero OAM has a vanishing density in the vortex core while the other component with zero OAM still has a finite density at the same central position. This leads to a circular polarization peak in the region of the HV core. Besides in polariton condensates, HVs have been studied theoretically and experimentally in various systems, e.g. in atomic condensates [123–126], in superconductors [127], and in $^3$He superfluids [128, 129].

Here, we investigate different localized vortices under linearly polarized ring-shaped excitation. For the scalar case (without polarization dependence), it was shown that vortex states with different topological charges can be stable under the same excitation conditions [130]. Including the polarization degree of freedom leads to a rich multistability of different half-, full-, and spin-vortices, which is presented in the first part of this chapter. We further explore the effect of TE-TM splitting which results in a reshaping of the spatial density and phase profiles in dependence of the involved topological charges. In the second part, we present a method to switch between differently polarized HVs by using a short resonant pulse based on the attractive cross-interaction between different circularly polarized polaritons. Finally, this switching method is applied to higher-order HV states, resulting in a multi-level switching scheme. This chapter is mainly based on our results published in Ref. [131].

# 4.1. Multistability of half-, full- and spin-vortices in ring-shaped pump profiles

In this section we investigate the multistability of different vortex states under linearly polarized ring-shaped excitation. In the numerical simulations, we use an $x$-linearly polarized continuous-wave pump with the following ring-shaped profile

$$P_+(\mathbf{r}) = P_-(\mathbf{r}) = P_0 \frac{\mathbf{r}^2}{\mathrm{w}_p^2} e^{-\mathbf{r}^2/\mathrm{w}_p^2}, \tag{4.1}$$

with radius $\mathrm{w}_p$ and pump intensity $P_0$. In the spinor GP model Eqs. (2.28, 2.29) we assume an incoherent but polarized reservoir which transfers the pump's linear polarization to the condensate; see Sec. 2.2. This assumption is reasonable in the case of linearly polarized excitation and has been commonly used in theoretical [61, 62] as well as in experimental works [11, 52, 53] where the same spinor GP model was used. We also fix the following system parameters $m_{\mathrm{eff}} = 10^{-4} m_e$ ($m_e$ is the free electron mass), $\gamma_c = 0.15$ ps$^{-1}$, $\gamma_r = 1.5\gamma_c$, $R = 0.01$ ps$^{-1}$ $\mu$m$^2$, $g_c = 3 \times 10^{-3}$ meV $\mu$m$^2$, $g_{\mathrm{x}} = 0.2 g_c$, $g_r = 2 g_c$, and $P_0 = 100$ $\mu$m$^{-2}$ps$^{-1} = 5 P_{\mathrm{thr}}$ with condensation threshold value $P_{\mathrm{thr}}$. All numerical results are obtained by solving Eqs. (2.28, 2.29) via a fourth-order Runge-Kutta algorithm on a finite, two-dimensional spatial grid of length $L = 100\,\mu$m sampled by $N = 501$ discrete points in each direction. Figure 4.1(a) shows a sketch of the ring-shaped nonresonant pump exciting the polariton condensate inside the semiconductor microcavity. In this setup, the pump has a two-fold role: It replenishes the reservoir which feeds the condensate and also acts as an optically induced potential for the condensate mediated via the reservoir density;
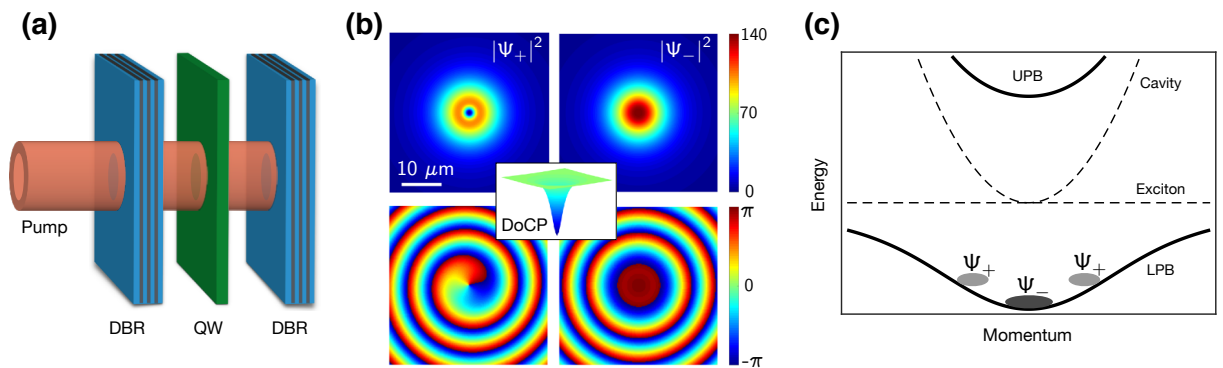


**Figure 4.1.** (a) Sketch of the semiconductor microcavity excited by an $x$-linearly polarized ring-shaped pump. (b) Densities in $\mu$m$^{-2}$ and phase profiles of the two circular polarization components for a HV state $(-1, 0)$. Pump radius is $w_p = 4.5$ $\mu$m and TE-TM splitting is set to zero here, i.e. $\Delta_{\mathrm{LT}} = 0$. (c) Sketch of the polariton dispersion relation, alongside with the bare exciton and cavity dispersion. Schematically shown are the condensate components of the HV state shown in (b). Reprinted from Ref. [131].

see Sec. 2.2. Additionally, the condensate itself also reshapes the reservoir creating a feedback loop. Stable stationary states require a balance between the loss and gain which is achieved by this aforementioned feedback between the condensate and the reservoir. This allows multiple different localized states being stable under the same excitation condition. The ring-shaped pump can trap the condensate inside the ring radius due to the optically induced potential, forming localized states fixed at the pump's position. Due to the circular symmetry, vortex states can form from initial noise or being resonantly imprinted. These vortex states are stabilized by the balance of the condensate between the confinement in the optically induced potential and the radially outgoing propagation due to the repulsive polariton-polariton interaction [56, 132]. As a result, the condensate reshapes the reservoir which is more pronounced when the vortex carries a higher topological charge with a larger radius [130]. In general, localized vortices excited by a ring-shaped pump can possibly be stable when the vortex radius is smaller than the pump's ring radius. Otherwise, the vortex becomes unstable and spirals out of the condensate due to the outgoing propagation, similar to non-localized vortices under Gaussian spot excitation [111].

Figure 4.1(b), shows the density and phase distribution of a localized HV state under linearly polarized excitation as an example. There is a vortex with topological charge $m_+ = -1$ in the $\Psi_+$ component and a fundamental mode with $m_- = 0$ in the $\Psi_-$ component. The vortex is characterized by a density minimum in the core and a $2\pi$ phase winding around the core indicating circular movement of the polariton condensate, since the condensate velocity is proportional to the phase gradient [133]

$$\mathbf{v}_\pm(\mathbf{r}) = \frac{\hbar}{m_{\mathrm{eff}}} \nabla \varphi_\pm(\mathbf{r}), \tag{4.2}$$

where $\varphi_\pm(\mathbf{r}) \equiv \arg \psi_\pm(\mathbf{r})$ is the phase in two-dimensional real space of the corresponding condensate component. The relation in Eq. (4.2) allows us to read the polariton's qualitative motion directly from the condensate phase distributions. Within the region defined by the pump's ring-shaped maximum, the azimuthal phase gradient around the vortex core is approximately linear, whereas it becomes rapidly twisted while crossing the ring-shaped maximum due to the radial outflow of the condensate. Moving further away from the pump region, the phase gradient mostly points in the radial direction indicating the outgoing propagation of the polariton condensate. Furthermore, the inset in Fig. 4.1(b) shows the degree of circular polarization in the microcavity plane near the vortex core; see definition in Eq. (4.3) further below. The HV core is characterized by a peak of circular polarization due to the vanishing density in the center of only one component. Figure 4.1(c) shows a sketch of the condensate components from panel (b) alongside the polariton dispersion relation.
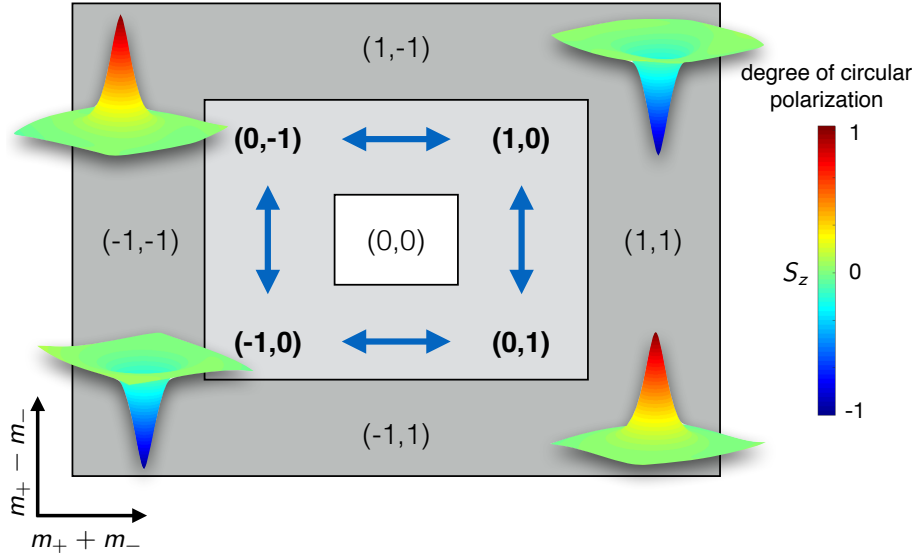
**Figure 4.2.** Overview of vortex multistability for linearly polarized ring-shaped excitation with $P_0 = 5P_{\text{thr}}$ and $w_p = 4.5$ $\mu$m. Notation refers to the topological charges $(m_+, m_-) \in \mathbb{Z}^2$. The rectangles define increasing energy tiers. The four elementary HVs are marked in bold and their degree of circular polarization in the core region of the cavity plane is shown. The blue arrows mark possible switching between right and left HVs which is presented in the next section. Adapted from Ref. [131].

All possible localized states excited by the ring-shaped pump defined in Eq. (4.1) can be characterized by two topological charges $(m_+, m_-) \in \mathbb{Z}^2$. Besides the ground state $(0, 0)$ (non-vortex state), the system can also be in a vortex state. The first excited state is then a HV state where there is a vortex in only one circular polarization component, i.e. $(\pm 1, 0)$ or $(0, \pm 1)$. The other possibilities are FV states, where there are same-sign vortices in both components $(\pm 1, \pm 1)$, or SV states, where there are opposite-sign vortices in both components $(\pm 1, \mp 1)$. Note that there is an alternative common notation of spinor vortices in the linear polarization basis. It uses polarization and phase rotation winding numbers $(k, m)$ [9, 120]. They are related to our notation via $k = (m_- - m_+)/2$ and $m = (m_+ + m_-)/2$.

Figure 4.2 shows an overview of all the different localized vortex states which are stable for the same linearly polarized ring-shaped excitation with $P_0 = 5P_{\text{thr}}$ and $w_p = 4.5$ $\mu$m. Here, we also include a finite TE-TM splitting value of $\Delta_{\text{LT}} = 0.025$ meV$\mu$m$^2$. In the numerical simulations, all solutions can arise from initial noise or be directly imprinted as the initial condition. In principle, the growing rectangles in Fig. 4.2 define increasing discrete energy tiers, but the degeneracy within a rectangle is lifted in the presence of TE-TM splitting. The four HVs are marked in bold. In contrast to the ground state, FV,

and SV states, HV states are purely circularly polarized in the core due to the nonzero density in the center of one component and mostly linearly polarized elsewhere. We can distinguish between right-circularly polarized HVs $(0, \pm 1)$ and left-circularly polarized HVs $(\pm 1, 0)$ and refer to them as right and left HVs in the following. Additionally, the corners of Fig. 4.2 show the degree of circular polarization in the cavity plane near the core for the four HVs, defined as the pseudospin component (Stokes parameter)

$$S_z = \frac{|\psi_+| - |\psi_-|}{|\psi_+| + |\psi_-|}. \tag{4.3}$$

Accordingly, a value of $S_z = +1$ ($S_z = -1$) refers to right- (left-) circular polarization. For a HV state, the pseudospin component is characterized by a narrow circular polarization peak $S_z = \pm 1$ in the core center and linear polarization elsewhere. Thus, in principle a localized HV state can be detected by simply measuring the polarization-resolved intensity in the core region, instead of extracting the whole phase information, which can be an advantage in experiments. As mentioned above, increasing the pump radius stabilizes higher-order vortices while destabilizing the fundamental mode or lower-order vortices. Figure 4.2 characterizes the vortex multistability for a given set of excitation conditions. For larger pump radii, a similar multistability figure would obtain more outer rectangles indicating stability of higher-order vortices while the most inner rectangles would vanish because of the fundamental mode and lower-order vortices become unstable.

## 4.1.1. Effects of TE-TM splitting

There is quite a debate [134–136] about the stability of HVs in the presence of TE-TM splitting in the corresponding conservative system (without loss and gain). It has been found that HVs can be stable under the influence of TE-TM splitting but their density and phase distributions become warped due to the polarization-dependent effective mass [135, 137, 138]. Reference [135] gives an implicit equation to calculate the warping in the corresponding conservative system. They find that the condensate's circular phases depend nonlinearly on the azimuthal angle. Hence, the reshaping of the two-dimensional spatial vortex profiles goes along with the breaking of the cylindrical symmetry. In the driven dissipative system excited by a linearly polarized ring-shaped pump, we find that localized HVs are stable in the presence of TE-TM splitting but also become deformed. To additionally demonstrate the stability of the HV solutions, we study the influence of a static disorder potential and dynamical noise in Appendix D. The HV solution is very robust in the presence of these external perturbations over a time interval of at least 10 ns. Furthermore, a large variety of higher-order vortex states can be stable depending on the pump's radius and intensity. This includes the appearance of vortex states carrying

topological charges $|m_\pm| > 1$ with increasing pump radius. Note that higher-order localized vortex states might be topologically unstable but dynamically stable [56, 109]. That means a higher-order vortex splits into singly charged vortices with spatially very close but separated vortex cores, and the overall vorticity within the ring-shaped pump area remains the same. In addition to having different topological charges and different energies, vortex states can now be arranged into distinct symmetries groups corresponding to their approximate real-space geometry. Figure 4.3 shows an overview of the first six symmetry groups alongside with density and phase distributions of the corresponding vortex states. They are arranged by the difference $\Delta m \equiv m_+ - m_-$ (vertical) and the sum $m_+ + m_-$ (horizontal) of their topological charges. Each relevant square shows the densities $|\psi_+|^2$ and $|\psi_-|^2$ in the upper row and the corresponding phases $\varphi_+ \equiv \arg \psi_+$ and $\varphi_- \equiv \arg \psi_-$ in the bottom row. Their color bars are given at the bottom of the figure. The blue-shaded diagonal lines separate the regions with different pump radii, which are given at the bottom of the figure. We find that the difference $\Delta m$ determines the real-space symmetry. Starting from the cylindrical symmetry characterized by the orthogonal group $O(2)$ for $\Delta m = -2$, all remaining discrete symmetries are given by the dihedral group $D_n$ where $n = |\Delta m + 2|$. For $n \geq 3$ the dihedral group is the symmetry group of a regular polygon. In the case $n = 2$ it corresponds to the symmetry of a non-equilateral rectangle and in the case $n = 1$ to the symmetry of an isosceles triangle. In the literature, the geometry of the four elementary HVs is often referred to as lemon and star. Note that the orientation of the different geometries rotates over time resulting from the coupled components having different energies. The time $\Delta T$ needed for the smallest rotation angle which preserves the spatial orientation can be calculated from the frequencies of the two polarization components $\omega_+$ and $\omega_-$

$$\Delta T = \frac{2\pi}{|\omega_+ - \omega_-|}. \tag{4.4}$$

For example, higher-order HV state $(2, 0)$ has a square symmetry and frequencies of about $\omega_+ \approx 0.74$ THz and $\omega_+ \approx 0.65$ THz; see real-space spectra in Fig. 4.8(c). Hence, after every $\Delta T \approx 70$ ps the square has the same orientation in two-dimensional real space.
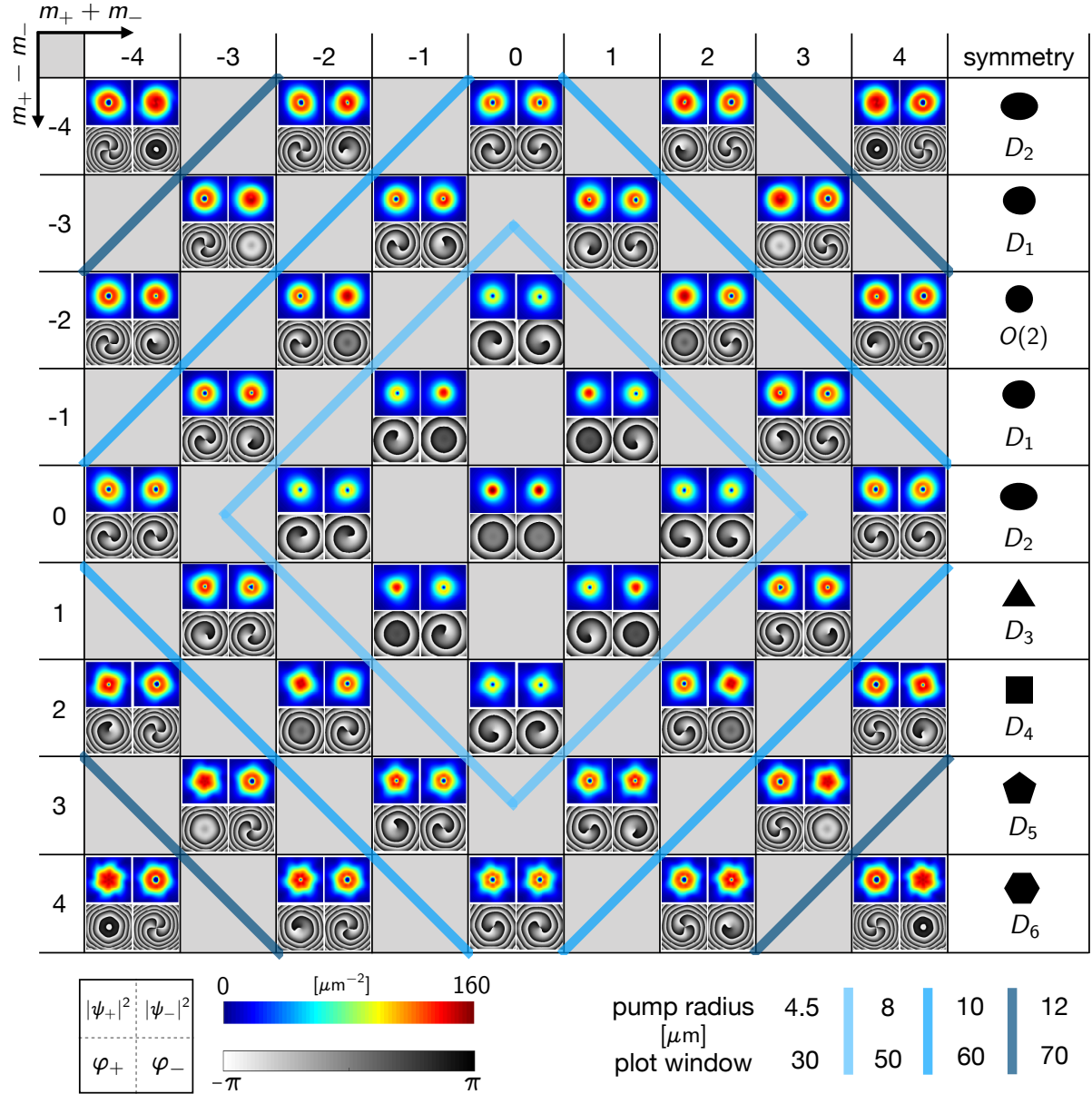
**Figure 4.3.** Overview of the first seven groups of the approximate real-space symmetry for different stable vortex states. The states are arranged by the difference $m_+ - m_-$ (vertical) and the sum $m_+ + m_-$ (horizontal) of their topological charges. The symmetries are given by orthogonal group $O(2)$ for $\Delta m = -2$ and by the dihedral group $D_n$ where $n = |\Delta m + 2|$ for $\Delta m \neq -2$. For each state, densities and phase distributions of the circular polarization components are shown. Their color bars are located at the bottom. Blue-shaded diagonal lines mark the regions of different pump radii and plot window sizes.

## 4.2. Reversal of circular polarization at the center of half-vortices

In this section we present a method to switch between left and right HVs using a circularly polarized resonant control pulse. The underlying mechanism is based on the attractive cross-interaction between differently polarized polaritons. This switching scheme results in the reversible and on-demand circular polarization reversal of the HV cores, which can be interpreted as switching of binary information. Similar vortex core dynamics where the magnetization is reversed via an external field are commonly studied in magnetic systems [139–142] as promising candidates for binary-data storage devices with ultra-fast control. Finally, we apply the method to higher-order HV states and demonstrate multi-level switching.

All following HV switching processes are triggered by a ring-shaped resonant control pulse

$$E_{\pm}(\mathbf{r}) = E_0 \mathbf{r}^2 e^{-\mathbf{r}^2/\mathrm{w}_c^2} e^{im_c\phi} e^{-i\omega_c t} e^{-(t-t_0)^2/\mathrm{w}_t^2} \tag{4.5}$$

which carries a topological charge $m_c$. Here, $\phi$ denotes the azimuthal angle of the two-dimensional coordinate system. Additionally, $\mathrm{w}_c$ is the spatial radius and $\omega_c$ is the frequency of the control pulse which is set to be nearly resonant with the corresponding condensate frequency. The parameters $t_0$ and $\mathrm{w}_t$ determine the Gaussian envelop in the time domain. Figure 4.4 shows an example of the HV switching process. We start with a stable stationary left HV state $(-1,0)$. Figure 4.4(a) shows the density and phase distributions of the initial HV state with topological charge $m_+ = -1$ in the $\psi_+$ component and a fundamental mode with topological charge $m_- = 0$ in the $\psi_-$ component resulting in a left-circular polarization peak in the core region as displayed in the inset. Figure 4.4(b) shows the corresponding central horizontal cut through the real-space spectrum for both condensate components. Now, a resonant control pulse $E_-$ is applied to the $\psi_-$ component which is also ring-shaped and carries topological charge $m_c = -1$ and its density and phase distributions in real space are shown in Fig. 4.4(c). This control pulse imprints a vortex into the $\psi_-$ component. Simultaneously, we observe that the vortex in the $\psi_+$ component becomes unstable and spirals out of the condensate, triggering a transition into the ground state with zero topological charge. Overall, this results in the stable stationary right HV state $(0,-1)$, which is now right-circularly polarized in the core region. Figure 4.4(d) shows the density and phase distributions of the final HV state $(0,-1)$ as well as the corresponding degree of circular polarization in the inset. Figure 4.4(e) shows the corresponding central horizontal cut through the real-space spectrum for both condensate components after the control pulse. In total, this switching process results in the reversal of circular polarization the core region. Additionally, we can observe that the reshaping of the
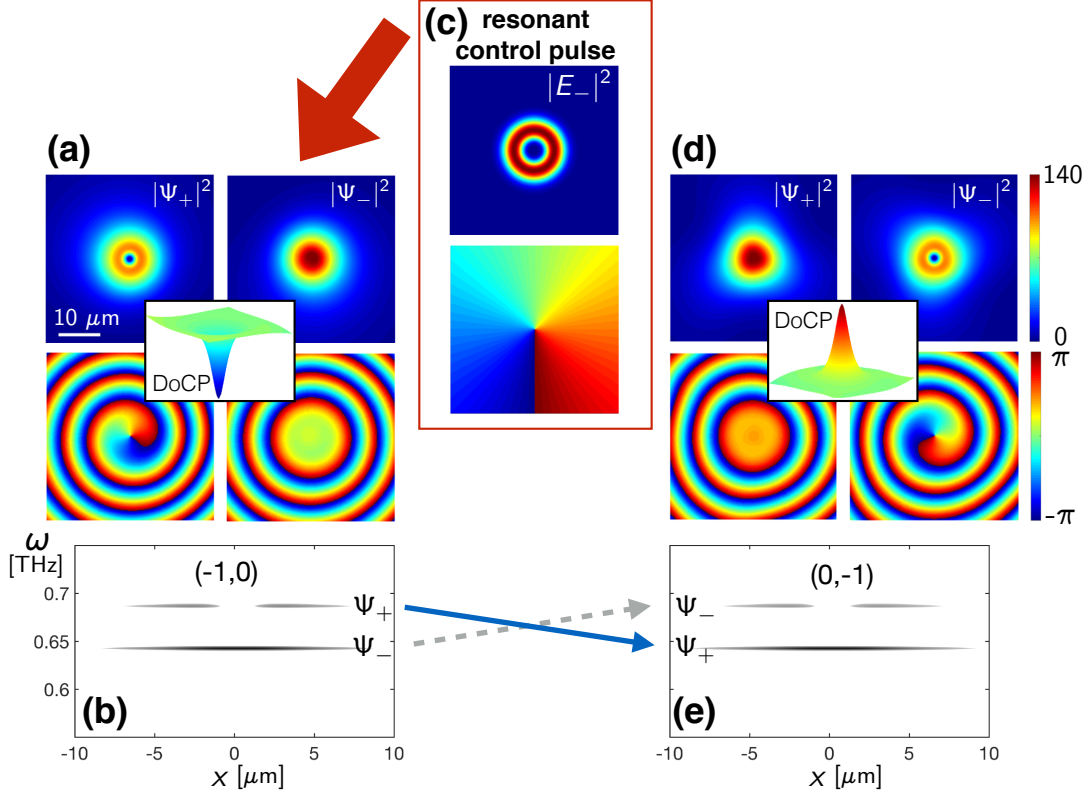
**Figure 4.4.** Example of a HV switching process from $(-1,0)$ to $(0,-1)$ and the corresponding circular polarization reversal of the HV core. (a) Density ($\mu\text{m}^{-2}$) and phase distributions of the initial left HV state $(-1,0)$. Inset shows the circular polarization peak $S_z = -1$ in the core region. (b) Central horizontal cut through the real-space spectrum for both condensate components before the control pulse. (c) Density (arbitrary units) and phase distribution of the circularly polarized resonant control pulse. (d) Density ($\mu\text{m}^{-2}$) and phase distributions of the final right HV state $(0,-1)$. Inset shows the circular polarization peak $S_z = +1$ in the core region. (e) Central horizontal cut through the real-space spectrum for both condensate components after the control pulse. Grey arrow marks imprinting of a vortex by the control pulse in the $\psi_-$ component. Solid blue arrow indicates the simultaneous transition from a vortex to a fundamental mode in the $\psi_+$ component. Parameters are $w_p = 4.5~\mu\text{m}$, $w_c = 6~\mu\text{m}$, $E_0 = 2.5$ meV $\mu\text{m}^{-3}$ and $w_t = 35$ ps, $\omega_c = 0.7$ THz. Reprinted from Ref. [131].

density and phase distributions due to TE-TM splitting changes from lemon ($D_1$) to star ($D_3$) geometry; see previous Sec. 4.1. In the real-space spectrum, this polarization reversal can be interpreted as the simultaneous inversion of two coupled two-level systems; see arrows in Figs. 4.4(b,e). The dashed grey arrow indicates the imprinting of a vortex by the control pulse in the $\psi_-$ component, whereas the solid blue arrow marks the simultaneous destabilization and removal of the vortex in the $\psi_+$ component.

In addition, Figure 4.5 shows three different time snapshots of the density distributions (in $\mu\text{m}^{-2}$) of both components during the switching process for the purpose of visualization. Here, the control pulse's temporal envelop is centered at $t_0 = 0$ on the time scale displayed. Black arrows indicate schematically the motion of the vortex cores. In Figure 4.5(b) the
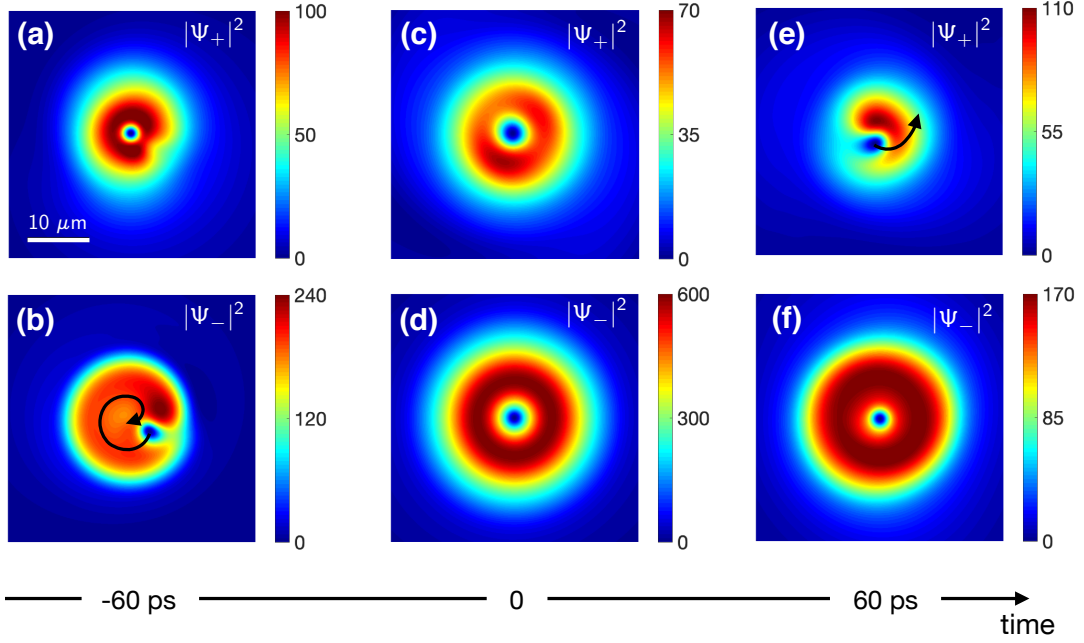
**Figure 4.5.** Time snapshots of the density distributions in $\mu\text{m}^{-2}$ of both polarization components during the switching process. The maximum of the temporal envelop of the control pulse is centered at $t = 0$. This time corresponds to panels (c) and (d). Panels (a) and (b) refer to a relative time of $t = -60$ ps. In panel (b) the inwards moving vortex due to the control pulse is clearly visible. Panels (e) and (f) correspond to a relative time of $t = 60$ ps. Panel (e) shows the outward moving vortex due to the destabilization by the attractive cross-interaction. Black arrows show schematically the motion of the vortex cores. Reprinted from Ref. [131].

vortex in the $\psi_-$ spirals into the condensate due to resonant imprinting, while there is still a vortex in the $\psi_+$ component; see Fig. 4.5(a). In Figure 4.5(e) the vortex in the $\psi_+$ spirals out of the condensate, while the resonant vortex imprinting in the $\psi_-$ is completed; see Fig. 4.5(f). Importantly, the HV switching can be detected by simply measuring the polarization resolved intensities in the core region, making complete phase extraction via interferometric methods unnecessary. In this particular example, the switching process is completed within about 150 ps with a control pulse temporal width of $\text{w}_t = 35$ ps. All possible switching combinations between the four elementary HVs are marked by the blue double arrows in Fig. 4.2.

In order to reveal the underlying mechanism of the switching process described above we have to look at the transient effective potential landscape. Earlier, we learned that the stability of localized vortex states strongly depends on the confinement in the effective potential mediated via the condensate-reservoir interaction. Hence, we have to investigate the effective potential landscape experienced by the $\psi_+$ component during the control pulse duration. Figure 4.6 shows a one-dimensional central cut of the contributions of the effective potential of the $\psi_+$ component at three different points in time during the switching process: (a) Initial HV state without control pulse, (b) intermediate state
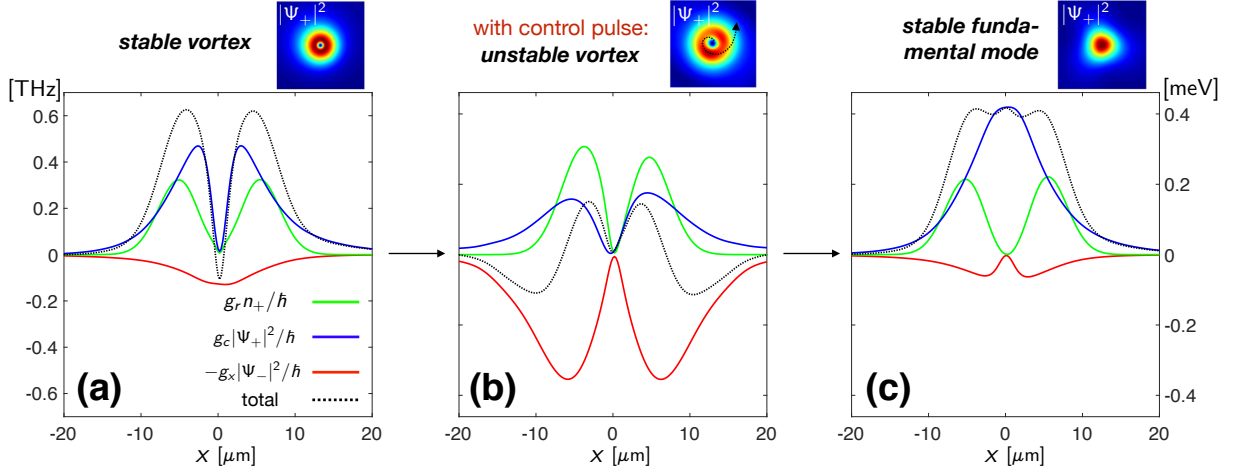
**Figure 4.6.** One-dimensional central cut through the effective potential landscape of the $\psi_+$ component during the HV switching process introduced in Fig. 4.4 at three different points in time: (a) Initial state. (b) Intermediate state at the maximum intensity of the control pulse. (c) Final state. Green lines show the reservoir-induced potential. Blue lines correspond to the repulsive self-interaction that is proportional to the density of the $\psi_+$ component itself. Red lines mark the attractive cross-interaction. Panel (b) reveals the destabilization of the vortex in the $\psi_+$ component due to the attractive cross interaction caused by the pulse induced density in the $\psi_-$ component. The vortex becomes unstable and spirals out of the condensate, schematically indicated by the black arrow in the density inset in panel (b). Adapted from Ref. [131].

with control pulse, and (c) final HV state without control pulse. Above each panel, the corresponding density (in arbitrary units) of the $\psi_+$ component is displayed. Figure 4.6(a) shows the potential landscape for the initial stable HV state $(-1, 0)$. The blue line is proportional to the density of the $\psi_+$ component and the position of its maximum is well located inside the reservoir-induced potential, shown by the green line. The red line shows the attractive potential due to the cross-interaction which is proportional to the density of the $\psi_-$ component. The attractive potential additionally supports the trapping of the vortex inside the reservoir-induced potential. Now we apply the control pulse and have a look at the intermediate state when the control pulse maximum is reached; see Fig. 4.6(b) and also Fig. 4.5(c,d). The control pulse imprints a vortex into the $\psi_-$ component and simultaneously reshapes the effective potential landscape of the $\psi_+$ component. Due to the attractive cross-interaction the $\psi_+$ component becomes spatially broader and the condensate-reservoir balance is suppressed. Hence, the vortex in the $\psi_+$ component is no longer confined. It becomes unstable and rapidly spirals out of the condensate due to the potential imbalance. This leaves behind a fundamental mode with zero topological charge $m_+ = 0$ in the $\psi_+$ component as shown in Fig. 4.6(c) and a vortex with topological charge $m_- = -1$ in the $\psi_-$ component. Effectively, the $\psi_+$ component transitions into the ground state, while the $\psi_-$ component is excited into the vortex state. The OAM is switched from one component to the other and the circular polarization peak in the core is reversed.
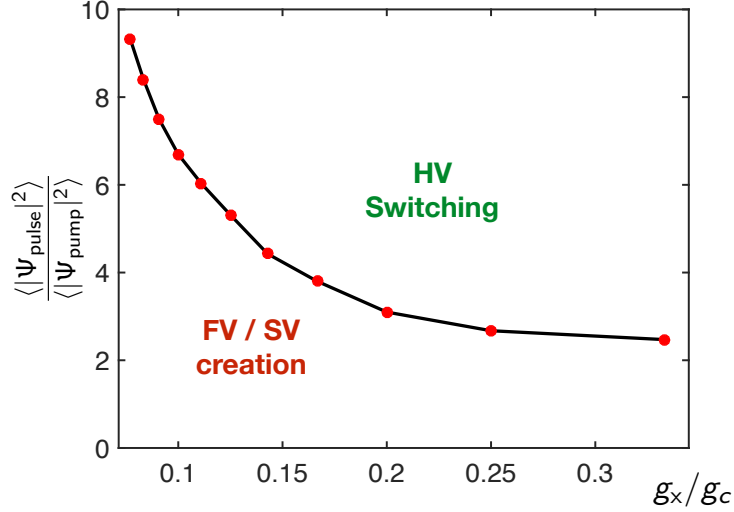
**Figure 4.7.** Time-integrated density induced by the control pulse $\langle|\psi_{\mathrm{pulse}}|^2\rangle$ normalized to the time-integrated pump-induced density $\langle|\psi_{\mathrm{pump}}|^2\rangle$ as a function of the interaction strength ratio $g_x/g_c$ in order to induce HV switching. Above the curve, HV switching works reliable, whereas below the curve a FV or SV state is created by trivial vortex imprinting. Line is shown to guide the eye. Reprinted from Ref. [131].

To summarize, the HV switching process depends on the shape and magnitude of the cross-polarized density which is induced by the resonant control pulse. Importantly, the results do not strongly depend on the absolute values of the control pulse's amplitude and duration, but more on the time-integrated pulse-induced density. In particular, there is no OAM conservation rule involved as it was found in similar but resonantly excited polariton systems [143, 144]. If the radius, intensity and duration of the control pulse are sufficient, the vortex in the cross-polarized component becomes unstable in the transient effective potential landscape and is removed from the condensate during the pulse duration. If they are not sufficient, a vortex is imprinted in the corresponding component, but the vortex in the cross-polarized component does not get removed but instead remains, resulting in a stable FV or SV state. Figure 4.7 shows the time-integrated density induced by the control pulse, explicitly

$$\langle|\psi_{\mathrm{pulse}}|^2\rangle \equiv \int_{-\mathrm{w}_t}^{+\mathrm{w}_t} dt \ |\psi(t_0)|^2 \ e^{-(t-t_0)^2/\mathrm{w}_t^2} = \sqrt{\pi}\mathrm{w}_t|\psi(t_0)|^2\mathrm{erf}(1), \tag{4.6}$$

as a function of the interaction strength ratio between cross- and co-polarized polaritons $g_x/g_c$ in order to observe the HV switching. It is normalized to the time-integrated density induced by the pump $\langle|\psi_{\mathrm{pump}}|^2\rangle$ without control pulse. Typically, the interaction strength of cross-polarized polaritons $g_x$ is about one order of magnitude smaller than the interaction strength of co-polarized polaritons $g_c$ in our excitation conditions [46, 145, 146]. Figure 4.7

shows that smaller interaction strength ratios can be compensated by a stronger control pulse. Above the curve the HV switching works, whereas below the curve the control pulse just imprints a vortex but the cross-polarized component does not change and remains in a vortex state, resulting in a FV or SV state.

## 4.2.1. Multi-level switching with higher-order HV states

Finally, we apply the switching scheme which was introduced above for the four elementary HVs to higher-order localized HV states. Increasing the pump radius can in principle stabilize solutions with higher topological charges, i.e. $|m_\pm| > 1$. Up to a certain threshold radius, the lower-order vortex states and the fundamental mode remain also stable [114,130]. We define higher-order HVs as states with one component in the ground state with zero topological charge and the other component in a higher order vortex state with an absolute value of the topological charge larger than one, e.g. $(m_+, 0)$ or $(0, m_-)$. Employing the switching method to such higher-order HV states raises the question about the possible outcomes. Interestingly, we find that the order of the initial vortex component can be reduced step wise down to the ground state depending on the intensity and duration of the control pulse. For example, an initial stable higher-order HV state $(m_+, 0)$ with $|m_+| > 1$ can be switched via a resonant control pulse $E_-$ carrying topological charge $m_c$ to all states $(m'_+, m_c)$ with $|m'_+| = |m_+| - j$ for $j \in [0\ |m_+|]$. This enables multi-level switching configurations. As an example we start with higher-order HV state $(2, 0)$ as shown in Fig. 4.8. Now, applying the resonant control pulse with $m_c = -1$ to the the $\psi_-$ component can lead to two possible outcomes (in addition to just imprinting a vortex). For a shorter ($w_t = 15$ ps) control pulse the vortex in the $\psi_+$ component reduces its topological charge to $m_+ = 1$. However, for a longer ($w_t = 35$ ps) control pulse the vortex in the $\psi_+$ component gets removed completely resulting in the ground state. The transient dynamics reveal that the higher-order vortex state first gets decomposed during the switching into singly charged vortices and they, one after the other, spiral out of the condensate. In principle, the higher-order HV states could provide a platform for various multi-level switching combinations.
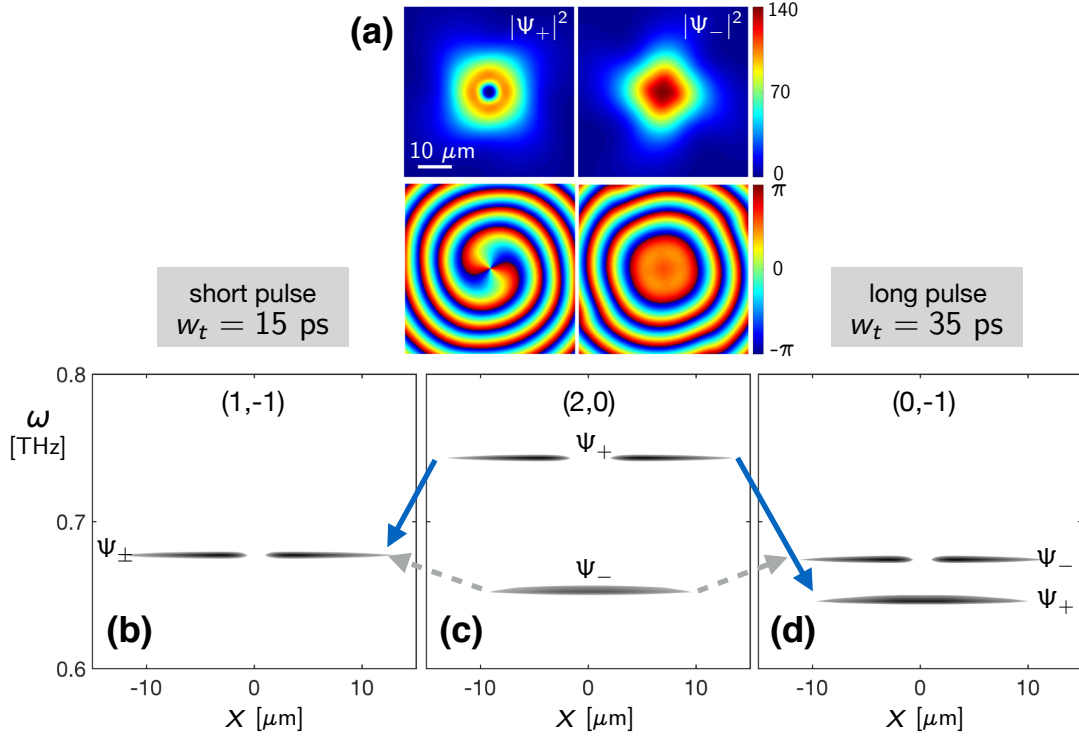
**Figure 4.8.** Multi-level higher-order HV switching. (a) Densities ($\mu$m$^{-2}$) and phase distributions of a higher-order HV state $(2, 0)$. (c) Corresponding central cut through the real-space spectrum. This state is a starting point for a transition to two possible target states depending on the control pulse's intensity and duration. The target states' spectra are shown in panel (b) and (d). (b) For a shorter pulse duration of $w_t = 15$ ps, a vortex $m_- = -1$ is imprinted in the $\psi_-$ component, while the topological charge in the $\psi_+$ component is reduced by one to $m_+ = 1$. (d) For a longer pulse duration of $w_t = 35$ ps, a vortex $m_- = -1$ is imprinted in the $\psi_-$ component, while the topological charge in the $\psi_+$ component is reduced by two to $m_+ = 0$. Parameters are $w_p = 6$ $\mu$m, $w_c = 7$ $\mu$m, $E_0 = 2.5$ meV $\mu$m$^{-3}$, $\omega_c = 0.7$ THz. Reprinted from Ref. [131].

# 5. Quantifying quantum coherence in polariton condensates

In the final chapter we investigate polaritons in semiconductor microcavities from a different perspective by adding the layer of statistical properties. In previous chapters, we studied various functional aspects based on the classical evolution of the expectation value of a coherent polariton field. Now, we additionally take classical and quantum fluctuations into account and use a phase-space method to calculate expectation values. This access to the statistical properties allows us to study different measures of coherence in polariton condensates across the threshold. Importantly, we are able to determine the quantum coherence which corresponds to the amount of Fock-state superpositions within the polariton condensate and provides a resource in the sense of quantum information protocols [147, 148]. The maximum value found in the numerical simulations is in good agreement with the experimental data. Additionally, we propose and demonstrate a method to increase the quantum coherence via pump shaping. Finally, we perform a full quantum state reconstruction in terms of the density matrix in Fock space with the help of so-called pattern functions and study the dynamics of the off-diagonal elements for linear and orbital angular momentum modes within the polariton condensate.

This chapter is partly based on our cooperation with the group of Marc Aßmann at TU Dortmund University who carried out the quantum optical experiments and Jan Sperling at Paderborn University who provided the theoretical background of quantum information science. We established this interdisciplinary work in the publication Ref. [43] where we studied quantum coherence in polariton condensates and the results are presented in the first section below.

## 5.1. Quantum coherence under spatially broad excitation

In this section we numerically investigate the quantum coherence of a polariton condensate under spatially broad excitation, compare it to experimental results and propose a method to enhance the coherence via pump shaping. Polariton condensates have been studied as

an example of spontaneous buildup of macroscopic coherence under nonresonant excitation [149–154]. The degree of spatial and temporal coherence is usually characterized by normalized correlation functions. Most prominently, the first- and second-order correlation functions $g^{(1)}$ and $g^{(2)}$ capture phase correlations in space and time and intensity correlations, respectively. Their behavior across the condensation threshold have been used to investigate the underlying phase transition [31–33]. Nevertheless, $g^{(1)}$ does not contain information of the state being classical or quantum, and $g^{(2)}$ only relates to particle-number distribution, i.e. the diagonal elements of the density operator in Fock space. In order to fill this gap, we investigate a form of quantum coherence which quantifies the amount of superpositions of Fock states (particle-number states) in the polariton condensate. Technically, the quantum coherence corresponds to the amount of off-diagonal contributions of the density operator in Fock space, i.e. the extent of quantum superpositions of particle-number states resulting in the non-diagonal form of the density operator under investigation. Since polaritons are promising candidates for hybrid light-matter interface applications, quantifying the quantum coherence in polariton condensates is highly relevant because it resembles a resource for possible quantum information tasks [147, 148]. To this end, we employ the truncated Wigner approximation, a phase-space method which was derived in detail in Sec. 2.3. It relies on the Wigner representation $W(\psi)$ of a bosonic field operator $\hat{\psi}(\mathbf{r})$ and the mapping of an approximated Fokker-Planck equation for $W$ onto a stochastic partial differential equation for the corresponding phase-space variables $\psi(\mathbf{r})$. The latter are then used to sample the phase space and to calculate expectation values as averages over many different noise realizations. The Wigner representation implies symmetric operator ordering. Hence, the general formula for the expectation values can be expressed as

$$\left\langle \left( \hat{\psi}^{\dagger m} \hat{\psi}^n \right)_{\text{sym}} \right\rangle \approx \frac{1}{N_s} \sum_{i=1}^{N_s} \psi_i^{*m} \psi_i^n \equiv \overline{\psi^{*m} \psi^n}, \tag{5.1}$$

where the index 'sym' stands for symmetrized, $N_s$ is the sample size, and overlined terms mark stochastic averages in the following.

### 5.1.1. Numerical results

For the simulations, the nonresonant continuous-wave pump has a broad super-Gaussian spatial profile, $P(\mathbf{r}) = P_0 \exp\left[-\mathbf{r}^4/w^4\right]$ with the width $w = 65$ $\mu$m. We also fix the following system parameters: $m_{\text{eff}} = 10^{-4} m_e$ ($m_e$ is the free electron mass), $\gamma_c = 0.2$ ps$^{-1}$, $\gamma_r = 1.5\gamma_c$, $R = 0.015$ ps$^{-1}$ $\mu$m$^2$, $g_c = 6 \times 10^{-3}$ meV $\mu$m$^2$, and $g_r = 2g_c$. The pump profile and the parameters are chosen with regard to the experimental realization; see Sec. 5.1.2. The same semiconductor microcavity sample has been described by similar parameters in previous work [116]. For the following numerical results, we use the condensation threshold pump
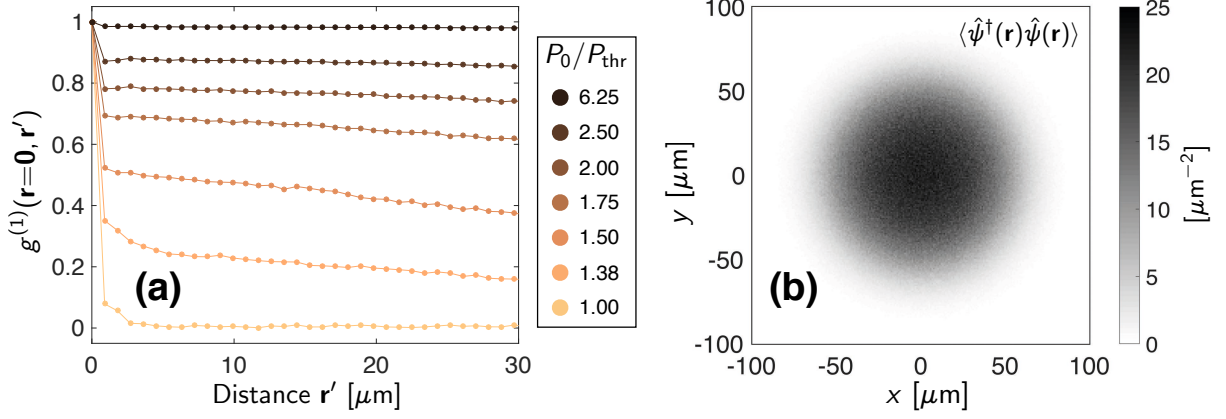
**Figure 5.1.** (a) Simulated first-order, equal-time spatial coherence as a function of the distance from the center of the excitation spot for increasing pump intensities, evidencing the creation of phase coherence across the excitation spot. Reprinted from [43]. (b) Single-time snapshot of the real-space density expectation values above the condensation threshold, here $P = 2\,P_{\text{thr}}$.

intensity for the corresponding spatially homogeneous system $P_{\text{thr}} = \gamma_c \gamma_r / R = 4 \text{ ps}^{-1}\,\mu\text{m}^{-2}$ as the reference pump value. All numerical results are obtained by solving Eqs. (2.45) and (2.47) via a fourth-order stochastic Runge-Kutta algorithm [155] on a finite two-dimensional spatial grid of length $L = 230.4\,\mu\text{m}$ sampled by $N^2 = 256^2$ discrete points, which satisfies the truncation condition in Eq. (2.48). Below threshold, we use 300 realizations each, and 200 above to ensure convergence. Every realization is evolved over a time interval of 4 ns with a fixed time step of $\Delta t = 0.04$ ps. Finally, expectation values are additionally averaged in time as steady-state mean. Displayed error bars accounting for the statistical errors indicate the standard deviations and the corresponding propagated errors. Details are given in Appendix E.

Figure 5.1(b) depicts a single-time snapshot of the real-space density expectation value for $P_0 = 2\,P_{\text{thr}}$. It resembles the super-Gaussian pump profile with a nearly homogeneous density in the center. Figure 5.1(a) shows the equal-time first-order correlation function,

$$g^{(1)}(\mathbf{r}, \mathbf{r}') = \frac{\langle \hat{\psi}^\dagger(\mathbf{r})\hat{\psi}(\mathbf{r}')\rangle}{\sqrt{\langle \hat{\psi}^\dagger(\mathbf{r})\hat{\psi}(\mathbf{r})\rangle \langle \hat{\psi}^\dagger(\mathbf{r}')\hat{\psi}(\mathbf{r}')\rangle}} = \frac{\overline{\psi^*(\mathbf{r})\psi(\mathbf{r}')} - \frac{\delta_{\mathbf{rr}'}}{2\Delta V}}{\sqrt{\left(\overline{|\psi(\mathbf{r})|^2} - \frac{1}{2\Delta V}\right)\left(\overline{|\psi(\mathbf{r}')|^2} - \frac{1}{2\Delta V}\right)}}, \quad (5.2)$$

as a function of the distance from the center of the excitation spot for different pump intensities. The first-order correlation increases significantly for increasing pump intensities and reflects the buildup of spatial phase coherence in the condensate. Additionally to the overall growth, the spatial decay of $g^{(1)}$ becomes weaker for each increasing pump intensity. Far above threshold, the phase coherence becomes almost $g^{(1)} \approx 1$ across the excitation spot; see $P_0 = 6.25\,P_{\text{thr}}$ in Fig. 5.2(a).

In order to study properties of the condensate mode at zero momentum, we transform the

field operators from real to momentum space, which corresponds to the far-field emission of the cavity

$$\hat{b}_{\mathbf{k}} = \frac{\Delta V}{\sqrt{V}} \sum_{\mathbf{r}} e^{-i\mathbf{k}\mathbf{r}} \hat{\psi}(\mathbf{r}). \tag{5.3}$$

The resulting polariton ladder operators obey the bosonic commutation relation

$$\left[ \hat{b}_{\mathbf{k}}, \hat{b}_{\mathbf{k}'}^{\dagger} \right] = \delta_{\mathbf{k}\mathbf{k}'}. \tag{5.4}$$

Figure 5.2(a) shows the mean occupation number in momentum space for a pump intensity $P_0 = 2\,P_{\mathrm{thr}}$ above threshold. For each mode, the expectation value is calculated according to Eq. (5.1) as

$$\langle \hat{n}_{\mathbf{k}} \rangle = \overline{|\beta_{\mathbf{k}}|^2} - \tfrac{1}{2}, \tag{5.5}$$

where $\beta$ is the complex amplitude in phase space that corresponds to the operator $\hat{b}$. The occupation has a peak at the $k \equiv |\mathbf{k}| = 0$ and a finite width due to the pump shape and the repulsive nonlinearity. To account for this finite width, we average the mode occupation in the vicinity of the zero-momentum mode. Technically, we consider a small square in $k$-space around $k = 0$ as marked in red in Fig. 5.2(a), which contains $N_p$ discrete modes. To this end, we define the polariton condensate excitation number mean and variance

$$\langle \hat{n}_c \rangle \;=\; \frac{\langle \hat{N} \rangle}{N_p}, \tag{5.6a}$$

$$\langle (\Delta \hat{n}_c)^2 \rangle \;=\; \frac{\langle (\Delta \hat{N})^2 \rangle}{N_p}. \tag{5.6b}$$

The total occupation number operator of all modes inside the square then reads

$$\hat{N} = \sum_{j=1}^{N_p} \hat{b}_j^{\dagger} \hat{b}_j, \tag{5.7}$$

where $\hat{b}_j \equiv \hat{b}_{\mathbf{k}_j}$ and $\mathbf{k}_j$ denotes a mode inside the square. Within our phase-space formalism, the first and second moments can be calculated by symmetrizing all operator products, which results in [68]

$$\langle \hat{N} \rangle \;=\; \sum_{j=1}^{N_p} \left( \overline{|\beta_j|^2} - \tfrac{1}{2} \right), \tag{5.8a}$$

$$\langle (\Delta \hat{N})^2 \rangle \;=\; \langle \hat{N}^2 \rangle - \langle \hat{N} \rangle^2 = \sum_{j=1}^{N_p} \left( \overline{|\beta_j|^4} - \overline{|\beta_j|^2} \right) - \sum_{j=1}^{N_p} \left( \overline{|\beta_j|^2} - \tfrac{1}{2} \right)^2. \tag{5.8b}$$

The mean polariton excitation number and its variance for different excitation powers are
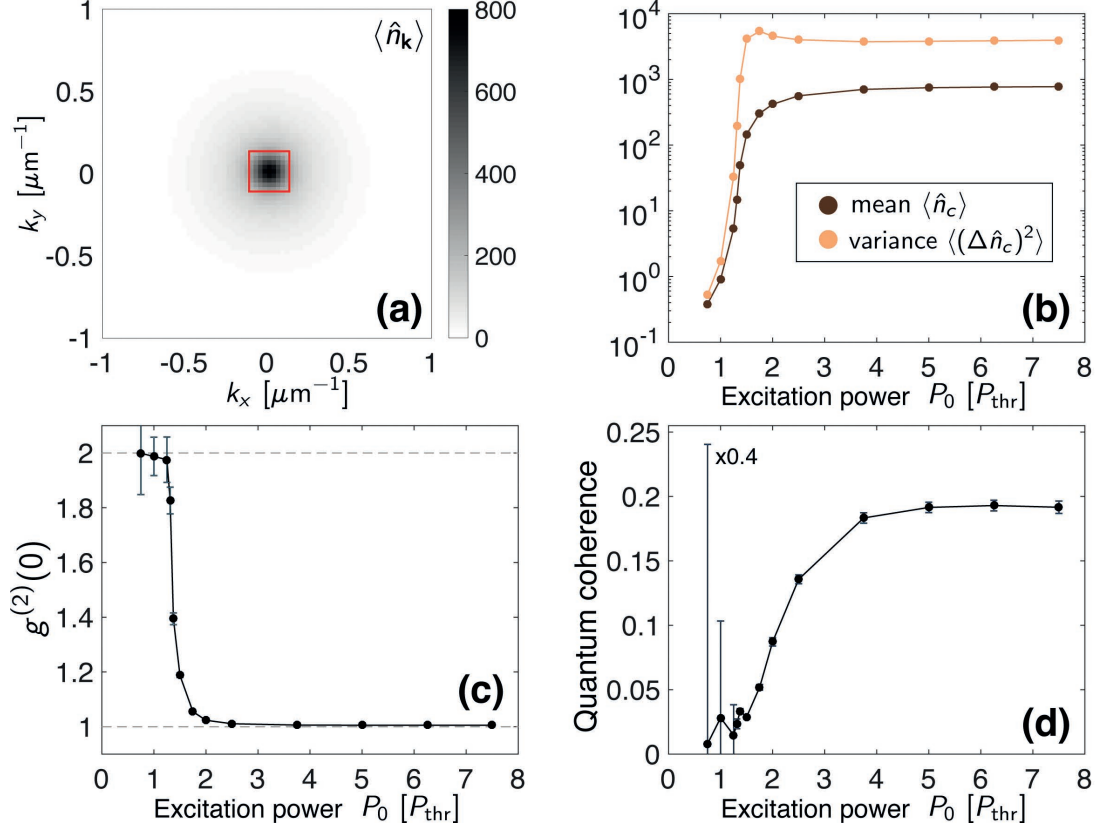
**Figure 5.2.** (a) Single-time snapshot of the $k$-space density expectation values above the condensation threshold, $P_0 = 2\,P_{\text{thr}}$. The red square indicates the selected signal area for the excitation number averaging. (b) Mean and variance of the averaged polariton excitation number as a function of the excitation power. (c) Equal-time second-order correlation function $g^{(2)}(\tau = 0)$ as a function of the excitation power, showing the transition from a thermal state to a coherent state. (d) Amount of quantum coherence $\mathscr{C}$ as a function of the excitation power. Reprinted from [43].

depicted in Fig. 5.2(b). They both increase rapidly above threshold until a saturation value is reached at about $P_0 \gtrsim 4\,P_{\text{thr}}$. Mean and variance both approach their saturation value asymptotically, but the former from below and the latter from above. The fluctuations in the condensate occupation number can be quantified via the equal-time second-order correlation function

$$g^{(2)}(\tau{=}0) = \frac{\langle \hat{n}_c^2 \rangle - \langle \hat{n}_c \rangle}{\langle \hat{n}_c \rangle^2} = 1 + \frac{\langle (\Delta \hat{n}_c)^2 \rangle - \langle \hat{n}_c \rangle}{\langle \hat{n}_c \rangle^2}. \tag{5.9}$$

Figure 5.2(c) shows $g^{(2)}$ as a function of the excitation power. Starting from a value $g^{(2)} = 2$ below threshold, indicating a thermal distribution, the second-order correlation rapidly decreases towards $g^{(2)} \approx 1$ above threshold, indicating a Poissonian distribution that corresponds to a coherent state. While $g^{(2)}$ gives information about the excitation number distribution, which corresponds to the diagonal elements of the density operator in Fock space, it does not contain any insight into the off-diagonal contributions. This

gap is filled by introducing the quantum coherence as a measure of the amount of off-diagonal elements [156]. To describe the state of the condensate between the thermal and coherent limit, we adapt the concept of a displaced thermal state, commonly used in quantum optics [157]. A displaced thermal state describes a thermal state which is coherently displaced in phase space. Hence, it consists of a thermal ($\bar{n}$) and coherent ($|\alpha_0|^2$) contribution such that mean and variance are given by [154]

$$\langle \hat{n}_c \rangle \;=\; \bar{n} + |\alpha_0|^2, \tag{5.10a}$$

$$\langle (\Delta \hat{n}_c)^2 \rangle \;=\; |\alpha_0|^2 (2\bar{n} + 1) + \bar{n}^2 + \bar{n}. \tag{5.10b}$$

The assumption of a displaced thermal state is further supported by explicit density matrix reconstruction in the next Sec. 5.3. Equations (5.10a) and (5.10b) allow us to calculate the thermal and coherent contributions from which we can finally determine the quantum coherence. Let $\hat{\rho} = \sum_{m,n \in \mathbb{N}} \rho_{m,n} |m\rangle\langle n|$ be the system's density operator in Fock space and $\hat{\rho}_{\mathrm{inc}} = \sum_{n \in \mathbb{N}} p_n |n\rangle\langle n|$ its closest incoherent counterpart with the same diagonal elements but no off-diagonal elements [158]. Here, we use the following definition of the quantum coherence [156]

$$\mathscr{C}(\hat{\rho}) = \sum_{\substack{mn \in \mathbb{N} \\ m \neq n}} |\rho_{m,n}|^2 = \|\hat{\rho} - \hat{\rho}_{\mathrm{inc}}\|_{\mathrm{HS}}^2 = \mathrm{tr}(\hat{\rho}^2) - \mathrm{tr}(\hat{\rho}_{\mathrm{inc}}^2), \tag{5.11}$$

which is the sum of all squared absolute values of the off-diagonal elements; equivalently, it is the Hilbert-Schmitt distance between the system's density operator and its incoherent version. For the class of displaced thermal states which have Gaussian phase-space distributions, the quantum coherence can be calculated explicitly via [43]

$$\mathscr{C}(\hat{\rho}) = \frac{1 - \exp\left[-\frac{2|\alpha_0|^2}{(\bar{n}+1)^2 - \bar{n}^2}\right] I_0\left[\frac{2|\alpha_0|^2}{(\bar{n}+1)^2 - \bar{n}^2}\right]}{(\bar{n}+1)^2 - \bar{n}^2}, \tag{5.12}$$

where $I_0(\lambda) = (2\pi)^{-1} \int_0^{2\pi} d\varphi \exp\left[\lambda \cos(\varphi)\right]$ is the zeroth-order modified Bessel function of the first kind. The quantum coherence is bound between the values zero (thermal state) and one (infinitely displaced coherent state). Expressing the second-order correlation function also in terms of thermal and coherent contributions using Eqs. (5.10a) and (5.10b) yields

$$g^{(2)} = 2 - \left(1 + \frac{\bar{n}}{|\alpha_0|^2}\right)^{-2}, \tag{5.13}$$

and allows us to compare both properties for displaced thermal states. Figure 5.3 shows (a) the second-order correlation function $g^{(2)}(|\alpha_0|^2, \bar{n})$ as well as (b) the quantum coherence $\mathscr{C}(|\alpha_0|^2, \bar{n})$ for a displaced thermal state as a function of the thermal and coherent
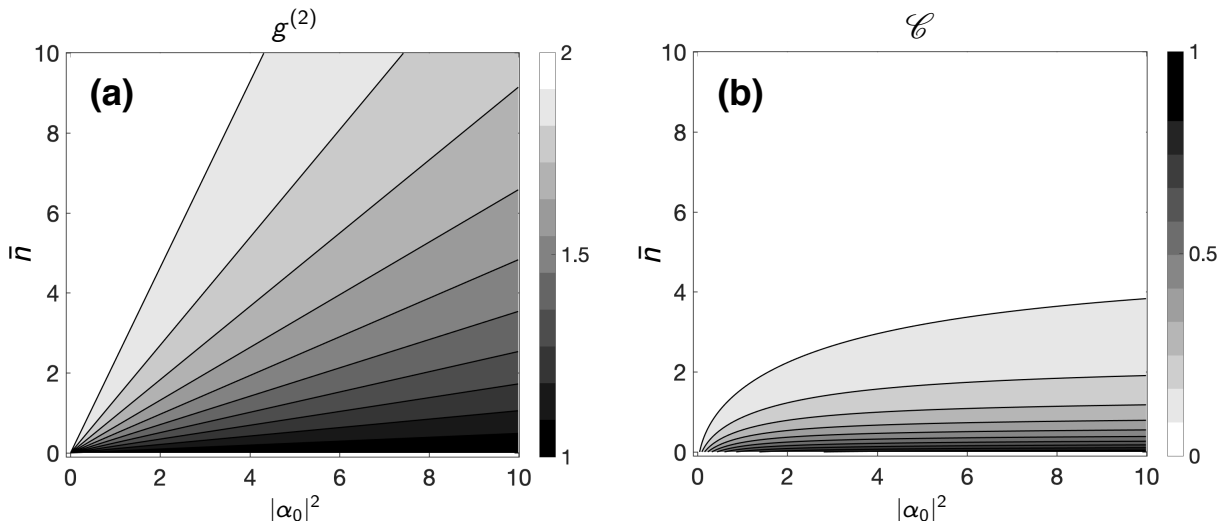
**Figure 5.3.** (a) Second-order correlation function $g^{(2)}$ and (b) quantum coherence $\mathscr{C}$ of a displaced thermal state as a function of the coherent and thermal contributions. Both show monotonic behavior but significantly different transitions between their limits. Reprinted from Ref. [43].

contributions. Both depend monotonically on $|\alpha_0|^2$ and $\bar{n}$; see also Appendix C in Ref. [43]. Importantly, their different behavior becomes obvious: $g^{(2)}$ decreases much faster from 2 towards 1 than $\mathscr{C}$ increases from 0 to 1 while the coherent amplitude $|\alpha_0|^2$ is increased or the thermal contribution $\bar{n}$ is reduced.

Coming back to our numerical simulations, Figure 5.2(d) shows the quantum coherence defined in Eq. (5.12) as a function of the excitation power. Below and also slightly above threshold the values are close to zero. The quantum coherence starts to increase significantly at about $P_0 \approx 2\,P_{\mathrm{thr}}$ and reaches a plateau for $P_0 \gtrsim 4\,P_{\mathrm{thr}}$ of

$$\mathscr{C} \approx 0.2. \tag{5.14}$$

This value indicates a significant amount of quantum coherence which results from polariton number-state superpositions within the condensate. Importantly, this property cannot be captured by the first- or second-order correlation function. A direct comparison between the numerical results for $\mathscr{C}$ and $g^{(2)}$ also shows their different behaviors as the excitation power increases; see Fig. 5.2(c,d). While $g^{(2)}$ reaches its minimum already at twice the threshold power, the quantum coherence saturates only at four to five times the threshold power. The quantum coherence's saturation value depends on the system parameters. In general, the quantum coherence takes values between zero and one, depending on the ration between the coherent and thermal contributions. Figure 5.4 shows the relative change of this saturation value in dependence of the interaction strength $g_c$ and the net reservoir in-scattering rate $R$ for a fixed pump intensity far above the threshold of $P_0 = 7.5\,P_{\mathrm{thr}}$.
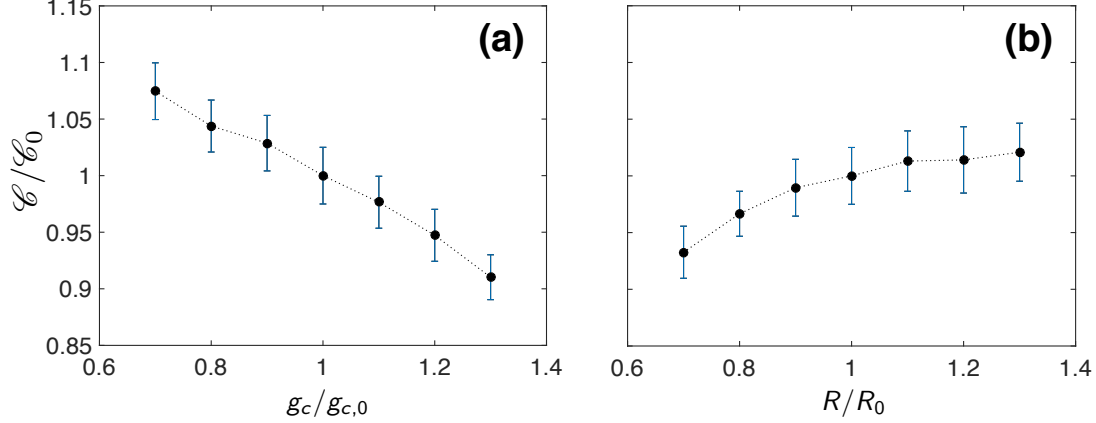
**Figure 5.4.** Relative changes of the quantum coherence saturation value in dependence of relative changes of (a) interaction strength $g_c$ (b) net reservoir in-scattering rate $R$. Reference values are given above at the beginning of this section, i.e. $\mathscr{C}_0 = 0.1916$, $g_{c,0} = 6 \times 10^{-3}$ meV $\mu$m$^2$, and $R_0 = 0.015$ ps$^{-1}$ $\mu$m$^2$. Sample size for each data point is $N_s = 100$.

Both axes show relative values normalized to the initially used parameters which were defined above and are marked with index 0, i.e. $\mathscr{C}_0 = 0.1916$, $g_{c,0} = 6 \times 10^{-3}$ meV $\mu$m$^2$, and $R_0 = 0.015$ ps$^{-1}$ $\mu$m$^2$. Overall, the quantum coherence is not very sensitive to changes of the two parameters up to 30%. It increases slightly for decreasing interaction strength and increasing scattering rate. In the regime far above threshold, the mean polariton occupation around $k = 0$ decreases with increasing interaction strength due to an enhanced radial outflow away from the excitation spot [57]. Additionally, the repulsive nonlinearity leads to polariton-polariton scattering in and out of the selected condensate mode being induced by the fluctuations. As a result, the ratio between coherent and thermal contributions declines, and the quantum coherence decreases for increasing interaction strength parameter $g_c$ in the regime far above threshold; see Fig. 5.4(a). Technically, we find that the condensate mean occupation $\langle \hat{n}_c \rangle$ reduces faster than the reduction of the corresponding variance $\langle (\Delta \hat{n}_c)^2 \rangle$ with increasing interaction strength. The condensation rate parameter $R$ determines the threshold pump intensity and also the intensity where the saturation value of the quantum coherence is reached. On the one hand, decreasing $R$ leads to decreasing quantum coherence since it shifts the saturated regime to higher excitation powers. On the other hand, increasing $R$ barely increases the saturation value, as depicted in Fig. 5.4(b).

## 5.1.2. Comparison with experimental results

While in the numerical investigation we directly simulated the polariton state (which has no direct physical representation in terms of a measurable quantity), in experiments, the emitted light from the semiconductor microcavity is measured. Assuming a linear coupling between the polariton state and the out-coupled light results in a rescaling of the density
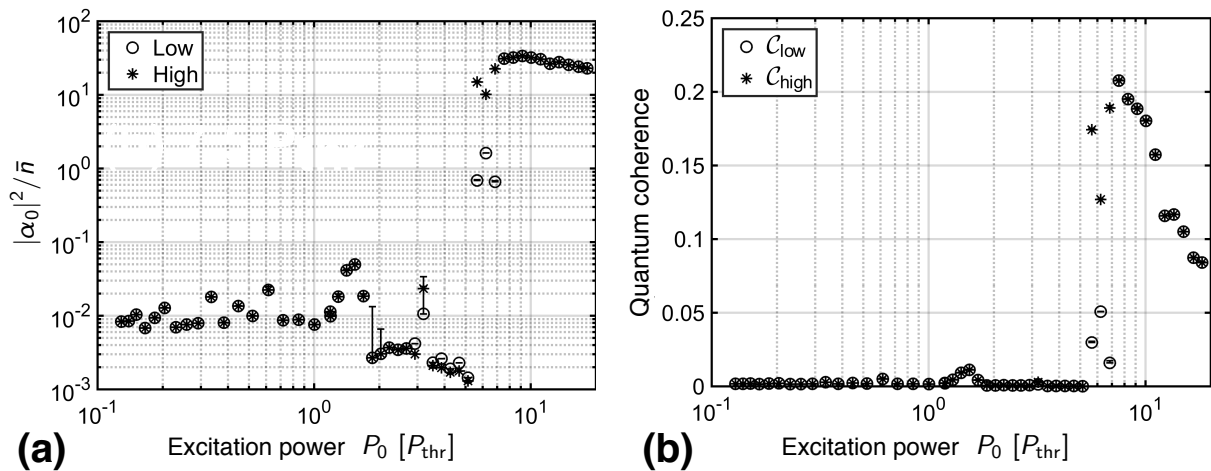
**Figure 5.5.** Experimental results of our cooperation partners at TU Dortmund; see text for details. Circles and stars correspond to bistable states with low and high emission, respectively, which were both measured in the experiment and then evaluated separately. (a) Ratio between coherent ($|\alpha_0|^2$) and thermal ($\bar{n}$) photon-number contributions as a function of the excitation power. (b) Quantum coherence as a function of the excitation power. Reprinted from [43].

operator [43], and hence a transfer of the coherence properties. The experiment to measure quantum coherence in polariton condensates was carried out by Carolin Lüders at TU Dortmund in the group of Marc Aßmann. The experimental results, together with the comparison with the numerical simulations, were published in our joint work [43] and is briefly recapitulated below.

The experimental setup is based on a balanced homodyne detection scheme [159, 160]. In a 10 K cryostat, the semiconductor microcavity sample is excited with a nonresonant continuous-wave pump laser with a Gaussian shape and a width of 70 $\mu$m, favoring condensation at the zero-momentum mode [24, 57]. The experimental pump profile is comparable to the profile used in the numerical simulations in Sec. 5.1 above. The difference can be denoted by the normalized Euclidean distance of about $\|P_{\mathrm{num}} - P_{\mathrm{exp}}\|/(\|P_{\mathrm{num}}\| \, \|P_{\mathrm{exp}}\|)^{1/2} \approx 0.46$. The light emission from the cavity is filtered in $k$-space in the vicinity of $k = 0$ mechanically via a pinhole and optically via the overlap with the local oscillator. From the measured field quadratures, the phase-averaged Husimi $Q$ function can be reconstructed. Fitting the experimental data to the phase-averaged Husimi function of a displaced thermal state gives the coherent ($|\alpha_0|^2$) and thermal ($\bar{n}$) photon number contributions. Finally, the latter are used to calculate the quantum coherence according to Eq. (5.12). Figure 5.5 shows parts of the experimental results published in Ref. [43]. Figure 5.5(a) shows the ratio between coherent ($|\alpha_0|^2$) and thermal ($\bar{n}$) photon number contributions in dependence of the excitation power. Below threshold the emission is dominated by the thermal contribution, and no quantum coherence is present as depicted in Fig. 5.5(b). Around the threshold power $P_0 \approx P_{\mathrm{thr}}$, the coherent photon number starts to increase but falls again rapidly

at about two times the threshold power. In this excitation power range, scattering into higher-$k$ states can be observed, preventing condensation into the zero-momentum mode. The coherent-to-thermal ratio and quantum coherence stay low until about $P_0 \approx 5 \, P_{\mathrm{thr}}$, where they start to rise rapidly. In this intermediate regime, the polarization-resolved measurement shows a competition between the two linear polarization modes. Far above threshold ($P_0 > 7.5 \, P_{\mathrm{thr}}$), the coherent contribution outweighs the thermal contribution significantly, resulting in a maximum quantum coherence of about $\mathscr{C} = 0.208 \pm 0.001$, which is in good agreement with the saturation value from the numerical simulations ($\mathscr{C} \approx 0.2$). In contrast to the numerical results, the maximum value of quantum coherence does not become saturated at even higher pump powers, but instead decreases again. This reduction happens due to increased polariton-polariton scattering and heating of the sample. The main differences between the experimental and numerical results can be explained by the effects of sample heating, sample disorder and polarization competition, which are not covered in the numerical model. Overall, experiment and simulation show a good agreement of the maximum amount of quantum coherence in the polariton condensate under spatially broad excitation. In conclusion, our joint theory-experiment work has shown how to quantify quantum coherence in polariton condensates —as an example of hybrid light-matter systems— by directly simulating the hybrid quasi-particle state via a phase-space method and by indirectly probing for particle superpositions via balanced homodyne detection of the emitted light field.

## 5.1.3. Enhancing quantum coherence via pump shaping

In the previous Sections 5.1.1 and 5.1.2, we studied the quantum coherence of a polariton condensate under a wide super-Gaussian pump spot ($w = 65 \, \mu$m). We found that the quantum coherence increases across the condensation threshold and plateaus at about $\mathscr{C} \approx 0.2$. Naturally, the question arises whether we can increase this saturation value for a fixed set of parameters; equivalently for a specific semiconductor microcavity sample in the experiment. A straightforward idea is to spatially separate the reservoir from the condensate with the goal to reduce fluctuations while still maintaining sufficient gain for the condensate to form. This separation can be realized by using ring-shaped pump profiles which are accessible in experiments by using spatial light modulators for example [115]. Polariton condensates with spatially separated reservoirs have been studied in various different contexts, e.g. optical traps and condensate formation [112], polarization dynamics [53] and measuring the polariton-polariton interaction strength [113]. In order to systematically study the effect of the pump shaping on the quantum coherence, we

define the following pump profile:

$$P(\mathbf{r}) = P_0 \left( e^{-\mathbf{r}^4/w^4} - \delta e^{-\mathbf{r}^4/(\frac{w}{2})^4} \right),$$ (5.15)

where the parameter $\delta$ is the reduction of the intensity in the center of the pump spot, i.e. $P(\mathbf{r} = \mathbf{0}) = P_0(1 - \delta)$. The width of the inner ring is fixed at $w/2$, but it is a variable parameter in general. Figure 5.6(a) shows the pump profiles for different reduction values $\delta$. While $\delta$ increases, the corresponding pump-induced reservoir acts more and more as a cylindrical trapping potential for the condensate. The ring-shaped reservoir has different competing effects on the formation of the condensate. On the one hand, less reservoir induced fluctuations are expected since maximum density region of the condensate is spatially separated from the maximum density region of the reservoir. Additionally, the trapping potential leads to a suppression of the condensate outflow, and hence to a pronounced zero-momentum mode. Both effects are expected to have an increasing effect on the quantum coherence. On the other hand, as the depth of the potential well increases, Bessel-like solutions form instead of a single mode at zero momentum. In position space, a small cylindrical shaped density in the center of the trap arises, and hence rings in momentum space. Additionally, initial noise-induced vortices can be trapped in the potential and even the zero-momentum state can become unstable and transition into a stable vortex array [161]. Overall, we expect a non-monotonous behavior of the quantum coherence with increasing $\delta$ (the pump profile becomes more ring-shaped) because of the competition of the various effects described above.

To account for the aforementioned effects, we focus on the observables of the single mode $k = 0$ instead of a larger region around it in order to study the enhancement due to the narrowing of the condensate emission. Experimentally, the width of emission can be selected by using differently sized pinholes and by adjusting the width of the local oscillator in the balanced homodyne detection scheme. To prevent the trapping of initially created vortices, we start each simulation with a super-Gaussian profile and increase $\delta$ over time until the target value is reached. Observables are then calculated after evolution to a stable steady state with the desired $\delta$ value. Figure 5.6(b) shows the simulation results for the quantum coherence as a function of the reduction parameter $\delta$ for different pump intensities above threshold. Additionally, the figure shows the single-mode density $|\psi_{k=0}(\delta)|^2$ normalized to the density with no reduction $|\psi_{k=0}(\delta{=}0)|^2$ which was calculated with a corresponding mean-field model. As expected, the quantum coherence shows a non-monotonous behavior. First, it decreases as $\delta$ increases, evidencing that small inhomogeneous reshaping of the pump profile has a negative effect (small perturbation) on the coherence of the single mode at $k = 0$. Minima form approximately at the inflection points (maximum slopes) of the corresponding density ratios. From here, the coherence
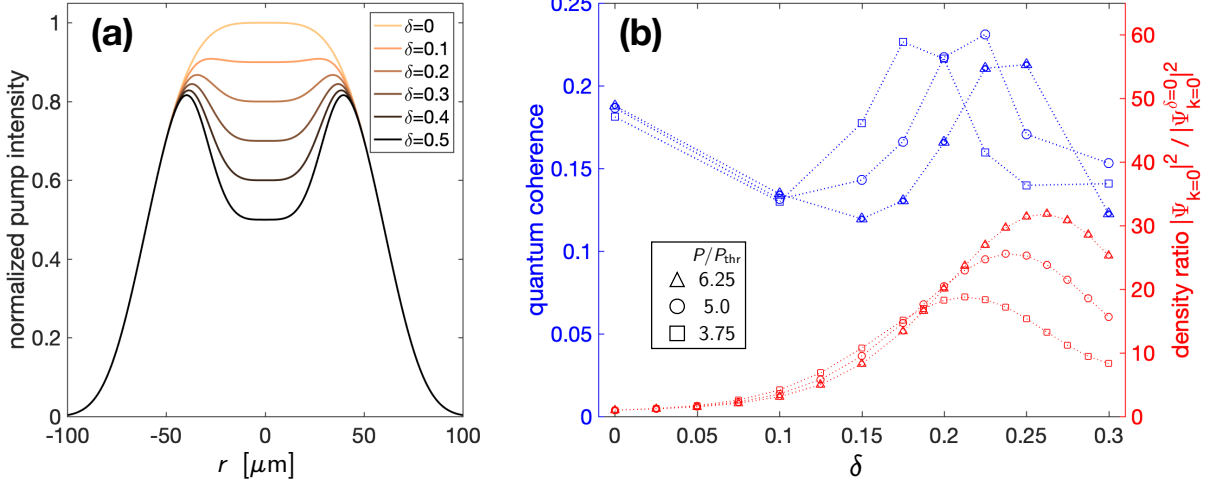
**Figure 5.6.** (a) Radial dependence of the pump profiles for different values of the reduction parameter $\delta$. (b) Left axis: Quantum coherence as a function of the reduction parameter $\delta$ for different pump intensities above threshold. Errors range from 8% to 16% and the corresponding error bars are omitted here for better visibility. Right axis: Single-mode density $|\psi_{k=0}(\delta)|^2$ as a function of the reduction parameter $\delta$ normalized to the density with no reduction $|\psi_{k=0}(\delta=0)|^2$ for the same pump intensities calculated with a corresponding mean-field model. Lines are shown to the eye.

increases again, indicating that the separation of condensate and reservoir maxima as well as the mode focusing become significant. As $\delta$ further increases, the coherence surpasses its initial value at $\delta = 0$ and forms a maximum close to the maximum of the corresponding density ratio. This behavior is similar for all three increasing pump intensities but each is shifted to larger $\delta$ values. Hence, the initial degeneracy of the saturation value is lifted. The maximum enhancement of the initially saturated quantum coherence is about 25%, confirming the general idea of spatially separating condensate and reservoir, but it comes with the cost of adjusting the pump intensity $P_0$ for each different $\delta$ in order to reach maximum quantum coherence. Additionally, in experiments the increase and the narrowing of the $k = 0$ mode emission might be limited by sample disorder. In conclusion, the main idea to increase the quantum coherence by using a ring-shaped pump profile to confine the condensate inside works but might be hard to realize in this specific setup. In the next Section 5.2, we investigate narrow ring-shaped pump profiles which additionally offer the excitation of stable orbital angular momentum modes.

# 5.2. Quantum coherence under spatially narrow and ring-shaped excitation

In this section we study spatially narrow excitation profiles. Starting from the previous results for spatially broad excitation, we first investigate the transition from broad to narrow pump profiles by varying the excitation spot size $w$. All physical system parameters defined in Sec. 5.1 are also utilized here for a better comparison.
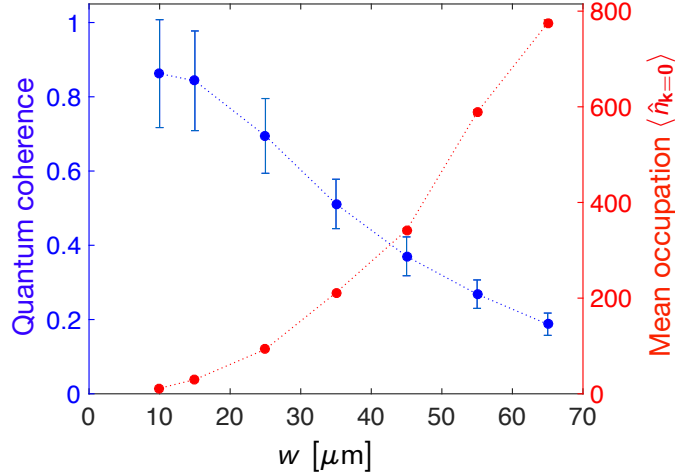


**Figure 5.7.** Quantum coherence (left axis) and mean occupation (right axis) of the zero-momentum mode as a function of the pump spot radius. Same system parameters as defined in the previous section. Sample size for each data point is $N_s = 100$.

Figure 5.7 shows the quantum coherence and mean occupation of the condensate zero-momentum mode while varying the excitation spot size $w$. While the corresponding quantum coherence increases significantly from $\mathscr{C} \approx 0.19$ to about $\mathscr{C} \approx 0.86$, its mean occupation decreases by almost two orders of magnitude. The decreasing density effectively reduces the nonlinear interactions similar to reducing the parameter $g_c$ in Sec. 5.1.1. Hence, scattering in and out of the zero-momentum mode induced by the fluctuations becomes more and more suppressed, resulting in an increasing quantum coherence. Besides other figures of merit, both a high quantum coherence and a high emission intensity are usually desired for any application in the direction of quantum information technologies. Both are heavily influenced by the spatial profile of the excitation as the results presented in Fig. 5.7 and Sec. 5.1.3 already suggest. Therefore, it is advantageous to explore this nontrivial competition behavior between quantum coherence and mean occupation depending on the pump's shape. In the limit of narrow excitation, the $k$-space spectrum of the condensate formation changes drastically. A review of polariton condensation under differently sized pumps spots can be found in Ref. [26]. A small Gaussian pump spot favors condensation into ring of momentum states, instead of the zero-momentum mode, if the polariton
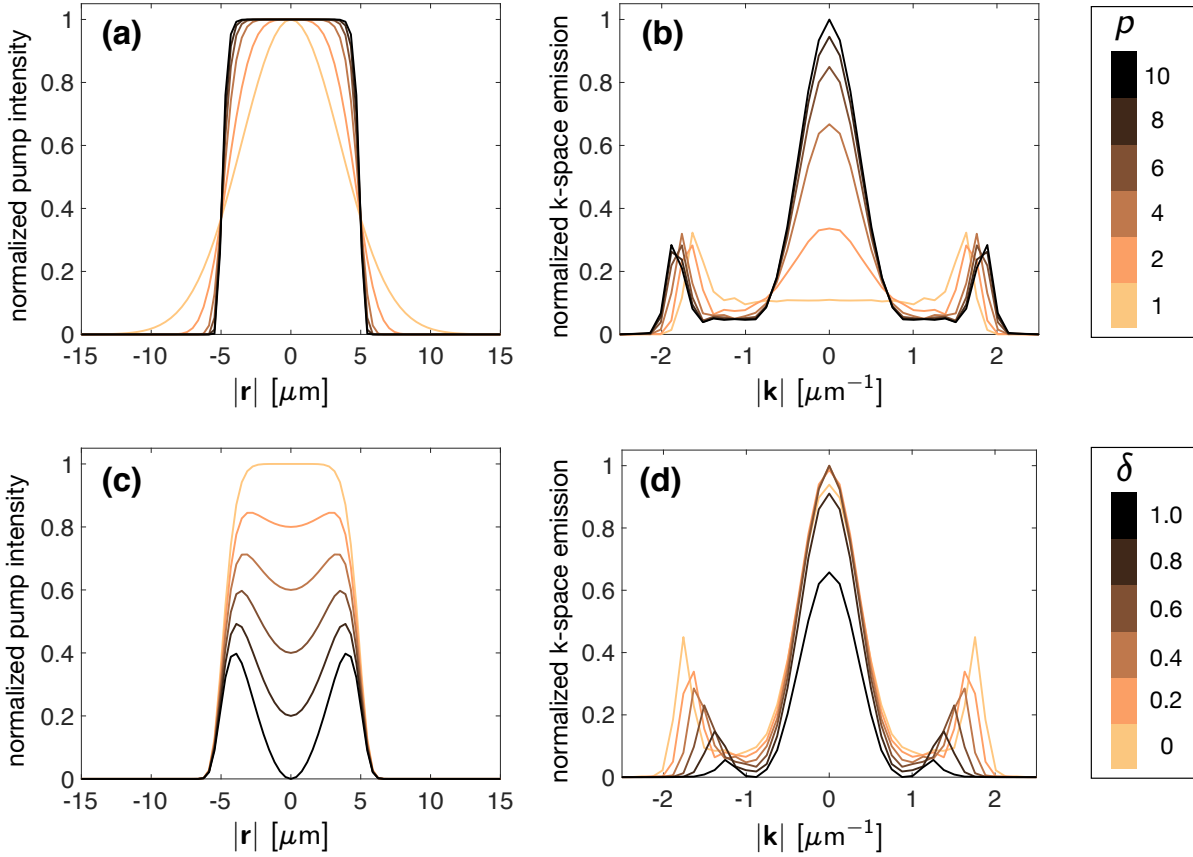
**Figure 5.8.** Effects of pump shaping on the $k$-space emission. Numerical results obtained from the mean-field versions of Eqs. (2.45) and (2.47). Radius and pump intensity are fixed at $w = 5$ $\mu$m and $P_0 = 70$ ps$^{-1}\mu$m$^{-2}$. Panels (a) and (c) show the one-dimensional cuts of pump profiles for different values of $p$ and $\delta$. Panels (b) and (d) show the corresponding normalized $k$-space emission. In (a,b) $\delta = 0$ and in (b,c) $p = 4$ are fixed.

propagation length exceeds the pump spot size [57, 162]. This ring-shaped condensate emission can be suppressed, while enhancing the zero-momentum mode, by reshaping the narrow Gaussian pump profile into a ring-shaped or super-Gaussian profile.

To systematically study the effects of pump shaping in the spatially narrow excitation regime, we define the following pump profile

$$P(\mathbf{r}) = P_0 \left( 1 - \delta e^{-\mathbf{r}^2/w^2} \right) e^{-(\mathbf{r}^2/w^2)^p} \tag{5.16}$$

where $\delta \in [0, 1]$ determines how ring-like the profile is, whereas $p$ determines how flat the top is. Numerical discretization parameters are adjusted to $L = 50$ $\mu$m, $N = 128$, $\Delta t = 0.02$ ps in this section to sufficiently resolve smaller spatial variations. Additionally, a super-Gaussian filter in $k$-space is used with a cut-off value of $k_{\text{cut}} = 10$ $\mu$m$^{-1}$ to avoid the problem of aliasing [64] and to maintain numerical convergence. Figure 5.8 shows the normalized $k$-space spectra alongside with the corresponding pump profiles for different

values of $\delta$ and $p$ to demonstrate the effects of pump shaping. These numerical results are obtained from the mean-field versions of Eqs. (2.45) and (2.47). The radius and the pump intensity are fixed to $w = 5$ $\mu$m and $P_0 = 70$ ps$^{-1}\mu$m$^{-2}$. Figures 5.8(a,c) show the one-dimensional cut of the pump profiles while varying $p$ and $\delta$, respectively. Increasing $p$, hence flatten the profile, enhances the emission of the zero-momentum mode significantly while keeping the ring-shaped emission at $k \approx 1.9$ $\mu$m$^{-1}$ almost unchanged; see Fig. 5.8(b). With increasing $\delta$, the pump becomes more ring-shaped and the induced potential acts as a trap. The outward flow of the condensate becomes increasingly suppressed so that the ring-shaped emission in $k$-space has smaller radii and vanishing densities; see Fig. 5.8(d). The density of the $k = 0$ mode first increases up until $\delta \approx 0.3$ and then decreases to about 30% of the starting value for $\delta = 1.0$.

Figure 5.9 shows the numerical results obtained from the stochastic model within the truncated Wigner framework. Again, we focus on the zero-momentum ground state for the different excitation geometries for a possible future comparison with experimental results which select the zero-momentum ground-state signal via local oscillator filtering; see also Sec. 5.1.2. Figure 5.9(a) shows that a more flat-top Gaussian pump profile, in addition to an increasing occupation of the zero-momentum mode, maintains an almost constant and high quantum coherence of about $\mathscr{C} \approx 0.9$. The effect of increasing $\delta$, making the pump profile more ring-shaped, is rather weak, as shown in Fig. 5.9. Merely a small drop-off due to the decreasing total density is visible. Regarding the enhancement of quantum coherence by spatially separating condensate and reservoir via pump shaping introduced in Sec. 5.1.3, in the narrow excitation regime, we find a similar maximum growth ($+0.05$ for $\delta = 0.8$) of the quantum coherence in terms of absolute values while increasing $\delta$. Of course, the relative change is quite low $\sim 2\%$ due to the high base value compared to 25% found for the spatially broad excitation; see Sec. 5.1.3. Within the range of error bars, the quantum coherence is approximately at a constant level of about $\mathscr{C} \approx 0.9$ for all values of $\delta \in [0, 1]$. In conclusion, pump shaping in the spatially narrow excitation regime shows the following trends: (i) Decreasing the pump radius $w$ leads to increasing $\mathscr{C}$, but decreasing $\langle \hat{n}_{k=0} \rangle$, (ii) increasing the flat-top parameter $p$ leads to increasing $\mathscr{C}$, but decreasing $\langle \hat{n}_{k=0} \rangle$, and (iii) increasing the ring-shape parameter $\delta$ leads to increasing $\mathscr{C}$ and increasing $\langle \hat{n}_{k=0} \rangle$.

## 5.2.1. Quantum coherence of vortices

So far in this chapter, we studied the statistics of the polariton condensate mode at zero momentum, corresponding to a homogeneous mode in real space. Now, we want to extend the investigation to vortex modes with nonzero orbital angular momentum, which can be stabilized in narrow ring-shaped pump profiles as it was introduced in Chapter 4.
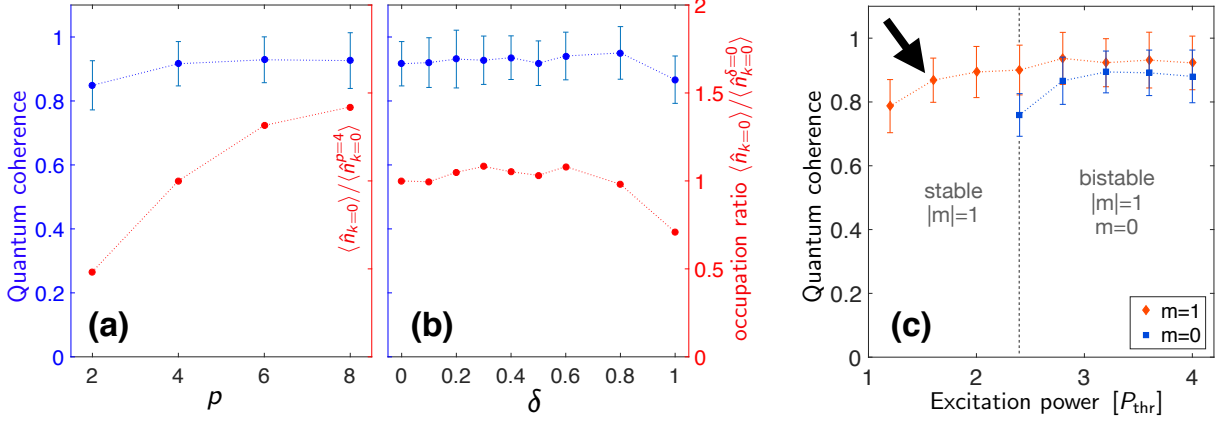
**Figure 5.9.** Quantum coherence (left axis) and normalized occupation number (right axis) as a function of pump shape parameters (a) $p$ with fixed $\delta = 0$ and (b) $\delta$ with fixed $p = 4$. Additional parameters are $w = 5$ $\mu$m and $P_0 = 70$ ps$^{-1}\mu$m$^{-2}$. Corresponding pump profiles and $k$-space emissions are shown in Fig. 5.8. Panel (c) shows the quantum coherence of the vortex mode with $m = 1$ and the fundamental mode with $m = 0$ as a function of the excitation power. Parameters are $w = 5$ $\mu$m, $p = 4$, and $\delta = 1.0$. Sample size for each data point is $N_s = 300$. Black arrow marks the state for which an explicit density matrix reconstruction is performed in Sec. 5.3.

Analogously to the expansion of the bosonic field operator in terms of linear momentum modes in Eq. (5.3) for systems with translation symmetry, the operator can be expanded in terms of orbital angular momentum modes for systems with circular symmetry,

$$\hat{\psi}(\mathbf{r}) = \frac{1}{\sqrt{V}} \sum_{m \in \mathbb{Z}} e^{im\phi} \hat{b}_m, \tag{5.17}$$

$$\hat{b}_m = \frac{\Delta V}{\sqrt{V}} \sum_{\mathbf{r}} e^{-im\phi} \hat{\psi}(\mathbf{r}), \tag{5.18}$$

where $\phi$ is the polar angle of the two-dimensional coordinates $\mathbf{r} \equiv (r, \phi)$. Again, we are interested in the coherence properties, but this time of the orbital angular momentum modes in addition. Experimentally, these investigations can be realized with the homodyne detection scheme where the local oscillator itself will be in a vortex state to filter out a specific orbital angular momentum mode.

Figure 5.9(c) shows the quantum coherence for both the fundamental mode $m = 0$ and the vortex mode $m = -1$ as a function of the excitation power for $w = 5$ $\mu$m, $p = 2$, and $\delta = 1.0$. Note that $P_{\text{thr}} = 25$ ps$^{-1}\mu$m$^{-2}$ refers to the numerically determined condensation threshold value for the specific excitation condition. The initial states are prepared as coherent states with a predefined topological charge. They are evolved in time until the final stationary displaced thermal states are reached. Numerical results for all observables are then obtained as steady-state averages. For $P_0 < 2.4\ P_{\text{thr}}$, only the vortex mode $m = -1$ is stable and its quantum coherence saturates at a value of $\mathscr{C} \approx 0.9$; see orange diamonds

in Fig. 5.9(c). Additionally, for $P_0 > 2.4\,P_{\text{thr}}$, the fundamental mode $m = 0$ also becomes stable and saturates at a similar value; see blue squares in Fig. 5.9(c). Vortex states might be an interesting platform to further investigate quantum coherence and correlations of single orbital angular momentum modes, and importantly also between them, especially due to their properties already discussed in Chapter 4, e.g. their additional degree of freedom, their robustness in the presence of noise and disorder, and their on-demand manipulation possibilities.

## 5.3. Quantum state reconstruction via pattern functions

Thus far, we studied the different coherence properties of polariton condensates. While $g^{(2)}$ relates to the diagonal elements of the density operator in Fock space, namely the occupation probability distribution, the quantum coherence $\mathscr{C}$ quantifies the amount of off-diagonal elements. In this section, we reconstruct the density operator in Fock space explicitly with the help of the so-called pattern functions [163–166]. For a review see also Refs. [167, 168]. The main idea is to reconstruct the density matrix of a quantum state by sampling the phase space spanned by the phase-space variables $\alpha$, which corresponds to an arbitrary single-mode ladder operator $\hat{a}$ in the following.

For our specific case of numerically sampling the Wigner function, we briefly review a derivation of the corresponding pattern functions [169]. The key point is the existence of mappings between the density matrix and the Wigner function, allowing reconstruction of each other from each other, explicitly [170]

$$\hat{\rho} = \int d^2\alpha\, W(\alpha) 2\hat{\Pi}(\alpha), \tag{5.19}$$

$$W(\alpha) = \text{tr}\left[\hat{\rho} 2\hat{\Pi}\right], \tag{5.20}$$

with the displaced parity operator $\hat{\Pi}(\alpha) = \hat{D}(\alpha)\hat{\mathcal{P}}\hat{D}^\dagger(\alpha) = (-1)^{\hat{n}(\alpha)}$ consisting of the displacement operator $\hat{D}(\alpha) = \exp(\alpha\hat{a}^\dagger - \alpha^*\hat{a})$ and the parity operator $\hat{\mathcal{P}} = \sum_{n=0}^{\infty}(-1)^n|n\rangle\langle n|$ $= \exp(i\pi\hat{n}) = (-1)^{\hat{n}}$. Equation (5.19) can be understood as an expansion of the density matrix in terms of displaced parity operators with Wigner functions as weights. Defining an observable $\hat{L} = |m\rangle\langle n|$ leads to the elements of the density matrix via the expectation value

$$\langle\hat{L}\rangle = \text{tr}\left[\hat{\rho}\hat{L}\right] = \sum_k \langle k|\hat{\rho}|m\rangle\langle n|k\rangle = \langle n|\hat{\rho}|m\rangle. \tag{5.21}$$

Using Eq. (5.19) and the definition of $\hat{\Pi}(\alpha)$, we obtain

$$\langle n|\hat{\rho}|m\rangle = \int d^2\alpha\, W(\alpha) 2\langle n|\hat{\Pi}(\alpha)|m\rangle = \int d^2\alpha\, W(\alpha) 2\langle n|(-1)^{\hat{n}(\alpha)}|m\rangle, \qquad (5.22)$$

where we define the pattern functions

$$f_{n,m}(\alpha) \equiv 2\langle n|(-1)^{\hat{n}(\alpha)}|m\rangle. \qquad (5.23)$$

The density matrix elements (expectation values of the observable $\hat{L}$) can now be calculated by sampling the Wigner function

$$\langle n|\hat{\rho}|m\rangle \approx \frac{1}{N_s}\sum_{i=1}^{N_s} f_{n,m}(\alpha_i). \qquad (5.24)$$

For the specific physical system of polariton condensates, the $N_s$ samples $\alpha_i$ are obtained via numerical simulation within the truncated Wigner approximation, as described in Sec. 2.3. Then, $\alpha$ can refer to any single mode in real or momentum space. Experimentally, the quantum state reconstruction can be realized via balanced homodyne detection which captures the quadratures of a signal light field mode. The measured quadrature histogram can then be used to sample the density matrix analogously to the prescription described above since $\alpha$ is just a composition of the quadratures.

For the explicit evaluation of the pattern functions [169], we use the following representation of number states

$$|m\rangle = \frac{(\hat{a}^\dagger)^m}{\sqrt{m!}}|0\rangle = \frac{1}{\sqrt{m!}}\partial_\gamma^m e^{\gamma\hat{a}^\dagger}|0\rangle\bigg|_{\gamma=0} = \frac{1}{\sqrt{m!}}\partial_\gamma^m e^{|\gamma|^2/2}\hat{D}(\gamma)|0\rangle\bigg|_{\gamma=0} = \frac{1}{\sqrt{m!}}\partial_\gamma^m e^{|\gamma|^2/2}|\gamma\rangle\bigg|_{\gamma=0}, \qquad (5.25)$$

and analogously

$$\langle n| = \frac{1}{\sqrt{n!}}\partial_{\beta^*}^n e^{|\beta|^2/2}\langle\beta|\bigg|_{\beta^*=0}, \qquad (5.26)$$

where we have used the displacement operator in the representation $\hat{D}(\gamma) = e^{-|\gamma|^2/2}e^{\gamma\hat{a}^\dagger}e^{\gamma^*\hat{a}}$ with its action $\hat{D}(\gamma)|0\rangle = |\gamma\rangle$. The parity operator in normal order is given by [171]

$$(-1)^{\hat{n}} =: e^{-2\hat{n}} :, \qquad (5.27)$$

which allows us to rewrite the displaced parity operator into

$$(-1)^{\hat{n}(\alpha)} = \hat{D}(\alpha)(-1)^{\hat{n}}\hat{D}^\dagger(\alpha) = \hat{D}(\alpha) : e^{-2\hat{n}} : \hat{D}^\dagger(\alpha) =: e^{-2(\hat{a}^\dagger-\alpha^*)(\hat{a}-\alpha)} : . \qquad (5.28)$$

Substituting all these expressions back into Eq. (5.23) leads to an expression to explicitly

calculate the pattern functions

$$f_{n,m}(\alpha) = \frac{2e^{-2|\alpha|^2}}{\sqrt{n!m!}} \partial_\gamma^m \partial_{\beta^*}^n e^{|\beta|^2/2+|\gamma|^2/2} \langle\beta| : e^{-2(\hat{a}^\dagger-\alpha^*)(\hat{a}-\alpha)} : |\gamma\rangle \Big|_{\gamma=0=\beta^*} \tag{5.29}$$

$$= \frac{2e^{-2|\alpha|^2}}{\sqrt{n!m!}} \partial_\gamma^m \partial_{\beta^*}^n e^{|\beta|^2/2+|\gamma|^2/2} e^{-2(\beta^*-\alpha^*)(\gamma-\alpha)} e^{-|\beta|^2/2-|\gamma|^2/2+\beta^*\gamma} \Big|_{\gamma=0=\beta^*} \tag{5.30}$$

$$= \frac{2e^{-2|\alpha|^2}}{\sqrt{n!m!}} \partial_\gamma^m \partial_{\beta^*}^n e^{2\alpha\beta^*+2\alpha^*\gamma-\beta^*\gamma} \Big|_{\gamma=0=\beta^*} . \tag{5.31}$$

The first diagonal elements for $n = m = 0, ..., 5$ read

$$f_{0,0}(\alpha) = 2e^{-2|\alpha|^2},$$

$$f_{1,1}(\alpha) = 2e^{-2|\alpha|^2}(-1 + 4|\alpha|^2),$$

$$f_{2,2}(\alpha) = 2e^{-2|\alpha|^2}(1 - 8|\alpha|^2 + 8|\alpha|^4),$$

$$f_{3,3}(\alpha) = \frac{2}{3}e^{-2|\alpha|^2}(-3 + 36|\alpha|^2 - 72|\alpha|^4 + 32|\alpha|^6),$$

$$f_{4,4}(\alpha) = \frac{2}{3}e^{-2|\alpha|^2}(3 - 48|\alpha|^2 + 144|\alpha|^4 - 128|\alpha|^6 + 32|\alpha|^8),$$

$$f_{5,5}(\alpha) = \frac{2}{15}e^{-2|\alpha|^2}(-15 + 300|\alpha|^2 - 1200|\alpha|^4 + 1600|\alpha|^6 - 800|\alpha|^8 + 128|\alpha|^{10}).$$

These explicit examples demonstrate that the pattern functions for the diagonal elements include terms proportional to $(-1)^j|\alpha|^{2j}$ with $j = 0, ..., n$, making numerical convergence quite challenging due to the numerical problem of large number cancellation. Due to finite precision of floating-point numbers, differences of very similar numbers can have large errors. This source of error was already pointed out in earlier works regarding the pattern functions [164]. Therefore, using standard double precision is not sufficient and will cause problems already at occupation numbers $n \gtrsim 30$. To overcome this issue, we mainly use symbolic computation, which increases the numerical effort significantly but gives the correct results which are presented in the following.

## 5.3.1. Reconstruction of artificially generated coherent states

To demonstrate and test the reconstruction method via pattern functions we start with an example by sampling an artificially generated coherent state and then try to reconstruct it. First, we study the occupation number distribution given by the diagonal of the density
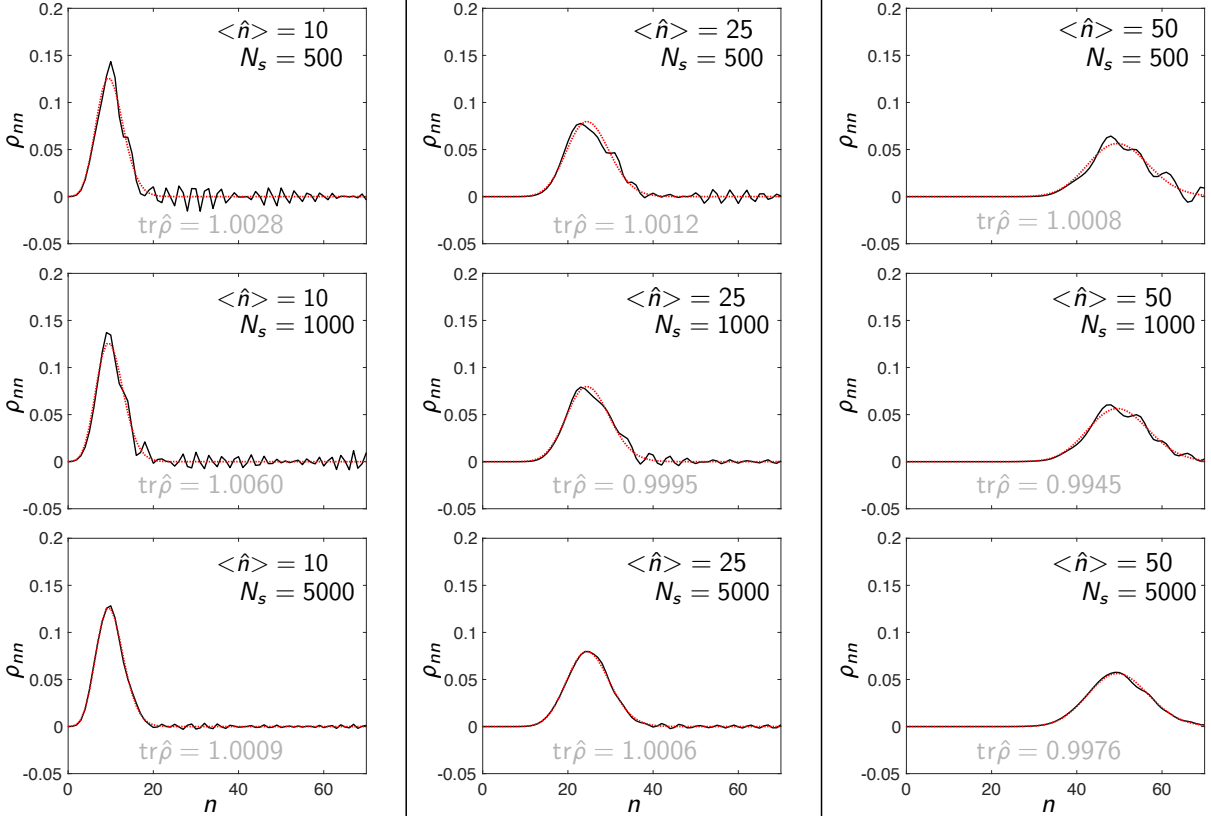
**Figure 5.10.** Results of reconstruction of the number distribution for different artificially created coherent states and for different sample sizes $N_s$. Dashed red lines show corresponding Poisson distributions First row: $\langle \hat{n} \rangle = 10$. Second row: $\langle \hat{n} \rangle = 25$. Third row: $\langle \hat{n} \rangle = 50$.

matrix. For a coherent state, the latter is given by

$$\hat{\rho} = |\alpha\rangle\langle\alpha| = e^{-|\alpha|^2} \sum_{n,m}^{\infty} \frac{\alpha^n \alpha^{*m}}{\sqrt{n!m!}} |n\rangle\langle m|, \qquad (5.32)$$

where the diagonal elements follow a Poisson distribution for the occupation number

$$P_n = \langle n|\hat{\rho}|n\rangle = |\langle n|\alpha\rangle|^2 = e^{-|\alpha|^2} \frac{|\alpha|^{2n}}{n!}. \qquad (5.33)$$

Figure 5.10 shows the results of the number distribution reconstruction via pattern functions for different coherent occupations $\langle \hat{n} \rangle = |\alpha|^2$ and for different sample sizes $N_s$. The Wigner function of a coherent state is a Gaussian in quadrature phase space. Therefore, the samples $\alpha_i$ can be artificially created by drawing random numbers for real and imaginary part of $\alpha$ from Gaussian distributions with variances $\langle(\Delta\Re(\alpha))^2\rangle = \langle(\Delta\Im(\alpha))^2\rangle = 0.25$ centered at fixed positions according to $\langle\alpha\rangle = \langle|\alpha|e^{i\varphi}\rangle$. The dashed red lines in Fig. 5.10 show the corresponding Poisson distributions as a reference. In all cases, the left side tail of the distribution is better resolved than the right side tail. The sample size needed to
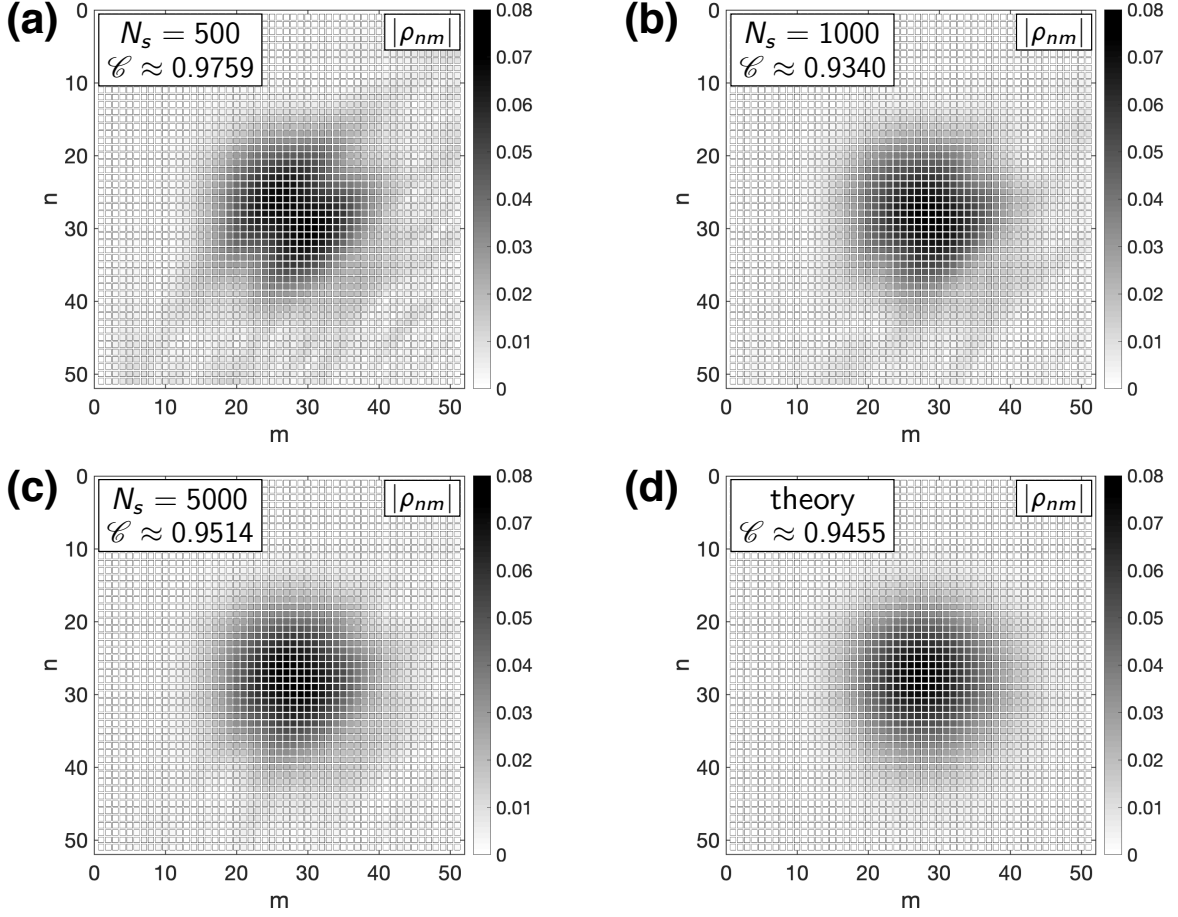
**Figure 5.11.** Results of density matrix reconstruction for an artificially created coherent state with different sample sizes (a) $N_s = 500$, (b) $N_s = 1000$, (c) $N_s = 5000$, alongside the theoretical density matrix (d).

achieve convergence for a given element $\rho_{nn}$ depends on the occupation number $n$ as well as the actual mean $\langle \hat{n} \rangle = |\alpha|^2$ of the data. Therefore, the reconstructed distributions converge asymmetrically, especially for low sample sizes. However, we find that the reconstructed data fits quite well to the theoretical curves. Maximum and width are reproduced correctly and $\text{tr}\,[\hat{\rho}] = 1$ is satisfied.

Now, we extend the implemented algorithm to the reconstruction of the off-diagonal elements of the density matrix in Fock space, which give information about the number state superpositions, i.e. the quantum coherence. Again, we use an artificially generated coherent state. Note, due to the slow symbolic calculations the size of the density matrix is effectively truncated. Compared to the reconstruction of the diagonal elements, the time effort is now squared; but it can be cut in half due to the hermiticity. Figure 5.11 shows the modulus of the reconstructed density matrix for different sample sizes for a coherent state with $\langle \hat{n} \rangle = |\alpha|^2 = 27$. Also shown in Figure 5.11(b) is the theoretical density matrix according to Eq. (5.32). The theoretical quantum coherence is $\mathscr{C}_{\text{theo}} \approx 0.9455$. The results show a good agreement of the reconstructed state with the theoretical state even for a low

sample size. As expected, the reconstructed data becomes even better for larger sample sizes. The resulting quantum coherence fits the theoretical value almost perfectly for $N_s = 5000$.

### 5.3.2. Reconstruction of displaced thermal states

The next step is to apply the reconstruction method to data of the simulated polariton system presented in Sec. 5.1. Above the condensation threshold the polariton condensate can be approximated by a displaced thermal state, which describes the intermediate regime between thermal and coherent states. In this case, the distribution of the occupation number in terms of the thermal $\bar{n}$ and coherent $|\alpha_0|^2$ contributions is given by [172]

$$P_n = \frac{\bar{n}^n}{(1+\bar{n})^{n+1}} \exp\left(-\frac{|\alpha_0|^2}{1+\bar{n}}\right) L_n\left(-\frac{|\alpha_0|^2}{\bar{n}+\bar{n}^2}\right), \tag{5.34}$$

where $L_n$ are the Laguerre polynomials of $n$-th order. From the simulated mean $\langle\hat{n}\rangle$ and variance $\langle(\Delta\hat{n})^2\rangle$ for the polariton-number occupation for a specific mode, we can extract the different contributions via the relations in Eqs. (5.10a) and (5.10b). Here, we use the existing data from simulations of our joint work [43], presented in Sec. 5.1 above. Figure 5.12 shows the occupation-number distribution for the zero-momentum mode of
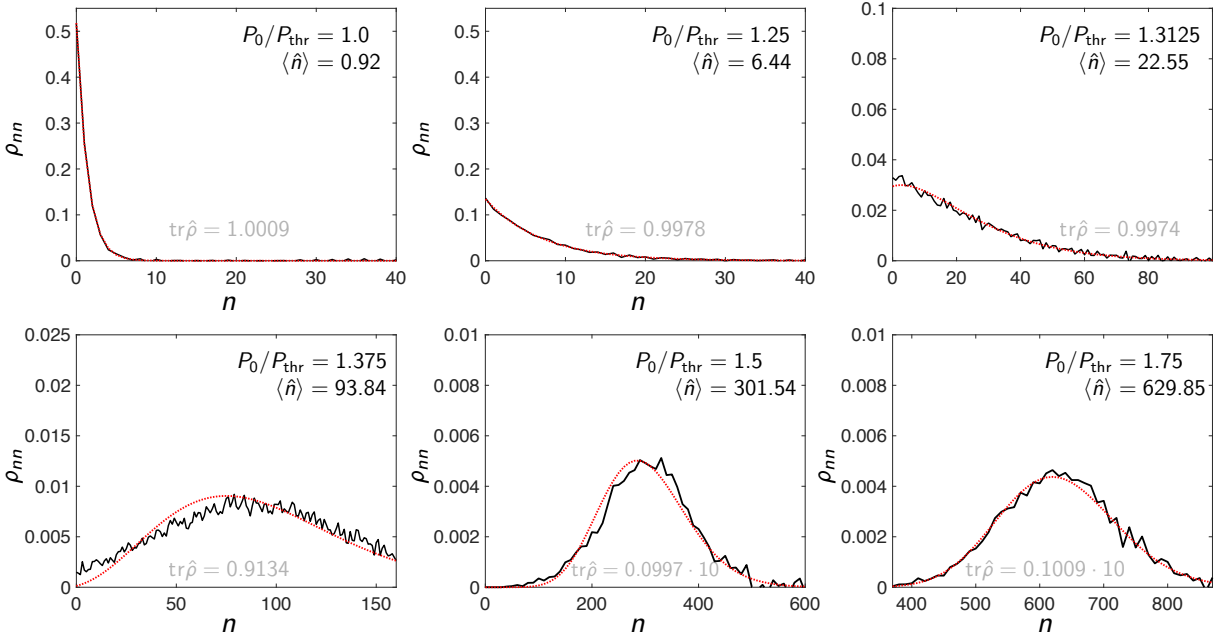


**Figure 5.12.** Results of reconstruction of the occupation-number distribution for the simulated polariton condensates for different pump intensities. Dashed red lines show corresponding theoretical distributions for a displaced thermal state according to Eq. (5.34). Samples sizes are $N_s = 30000$ for $P = P_{\mathrm{thr}}$ and $N_s = 20000$ otherwise.

the polariton condensate for different pump intensities. Note that for $P_0/P_{\text{thr}} = 1.5$ and $P_0/P_{\text{thr}} = 1.75$ only every tenth diagonal matrix element was calculated to reduce the numerical run time. The number of simulated realization is $N = 300$ for $P = P_{\text{thr}}$ and $N = 200$ otherwise. Additionally, for each realization, we take 100 different time snapshots in an interval of 2 ns where the steady state was reached, resulting in effective sample sizes of $N_s = 30000$ and $N_s = 20000$, respectively. We observe that distributions are well resolved and reproduce the theory. Especially for low occupation numbers, the reconstructed data fits very well. The condition of $\text{tr}\,[\hat{\rho}] = 1$ is also satisfied with small deviations because of the truncation. Some minor deviations and convergence issues occur in the intermediate regime ($P \geq 1.375 P_{\text{thr}}$) where the transition from a mostly thermal state to a mostly coherent state takes place. Importantly, the numerical results also fit qualitatively to the recently measured photon-number distributions of a polariton condensate across the threshold using a photon-number-resolving transition edge sensor [154]. The reconstructed data can be improved by using more realizations and more time snapshots to increase the effective sample size. Note that calculations for higher occupation numbers $n > 10^2$ become exceedingly slow because of the number of symbolic computations involved. Therefore, a major goal for the future should be the improvement of the calculation process regarding the computation time. In return, an improved method will enable us to resolve distributions with higher occupation numbers and to use larger sample sizes.

### 5.3.3. Off-diagonal elements and temporal decay of quantum coherence

So far, we have discussed the diagonal elements of the reconstructed density matrices for the numerical simulated condensate states, which corresponds to the occupation-number distribution. In order to study quantum coherence, we have to include the off-diagonal elements, which correspond to superpositions of particle-number states. In Section 5.1 we demonstrated how to quantify quantum coherence of displaced thermal states by their coherent and thermal contributions. These results can be extended by explicitly reconstructing the off-diagonal elements using the pattern functions given in Eq. (5.23). In this context, the phase plays an important role in contrast to the reconstruction of the diagonal elements. Therefore, we have to be careful how the phase-space data and which phase-space data is obtained in both experiment and simulation. In the numerical simulations, the phase-space variable of a single mode for a single realization sample is given by

$$\alpha(t) = |\alpha(t)|e^{-i(\omega t - \varphi)}, \tag{5.35}$$

where $\omega$ is the frequency of the particular mode sample and $\varphi$ is an arbitrary phase determined by the initial condition and fluctuations. The mean condensate frequency is determined by the fixed system parameters. The individual frequencies vary within the sample ensemble and over time due to polariton-number fluctuations constituting an intrinsic decoherence mechanism [151]. The commonly studied property to determine the phase coherence is the first-order unequal-time correlation function $g^1(\tau) = \langle \hat{a}^\dagger(t)\hat{a}(t+\tau) \rangle$. Within our truncated Wigner framework, $g^{(1)}(\tau)$ cannot be directly calculated due to unknown unequal-time commutators [173]. However, since we are directly sampling the Wigner function, it is possible to dynamically track the circular variances of the phase distribution as a measure of coherence. Alternatively, temporal decay of phase coherence is reflected in the decrease of off-diagonal density matrix elements which can be tracked by explicit numerical reconstruction.

In the following, we study the temporal decay of quantum coherence via explicit density matrix reconstruction at different points in time. Key point of this investigation is a proper state preparation. Assuming an empty cavity as initial condition leads to randomized phases for all samples, resulting in $\langle \alpha(t) \rangle = 0$ at all times. Therefore, using phase-randomized data, as the initial vacuum assumption suggests, leads to vanishing off-diagonal elements, and hence $\mathscr{C} = 0$. A possibility to resolve this problem is to start with a displaced thermal state, i.e. a Gaussian distribution in phase space, with mean occupation number and quantum coherence that match the steady-state values. This method fixes the mean and circular variance of the phase angle of the initial state which then is evolved in time. In that way, the fluctuations in amplitude and phase are determined by the dynamical noise and not influenced by randomization of the initial conditions.

The state preparation and density matrix reconstruction is demonstrated for a vortex state as an example in the following. We choose the state marked with a black arrow in Fig. 5.9 in Sec. 5.2.1 because it has a low mean occupation number which justifies an early truncation in Fock space to improve numerical accuracy. Excitation parameters are $P_0 = 40 \text{ ps}^{-1}\mu\text{m}^{-2} = 1.6 \ P_{\text{thr}}$, $w = 5 \ \mu\text{m}$, $\delta = 1.0$, and $p = 4$. The single vortex mode with topological charge $l = 1$ has the steady-state averaged expectation values $\langle \hat{n}_{l=1} \rangle = 27.5$ and $\langle (\Delta \hat{n}_{l=1})^2 \rangle = 29.9$, leading to a quantum coherence value of about $\mathscr{C} = 0.87$. These three values are the targets of the following optimization algorithm. First, the steady state's spatial envelope is determined via the corresponding mean-field model. Secondly, $N_s = 2000$ phase-space samples are drawn from a Gaussian distribution with mean $\mu$ and standard deviation $\sigma$ for each spatial grid point. Afterwards, this sampled grid is multiplied with the normalized spatial envelop of the vortex state including the $2\pi$ phase winding. Thirdly, the expectation values $\langle \hat{n}_{l=1} \rangle$, $\langle (\Delta \hat{n}_{l=1})^2 \rangle$, and $\mathscr{C}$ of the single vortex mode $l = 1$ are calculated and compared with the target values. Based on the
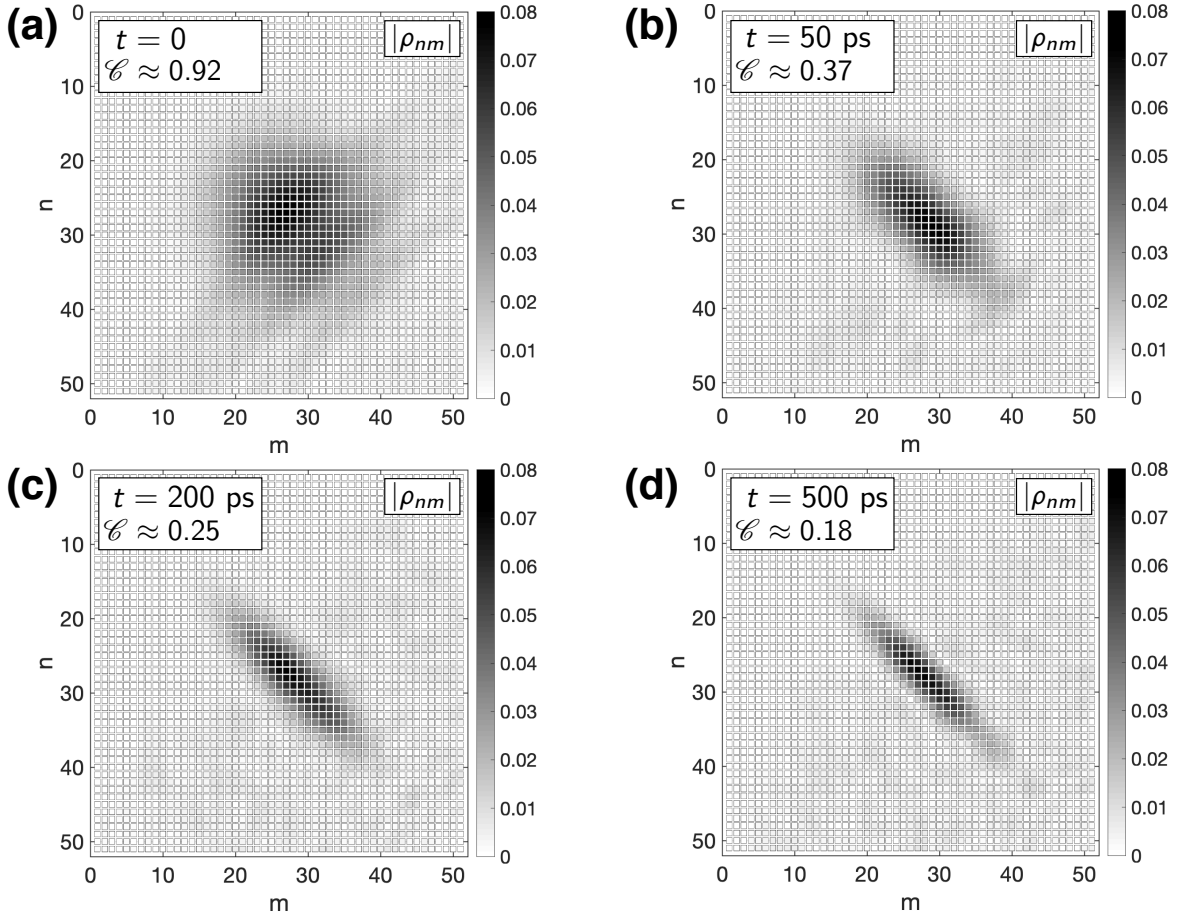
**Figure 5.13.** Results of the density matrix reconstruction for a numerically simulated vortex state $l = 1$ at different points in time: (a) $t = 0$, (b) $t = 50$ ps, (c) $t = 200$ ps, and (d) $t = 500$ ps. This state is marked with a black arrow in Fig. 5.9 in Sec. 5.2.1. Excitation parameters are $P_0 = 40$ ps$^{-1}\mu$m$^{-2}$, $w = 5$ $\mu$m, $\delta = 1.0$, $p = 4$, and sample size is $N_s = 2000$.

deviations, the procedure is repeated with different values for $\mu$ and $\sigma$ until a sufficient agreement with all three target values is reached; for the selected vortex state, we find $\mu = 3.92$ and $\sigma = 8.66$. The initial reservoir state is taken from the stationary mean-field solution. Finally, the state preparation yields an initial condition with the same expectation values as the corresponding steady state but with the right amount of phase coherence instead of completely random phases. The initial state is then dynamically evolved via Eqs. (2.45, 2.47) and its density matrix in Fock space is reconstructed at different points in time. The corresponding quantum coherence can then be calculated by direct summation of the squared absolute values of the off-diagonal elements; see Eq. (5.11).

Figure 5.13 shows the absolute values of the reconstructed density matrix elements in truncated Fock space with $n, m \in [0\ 51]$ at four different points in time. The initial state at $t = 0$ shows a broad, approximately circular spot centered at $n, m = 27 \approx \langle \hat{n}_{l=1} \rangle$, indicating a large amount of off-diagonal contributions. The corresponding quantum coherence of about $\mathscr{C} \approx 0.92$ fits the steady-state value. Additionally, numerical artifacts

in form of weak diagonal stripes are visible which can be further avoided by increasing the sample size; see also previous Sec. 5.3.1. Figure 5.13(b) shows $|\rho_{nm}|$ at $t = 50$ ps. The initially broad spot is now more contracted towards the diagonal, marking the decrease of off-diagonal elements. Consequently, the quantum coherence is reduced to $\mathscr{C} \approx 0.37$ while the diagonal elements remain approximately constant. This trend continues at later points in time as shown, e.g. (c) $\mathscr{C} \approx 0.25$ at $t = 200$ ps and (d) $\mathscr{C} \approx 0.18$ at $t = 500$ ps. In conclusion, the procedure presented in this section allows us to track coherence properties in the time domain and is planned to be used in our theory-experiment cooperation.

# 6. Conclusion and outlook

In this thesis we theoretically investigated different functional aspects of polaritons in semiconductor microcavities. As a prototypical hybrid light-matter system, polaritons have become an important platform to study nonlinear optical phenomena because of their relevance in the context of optoelectronic devices. We explored three promising directions based on representative configurations, which are recapitulated further below.

In Chapter 3 we reviewed a recently proposed all-optical switching scheme of orthogonal two-spot patters in a resonantly excited spinor polariton fluid. The spatial pattern formation originates from phase-matched wave-mixing processes of polariton fields inherited from exciton-exciton scattering within the underlying matter system. The reversible on-demand switching process is based on the polariton's peculiar polarization dependence, which induces spatial anisotropy. We reproduced a switching example by numerical simulations using a spatially extended semiclassical model for the light-matter interaction. Starting from this full model, we recapitulated the derivation of a simplified population competition model for the occupations of the two relevant two-spot patterns. We showed that this model takes the form of an inhomogeneous generalized Lotka-Volterra model for two competing species. We performed a complete steady-state analysis of the population competition model, calculated the phase boundaries in parameter space spanned by the external control and anisotropy parameters, and characterized all corresponding bifurcations. Importantly, the model parameters can be directly calculated from the physical quantities used in the simulations. In conclusion, we found that the population competition model covers all key features of the orthogonal switching process observed in the numerical simulations based on the full model. Furthermore, our results confirm and explain the general performance trends found in previous numerical studies of the specific switching process. Due to the broad spread of generalized Lotka-Volterra models throughout various fields of science, the results presented here are relevant and can be similarly applied in different contexts in the future. From a more general point of view, we demonstrated how powerful a simplified model, based on a few reasonable assumptions, can be in order to shed light onto the rather complex dynamics of the light-matter system at hand.

In Chapter 4 we investigated localized vortices under ring-shaped linearly polarized excitation in a nonresonantly excited spinor polariton condensate. To this end, we

performed numerical simulations of a driven-dissipative two-component Gross-Pitaevskii model phenomenologically extended by the incoherent reservoir dynamics. We found a rich multistability of different localized full-, spin-, and half-vortex states. The last are characterized by a circular polarization peak in the vortex core region, which allows detection of half-vortex states by simply measuring the polarization resolved intensities instead of the rather complicated phase information. Moreover, we demonstrate the known density reshaping effect due to the TE-TM splitting, and categorized different vortex states based on their reduced spatial symmetries. Importantly, we proposed a half-vortex switching scheme triggered by a resonant control pulse which results in the reversal of the circular polarization peak in the vortex core region. The switching process is based on the attractive cross-interaction between oppositely polarized polaritons. Besides studying specific examples, we determined the minimum time-integrated pulse-induced density required to trigger the switching as a function of the cross- and self-interaction strength ratio. From a more general point of view, we demonstrated that the polarization degree of freedom in polariton condensates is important regarding localized vortex states and can be effectively utilized. A straightforward continuation is to perform further performance studies to reveal possible non-trivial effects of the system parameters, as well as the exploration of more sophisticated multi-step switching configurations involving higher-order orbital angular momentum modes. From an experimental point of view, it would be a great first step to observe the multistability of half-, full-, and spin-vortex states under linearly polarized ring-shaped excitation. With a view to the last Chapter 5, a promising direction is to investigate the vortex multistability regarding their coherence and correlation properties with the help of the presented phase-space method. Especially, the vortex formation process in the multistability regime could yield valuable insights of the initial mode competition.

In Chapter 5, as part of a theory-experiment joint work, we established a new access to polariton condensates which determines their general resourcefulness in terms of quantum-information tasks. To this end, we used a phase-space model derived from the density matrix formalism of the quantized polariton field, which incorporates fluctuations and allows to calculate expectation values. We showed that polariton condensates under spatially broad nonresonant excitation exhibit a significant amount of quantum coherence of about $\mathscr{C} \approx 0.2$. The quantum coherence quantifies the magnitude of off-diagonal contributions to the density matrix in Fock space, and hence indicates particle-number superposition within the polariton condensate. The numerically determined quantum coherence fits well with the experimental value. Furthermore, we explored a method to enhance the quantum coherence via pump shaping, i.e. by spatially separating the condensate and the reservoir to reduce fluctuations. We investigated the transition between spatially broad to narrow excitation and found a significant increase of the quantum coherence accompanied

by a notable decrease of the mean occupation number. We showed that under a narrow ring-shaped excitation bistable vortex and non-vortex states exhibit a similar amount of quantum coherence. Lastly, we explicitly reconstructed the density matrix in Fock space for exemplary polariton condensate states. On the one hand, the diagonal elements revealed a polariton-number distribution, which fits very well to the theory of a displaced thermal state and to recent photon-number resolved experiments. On the other hand, the off-diagonal elements allowed us to explicitly calculate the quantum coherence, and additionally to track the decay of coherence in time. In general, this fruitful cooperation opens the door to further perform quantum process tomography with polariton condensates in various configurations. Besides the improvement of the numerical implementation to handle more data, a next step is to include the polarization dependence and finite sample disorder potentials within the phase-space model. As discussed in Chapter 4, with the additional degrees of freedom, namely the topological charge and the polarization, a rich controllable multistability of different vortex states arises under linearly polarized ring-shaped excitation. This is a great opportunity to study coherence and correlation properties of various vortex states within our theory-experiment cooperation. Additionally, it will be interesting to investigate formation dynamics in ring-shaped pump profiles to reveal the competition and correlation between different orbital angular momentum modes in time. For this purpose, elements of a reduced density matrix in a truncated orbital angular momentum basis can be calculated.

# A. Numerical implementation

All numerical simulations throughout the thesis are performed in real space, and hence imply discretization on a finite grid. Therefore, we use discrete versions of the corresponding differential operators. Let $L$ be the edge length of the two-dimensional grid which is sample by $N$ grid points in each dimension. Hence, the spatial step size is given by $h = L/N$. Their specific values are explicitly given in each relevant section. The action of the discrete Laplace operator on a two-dimensional function $f(x, y)$ can be approximated by the five-point stencil finite difference method

$$\Delta f \approx \frac{1}{h^2} \left[ f(x_{i-1}, y_i) + f(x_{i+1}, y_i) + f(x_i, y_{i-1}) + f(x_i, y_{i+1}) - 4f(x_i, y_i) \right]. \qquad (A.1)$$

Additionally, mixed derivatives appear in the circular polarization basis due to finite TE-TM splitting of the cavity modes. The mixed derivatives are discretized in a similar way which yields

$$\frac{\partial^2 f}{\partial x \partial y} \approx \frac{1}{4h^2} \left[ f(x_{i+1}, y_{i+1}) + f(x_{i-1}, y_{i-1}) - f(x_{i+1}, y_{i-1}) - f(x_{i-1}, y_{i+1}) \right]. \qquad (A.2)$$

All $k$-space data is obtained by a two-dimensional fast Fourier transform.

# B. Derivation of the population competition model

Here, we review the derivation of the simplified PC model as it was published by us in Ref. [83]. We analyze the PC model in Chapter 3 in order to understand the orthogonal switching of polariton two-spot patterns from a nonlinear dynamical systems perspective. In principle, we follow the derivation of the hexagon PC model [85], but we include the polariton's polarization dependence which leads to a different reduced $k$-space and different interactions. Starting from the full equations of motion for the cavity and exciton field given in Eqs. (2.24) and (2.25), we transform them into the linear polarization basis and we introduce the set of modes for the reduced $k$-space $\{\mathbf{k}_0 = \mathbf{0}, \mathbf{k}_1, \mathbf{k}_2, \mathbf{k}_3, \mathbf{k}_4\}$ with $\mathbf{k}_3 = -\mathbf{k}_1$ and $\mathbf{k}_4 = -\mathbf{k}_2$; see Fig. B.1. This leaves us with 20 equations for the five modes of the two fields with two possible polarizations. The excitation is $x$-linearly polarized, which results in the following selection rules (see Sec. 3.1): (i) An $\frac{x}{y}$-polarized probe beam with $\mathbf{k} \parallel \mathbf{e}_x$ on the elastic ring excites a $\frac{\mathrm{TM}}{\mathrm{TE}}$-mode and (ii) an $\frac{x}{y}$-polarized probe beam with $\mathbf{k} \perp \mathbf{e}_x$ on the elastic ring excites a $\frac{\mathrm{TE}}{\mathrm{TM}}$-mode. Assuming all quantities oscillate with the pump's frequency $\omega$ allows us to remove the phase factor $\mathrm{e}^{-i\omega t}$ by shifting the dispersion by $-\hbar\omega$. We assume equal excitation of modes with opposite momentum in the reduced $k$-space, i.e. $p_{\mathbf{k}_1} = p_{\mathbf{k}_3} \equiv p_1$ and $p_{\mathbf{k}_2} = p_{\mathbf{k}_4} \equiv p_2$ and analogously for $E$, since the linear stability analysis in Sec. 3.1 reveals a $D_2 \cong \mathbb{Z}_2 \times \mathbb{Z}_2$ symmetry. Furthermore, we consider the modes which are directly excited by the pump, i.e. $E_0^{x/y}$ and $p_0^{x/y}$ at $\mathbf{k}_0 = \mathbf{0}$, to be constant at all times. In the following, we use a cyclic definition for pairs of opposite modes, i.e. $p_j = p_{j+2}$ with $j = 1, 2$. We also denote scattering processes as a set of the involved momenta $(\mathbf{q}, \mathbf{k}', \mathbf{k}'')$ with the phase-matching condition $\mathbf{q} = \mathbf{k} - \mathbf{k}' - \mathbf{k}''$. Then, all phase-matched scattering processes
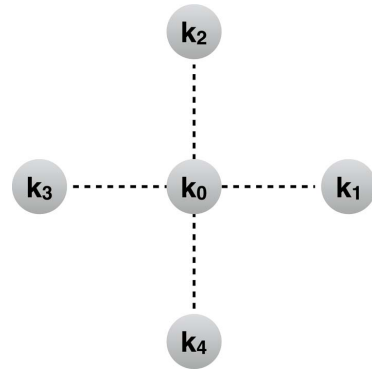


**Figure B.1.** Reduced $k$-space.

up to third order within the reduced k-space can be written as

$$(j,0,0), \ (0,j,0), \ (0,0,j), \ 3 \times (j,j,j), \ 2 \times (j,j+1,j+1). \tag{B.1}$$

Since the pump is purely $x$-linearly polarized, all terms $\propto p_0^y$ or $\propto E_0^y$ are omitted. As another consequence, the co-linearly polarized off-axis are negligible small since scattering occurs predominantly in the cross-polarization channel (see Sec. 3.1), i.e. $|p_j^x| \ll |p_j^y|$ and $|E_j^x| \ll |E_j^y|$. Thus, we arrive at four equations of motion for the $y$-linearly polarized mode pairs in the reduced $k$-space

$$i\hbar\partial_t p_j^y = (\epsilon_j - \hbar\omega - i\gamma_e)p_j^y + \tfrac{1}{2}\alpha_{\mathrm{PSF}}\Omega[-p_j^{y*}p_0^x E_0^x + p_0^{x*}p_j^y E_0^x + |p_0^x|^2 E_j^y + 3p_j^{y*}p_j^y E_j^y$$
$$+ 2p_j^{y*}p_{j+1}^y E_{j+1}^y] + \tfrac{1}{2}(T^{++} + T^{+-})\left[3p_j^{y*}p_j^y p_j^y + 2p_j^{y*}p_{j+1}^{y2}\right]$$
$$- \tfrac{1}{2}(T^{++} - T^{+-})\left[p_j^{y*}p_0^{x2}\right] + T^{++}|p_0^x|^2 p_j^y - \Omega E_j^y, \tag{B.2}$$
$$i\hbar\partial_t E_j^y = (\hbar\omega_j^y - \hbar\omega - i\gamma_c)E_j^y - \Omega p_j^y + E_{\mathrm{ext},j}^y. \tag{B.3}$$

Assuming the time evolution of $E$ adiabatically follows the evolution of $p$ and setting $\partial_t E_j \approx 0$, we find the following relation

$$E_j = \frac{\Omega}{\hbar\omega_j - \delta_j - \hbar\omega - i\gamma_c} p_j \equiv \frac{2\lambda_j}{\alpha_{\mathrm{PSF}}\Omega} e^{i\theta_j} p_j. \tag{B.4}$$

The external field $E_{\mathrm{ext},j}^y$ was also removed and will be added again later. The phase between $E_j^y$ and $p_j^y$ is denoted as $\theta_j$ and the ratio of their magnitude is given by $|E_j^y|/|p_j^y| = \frac{2\lambda_j}{\alpha_{\mathrm{PSF}}\Omega}$. The parameter $\delta_j$ accounts for the anisotropy effects due to tilting the pump and a higher density of states for TE modes; see Sec. 3.1. In conclusion,

$$\lambda_j e^{i\theta_j} = \frac{\alpha_{\mathrm{PSF}}\Omega^2}{2(\hbar\omega_j^y - \delta_j - \hbar\omega - i\gamma_c)} \qquad \text{for } j = 1, 2, \tag{B.5}$$

$$\lambda_0 e^{i\theta_0} = \frac{\alpha_{\mathrm{PSF}}\Omega^2}{2(\hbar\omega_0^x - \hbar\omega - i\gamma_c)} \qquad \text{for } j = 0. \tag{B.6}$$

With these definitions we obtain two equations of motion for $p_1^y$ and $p_2^y$. Moreover, we rewrite the exciton field into $p_j^y \equiv \tilde{p}_j^y e^{i\varphi_j}$, which allows us to split the dynamics into separate equations for the phase phase and the magnitude:

$$\partial_t \tilde{p}_j^y = L_j \tilde{p}_j^y + \sum_{k=1}^{2} C_{jk}\tilde{p}_k^{y2}\tilde{p}_j^y \tag{B.7}$$

$$\partial_t \varphi_j = K_j + \sum_{k=1}^{2} D_{jk}\tilde{p}_k^{y2}. \tag{B.8}$$

We define the phase difference $\phi_j \equiv \varphi_j - \varphi_0$, so that the coefficients in Eqs. (B.7) and (B.8) are given by

$$\hbar L_j = -\gamma_e + \lambda_0 \tilde{p}_o^{x2}(\sin(\theta_0) - \sin(\theta_0 - 2\phi_j)) + \lambda_j \sin(\theta_j)\left(\tilde{p}_0^{x2} - \tfrac{2}{\alpha_{\mathrm{PSF}}}\right)$$
$$- \tfrac{1}{2}(T^{++} - T^{+-})\tilde{p}_0^{x2}\sin(-2\phi_j) \tag{B.9}$$

$$\hbar C_{jk} = \begin{cases} 3\lambda_j \sin(\theta_j) & , \; j = k \\ 2\lambda_k \sin(\theta_k + 2\phi_k - 2\phi_j) + (T^{++} + T^{+-})\sin(2\phi_k - 2\phi_j) & , \; j \neq k \end{cases} \tag{B.10}$$

$$\hbar K_j = \epsilon_j - \hbar\omega - T^{++}\tilde{p}_0^{x2}(\cos(\theta_0) - \cos(\theta_0) - 2\phi_j) - \lambda_j \cos(\theta_j)\left(\tilde{p}_0^{x2} - \tfrac{2}{\alpha_{\mathrm{PSF}}}\right)$$
$$- \tfrac{1}{2}(T^{++} - T^{+-})\tilde{p}_0^{x2}\cos(-2\phi_j) \tag{B.11}$$

$$\hbar D_{jk} = \begin{cases} -3\lambda_j \cos(\theta_j) - \tfrac{3}{2}(T^{++} + T^{+-}) & , \; j = k \\ -2\lambda_k \cos(\theta_k + 2\phi_k - 2\phi_j) - (T^{++} + T^{+-})\cos(2\phi_k - 2\phi_j) & , \; j \neq k \end{cases} . \tag{B.12}$$

Similarly to Ref. [85], the phases as dynamical variables can be removed by assuming them to be locked and linearizing Eqs. (B.7) and (B.8). We denote the time-dependent phases as $\phi_j(t) \equiv \delta\phi_j(t) + \phi_j^{(0)}$ where $\phi_j^{(0)}$ are the locked phases which are determined by $K_j(\phi_j^{(0)}) = 0$ and $\delta\phi_j(t)$ are small perturbations. Expanding Eqs. (B.7) and (B.8) up to first order in $\delta\phi_j$ around $\phi_j^{(0)}$ and neglecting terms $\propto \delta\phi_j \tilde{p}_k^{y2}$ results in an explicit expression for $\delta\phi_j$. The latter can then be substituted back into Eq. (B.7) to obtain

$$\partial \tilde{p}_j^y = \left[ L_j(\phi_j^{(0)}) + \sum_{k=1}^{2}\left( C_{jk}(\phi_j^{(0)}, \phi_k^{(0)}) - \tfrac{D_{jk}(\phi_j^{(0)}, \phi_k^{(0)})L_j'(\phi_j^{(0)})}{K_j'(\phi_j^{(0)})} \right)\tilde{p}_k^{y2} \right]\tilde{p}_j^y. \tag{B.13}$$

In short, these two equations can be written as

$$\partial_t \tilde{p}_1^y = \tilde{\alpha}_1 \tilde{p}_1^y - \tilde{\beta}_1 \tilde{p}_1^{y3} - \tilde{\theta}_1 \tilde{p}_2^{y2}\tilde{p}_1^y,$$
$$\partial_t \tilde{p}_2^y = \tilde{\alpha}_2 \tilde{p}_2^y - \tilde{\beta}_2 \tilde{p}_2^{y3} - \tilde{\theta}_2 \tilde{p}_1^{y2}\tilde{p}_2^y. \tag{B.14}$$

In order to de-dimensionalize the equations of motion, we replace $\tilde{p}_j^y$ by a product of a dimensionless quantity $\hat{\tilde{p}}_j^y$ and a characteristic quantity $\tilde{p}_{j,c}^y$. The latter has the original dimension. This results in $\tilde{p}_j^y = \hat{\tilde{p}}_j^y \cdot \tilde{p}_{j,c}^y$. Analogously, the independent time variable is replaced by $t = \hat{t} \cdot t_c$, which leads to the derivative changing to $\frac{\partial \tilde{p}_j^y}{\partial t} = \frac{\tilde{p}_{j,c}^y}{t_c}\frac{\partial \hat{\tilde{p}}_j^y}{\partial \hat{t}}$. Now we can chose characteristic values so that the corresponding dimensionless quantities are of unit magnitude. Finally, we denote $t \equiv \hat{t}$ and $A_j \equiv \hat{\tilde{p}}_j^y$ and arrive at the PC model

$$\partial_t A_1 = \alpha_1 A_1 - \beta_1 A_1^3 - \theta_1 A_2^2 A_1,$$
$$\partial_t A_2 = \alpha_2 A_2 - \beta_2 A_2^3 - \theta_2 A_1^2 A_2 + S, \tag{B.15}$$

where $S$ is a manually added a control parameter acting on the $A_2$ mode pair.

# C. PC model solutions for the inhomogeneous case

On the following four pages the explicit expressions for the steady-state solutions of the inhomogeneous case of the PC model in Sec. 3.2.2 are displayed. They are exports of the corresponding MAPLE worksheets. Capital letter $I$ denotes the imaginary unit, but all solutions are real-valued in the considered parameter regions. These expression are included for the sake of completeness only and therefore displayed in a smaller font size.

**steady state T$_2$ :**

$A_1 := 0;$

$A_2 := \dfrac{1}{6}$ ...

## *Larger cross–saturation*

**steady state F$_1$ :**

$A_1 :=$ ...

**steady state F_2:**

$A_1 :=$

$A_2 :=$

$$A_2 := \frac{1}{12}\,12^{1/3}\left(\cdots\right)$$

$$+\sqrt[3]{\ \frac{4\,\theta_2^3\,\alpha_2^3-12\,\theta_2^2\,\alpha_2^2\,\alpha_1\,\beta_1+12\,\theta_2\,\alpha_1\,\alpha_2\,\beta_1^2-4\,\alpha_2^3\,\beta_1^3+27\,S^2\,\beta_1^3\,\beta_2-27\,S^2\,\beta_1^2\,\theta_2\,\theta_1}{\beta_2\,\beta_1-\theta_2\,\theta_1}\ \frac{\beta_2^2\,\beta_1^2}{\theta_2^2\,\theta_1^2}\ }$$

$$-2\sqrt[3]{\ \frac{4\,\theta_2^3\,\alpha_2^3-12\,\theta_2^2\,\alpha_2^2\,\alpha_1\,\beta_1+12\,\theta_2\,\alpha_1\,\alpha_2\,\beta_1^2-4\,\alpha_2^3\,\beta_1^3+27\,S^2\,\beta_1^3\,\beta_2-27\,S^2\,\beta_1^2\,\theta_2\,\theta_1}{\beta_2\,\beta_1-\theta_2\,\theta_1}\ }$$

**steady state F₁ :**

$$\mathcal{A}_1$$

$$:= \frac{1}{36}\left(\sqrt[3]{12^{2/3}}\left(\beta_1\left(\left(\beta_2\,\beta_1-\theta_2\,\theta_1\right)^2\sqrt[3]{\dfrac{4\,\theta_2^3\,\alpha_1^3-12\,\theta_2^2\,\alpha_1^2\,\alpha_2\,\beta_1+12\,\theta_2\,\alpha_1\,\alpha_2^2\,\beta_1^2-4\,\alpha_2^3\,\beta_1^3+27\,S^2\,\beta_1^3\,\beta_2-27\,S^2\,\beta_1^2\,\theta_2\,\theta_1}{\beta_2\,\beta_1-\theta_2\,\theta_1}}\,\,9\,S\,\beta_1}\right.\right.$$

$$+\sqrt[3]{\dfrac{4\,\theta_2^3\,\alpha_1^3-12\,\theta_2^2\,\alpha_1^2\,\alpha_2\,\beta_1+12\,\theta_2\,\alpha_1\,\alpha_2^2\,\beta_1^2-4\,\alpha_2^3\,\beta_1^3+27\,S^2\,\beta_1^3\,\beta_2-27\,S^2\,\beta_1^2\,\theta_2\,\theta_1}{\beta_2\,\beta_1-\theta_2\,\theta_1}}\left(\left(\beta_2\,\beta_1-\theta_2\,\theta_1\right)^2\right)\,9\,S\,\beta_1}$$

$$\alpha_2^2\,\beta_2\,\beta_1-9\,\beta_1^2\,\theta_1\,12^{1/3}\left(\left(\beta_2\,\beta_1-\theta_2\,\theta_1\right)^2\right)$$

$$+\sqrt[3]{\dfrac{4\,\theta_2^3\,\alpha_1^3-12\,\theta_2^2\,\alpha_1^2\,\alpha_2\,\beta_1+12\,\theta_2\,\alpha_1\,\alpha_2^2\,\beta_1^2-4\,\alpha_2^3\,\beta_1^3+27\,S^2\,\beta_1^3\,\beta_2-27\,S^2\,\beta_1^2\,\theta_2\,\theta_1}{\beta_2\,\beta_1-\theta_2\,\theta_1}}}$$

$$S+24\,\beta_1^2\,\beta_2\,\theta_1\,\alpha_1\,\alpha_2$$

$$-12\,\beta_1\,\theta_1\,\theta_2^2\,\alpha_1^2+12\,\beta_1^2\,\alpha_2^2\,\theta_1+3\,\beta_1\,\alpha_1\,12^{2/3}\left(\left(\beta_2\,\beta_1-\theta_2\,\theta_1\right)^2\right)$$

$$+\sqrt[3]{\dfrac{4\,\theta_2^3\,\alpha_1^3-12\,\theta_2^2\,\alpha_1^2\,\alpha_2\,\beta_1+12\,\theta_2\,\alpha_1\,\alpha_2^2\,\beta_1^2-4\,\alpha_2^3\,\beta_1^3+27\,S^2\,\beta_1^3\,\beta_2-27\,S^2\,\beta_1^2\,\theta_2\,\theta_1}{\beta_2\,\beta_1-\theta_2\,\theta_1}}}$$

$$-\beta_1\,\beta_2\,12^{1/3}\left(\left(\beta_2\,\beta_1-\theta_2\,\theta_1\right)^2\right)\,9\,S\,\beta_1$$

$$+\sqrt[3]{\dfrac{4\,\theta_2^3\,\alpha_1^3-12\,\theta_2^2\,\alpha_1^2\,\alpha_2\,\beta_1+12\,\theta_2\,\alpha_1\,\alpha_2^2\,\beta_1^2-4\,\alpha_2^3\,\beta_1^3+27\,S^2\,\beta_1^3\,\beta_2-27\,S^2\,\beta_1^2\,\theta_2\,\theta_1}{\beta_2\,\beta_1-\theta_2\,\theta_1}}}$$

$$-2\,\beta_1\,\theta_1\,12^{2/3}\left(\left(\beta_2\,\beta_1-\theta_2\,\theta_1\right)^2\right)\,9\,S\,\beta_1$$

$$+\sqrt[3]{\dfrac{4\,\theta_2^3\,\alpha_1^3-12\,\theta_2^2\,\alpha_1^2\,\alpha_2\,\beta_1+12\,\theta_2\,\alpha_1\,\alpha_2^2\,\beta_1^2-4\,\alpha_2^3\,\beta_1^3+27\,S^2\,\beta_1^3\,\beta_2-27\,S^2\,\beta_1^2\,\theta_2\,\theta_1}{\beta_2\,\beta_1-\theta_2\,\theta_1}}}$$

$$-\alpha_1\,12^{2/3}\left(\left(\beta_2\,\beta_1-\theta_2\,\theta_1\right)^2\right)\,9\,S\,\beta_1\,\alpha_2$$

$$+1\,\sqrt[3]{12^{1/3}}\,\theta_2\,\beta_1\,\alpha_2\,\beta_2\,\beta_1-1\,\sqrt[3]{12^{1/3}}\,\theta_2^2\,\alpha_1\,\theta_1-1\,\sqrt[3]{12^{1/3}}\,\alpha_2\,\beta_1^2\,\beta_2+1\,\sqrt[3]{12^{1/3}}\,\alpha_2\,\beta_1\,\theta_2\,\theta_1\Big)\Big)\Big/\left(\left(\beta_2\,\beta_1\right.\right.$$

$$-\theta_2\,\theta_1\Big)\Big)$$

$$+\sqrt[3]{\dfrac{4\,\theta_2^3\,\alpha_1^3-12\,\theta_2^2\,\alpha_1^2\,\alpha_2\,\beta_1+12\,\theta_2\,\alpha_1\,\alpha_2^2\,\beta_1^2-4\,\alpha_2^3\,\beta_1^3+27\,S^2\,\beta_1^3\,\beta_2-27\,S^2\,\beta_1^2\,\theta_2\,\theta_1}{\beta_2\,\beta_1-\theta_2\,\theta_1}}\left(\left(\beta_2\,\beta_1-\theta_2\,\theta_1\right)^2\right)}^{1/3};$$

Second part:

$$+\sqrt[3]{\dfrac{4\,\theta_2^3\,\alpha_1^3-12\,\theta_2^2\,\alpha_1^2\,\alpha_2\,\beta_1+12\,\theta_2\,\alpha_1\,\alpha_2^2\,\beta_1^2-4\,\alpha_2^3\,\beta_1^3+27\,S^2\,\beta_1^3\,\beta_2-27\,S^2\,\beta_1^2\,\theta_2\,\theta_1}{\beta_2\,\beta_1-\theta_2\,\theta_1}}}^{2/3}$$

$$\theta_1^2\,12^{1/3}\left(\left(\beta_2\,\beta_1-\theta_2\,\theta_1\right)^2\right)\,9\,S\,\beta_1$$

$$+\sqrt[3]{\dfrac{4\,\theta_2^3\,\alpha_1^3-12\,\theta_2^2\,\alpha_1^2\,\alpha_2\,\beta_1+12\,\theta_2\,\alpha_1\,\alpha_2^2\,\beta_1^2-4\,\alpha_2^3\,\beta_1^3+27\,S^2\,\beta_1^3\,\beta_2-27\,S^2\,\beta_1^2\,\theta_2\,\theta_1}{\beta_2\,\beta_1-\theta_2\,\theta_1}}}^{1/3}\,S\,\theta_2-24\,\beta_1^2\,\theta_2^2\,\alpha_1\,\alpha_2\,\theta_1^2+$$

$$\theta_1^2\,12^{1/3}\left(\left(\beta_2\,\beta_1-\theta_2\,\theta_1\right)^2\right)\,9\,S\,\beta_1$$

$$+\sqrt[3]{\dfrac{4\,\theta_2^3\,\alpha_1^3-12\,\theta_2^2\,\alpha_1^2\,\alpha_2\,\beta_1+12\,\theta_2\,\alpha_1\,\alpha_2^2\,\beta_1^2-4\,\alpha_2^3\,\beta_1^3+27\,S^2\,\beta_1^3\,\beta_2-27\,S^2\,\beta_1^2\,\theta_2\,\theta_1}{\beta_2\,\beta_1-\theta_2\,\theta_1}}}\,\theta_2+12\,\theta_1^3\,\alpha_1^2\,\theta_1^2\right)^{1/2}\Bigg/$$

$$\left(\left(\left(\beta_2\,\beta_1-\theta_2\,\theta_1\right)^2\right)\sqrt[3]{\dfrac{4\,\theta_2^3\,\alpha_1^3-12\,\theta_2^2\,\alpha_1^2\,\alpha_2\,\beta_1+12\,\theta_2\,\alpha_1\,\alpha_2^2\,\beta_1^2-4\,\alpha_2^3\,\beta_1^3+27\,S^2\,\beta_1^3\,\beta_2-27\,S^2\,\beta_1^2\,\theta_2\,\theta_1}{\beta_2\,\beta_1-\theta_2\,\theta_1}}}\,\beta_1\left(\beta_2\,\beta_1-\theta_2\,\theta_1\right)\right);$$

$$\mathcal{A}_2$$

$$:= \frac{1}{6}\frac{1}{\beta_2\,\beta_1-\theta_2\,\theta_1}\sqrt[3]{108\,S\,\beta_1}$$

$$+12\sqrt{3}\sqrt{\dfrac{4\,\theta_2^3\,\alpha_1^3-12\,\theta_2^2\,\alpha_1^2\,\alpha_2\,\beta_1+12\,\theta_2\,\alpha_1\,\alpha_2^2\,\beta_1^2-4\,\alpha_2^3\,\beta_1^3+27\,S^2\,\beta_1^3\,\beta_2-27\,S^2\,\beta_1^2\,\theta_2\,\theta_1}{\beta_2\,\beta_1-\theta_2\,\theta_1}}\left(\beta_2\,\beta_1-\theta_2\,\theta_1\right)^2}$$

$$-\left(2\left(\theta_2\,\alpha_1-\alpha_2\,\beta_1\right)\right)\Bigg/\left[\left(108\,S\,\beta_1+12\,\sqrt{3}\right.\right.$$

# D. Half-vortex stability with dynamical noise and static disorder

To further evidence dynamical stability of the half-vortices presented in Chapter 4 including TE-TM splitting and attractive cross-interaction, we study the long-time dynamics under the influence of (i) dynamical solution-related noise and (ii) a static disorder potential.

Figure D.1(b) shows the time evolution of the peak densities for both polarization components under the influence of dynamical noise. Here, we use complex white noise scaled with 5% the solution's amplitude which is generated and added every picosecond. Figure D.1(a) shows an exemplary time snapshot of the densities and phase distributions. The half-vortex remains stable over a long time evolution of $T = 10$ ns.

Figure D.1(d) shows the time evolution of the peak densities for both polarization components under the influence of a static disorder potential. The latter is generated via random numbers on the spatial grid which are then averaged over about a 1 $\mu$m radius to simulate a finite correlation length. The average disorder amplitude is about $\sqrt{\langle V_0^2 \rangle} \approx 0.055$ meV. Figure D.1(c) shows an exemplary time snapshot of the densities and phase distributions. The half-vortex is clearly deformed in the presence of the disorder potential but remains stable over a long time evolution of $T = 10$ ns.
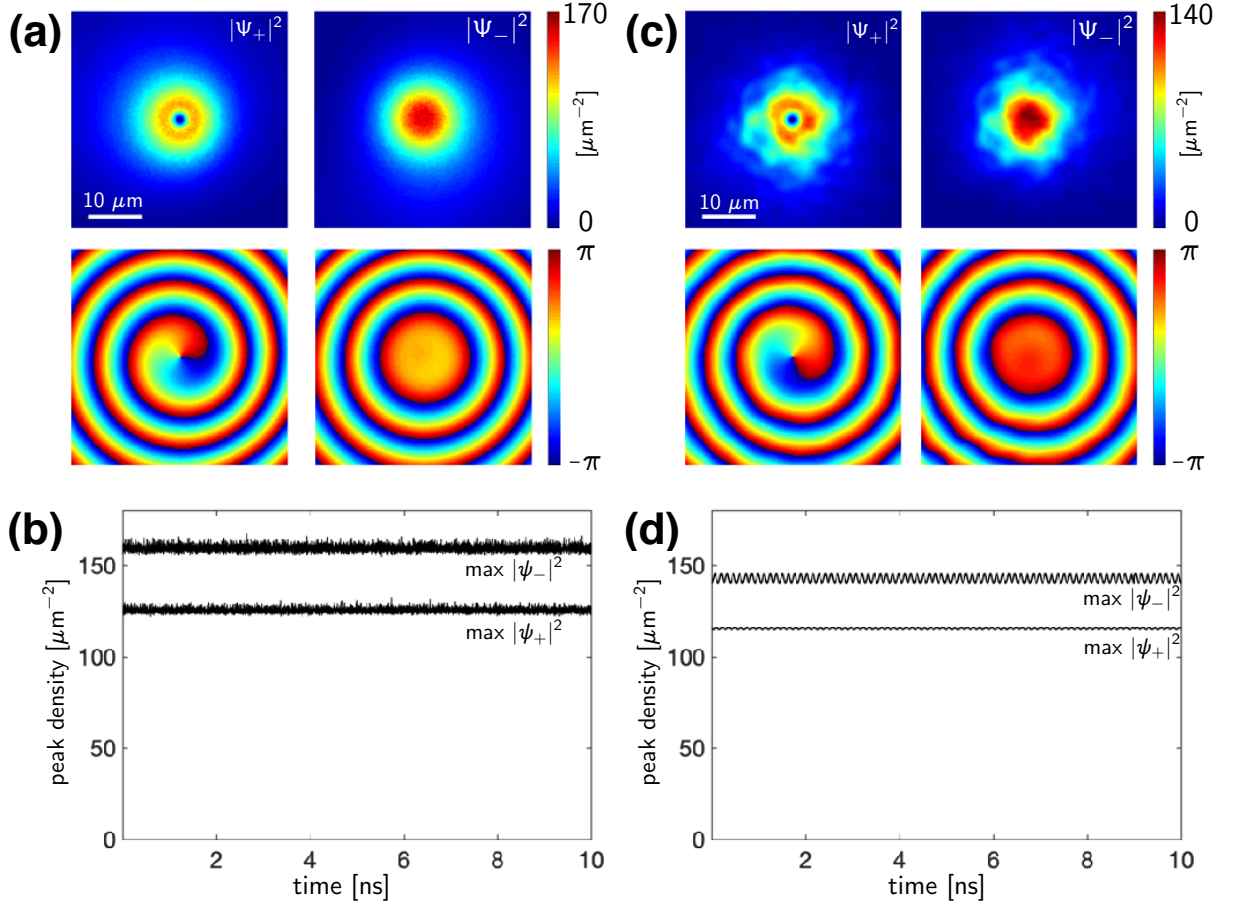
**Figure D.1.** (a) Time-snapshot of density and phase distributions of half-vortex state $(-1, 0)$ under the influence of dynamical noise scaled with 5% the solution's amplitude. Panel (c) shows the corresponding time evolution of the peak densities for a time interval of 10 ns. (c) Time-snapshot of density and phase distributions of half-vortex state $(-1, 0)$ under the influence of a static disorder potential with average amplitude of about $\sqrt{\langle V_0^2 \rangle} \approx 0.055$ meV and a correlation length of about 1 $\mu$m. Panel (d) shows the corresponding time evolution of the peak densities for a time interval of 10 ns.

# E. Statistical errors

All coherence properties determined in Chapter 5 are based on the time-averaged mean $A \equiv \overline{\langle \hat{n}_c \rangle}$ and variance $B \equiv \overline{\langle (\Delta \hat{n}_c)^2 \rangle}$ of the condensate occupation number operator. From $N_t$ samples in time we calculate mean and standard deviation via:

$$\overline{x} = \frac{1}{N_t} \sum_{i=1}^{N_t} x_i, \tag{E.1}$$

$$\Delta x = \sqrt{\frac{1}{N_t(N_t - 1)} \sum_{i=1}^{N_t} (x_i - \overline{x})^2}, \tag{E.2}$$

where $x \in \{A, B\}$. All errors of consequent quantities $f(A, B)$ are calculated via error propagation assuming $A$ and $B$ having a small covariance compared to their isolated variances, explicitly

$$\Delta f(A, B) = \sqrt{\left(\frac{\partial f}{\partial A}\right)^2 (\Delta A)^2 + \left(\frac{\partial f}{\partial B}\right)^2 (\Delta B)^2}. \tag{E.3}$$

This process results in the following standard deviations which are displayed in the plots throughout Chapter 5:

$$\Delta |\alpha_0|^2(A, B) = \sqrt{\left(\frac{2A + 1}{2\sqrt{A^2 + A - B}}\right)^2 (\Delta A)^2 + \left(\frac{1}{2\sqrt{A^2 + A - B}}\right)^2 (\Delta B)^2}, \tag{E.4}$$

$$\Delta \bar{n}(A, B) = \sqrt{\left(1 - \frac{2A + 1}{2\sqrt{A^2 + A - B}}\right)^2 (\Delta A)^2 + \left(\frac{1}{2\sqrt{A^2 + A - B}}\right)^2 (\Delta B)^2}, \tag{E.5}$$

$$\Delta g^{(2)}(A, B) = \sqrt{\left(\frac{A^2 - 2AB}{A^4}\right)^2 (\Delta A)^2 + \left(\frac{\Delta B}{A^2}\right)^2}, \tag{E.6}$$

$$\Delta \mathscr{C}(|\alpha_0|^2, \bar{n}) = \sqrt{(\Delta \mathscr{C}_1)^2 (\Delta |\alpha_0|^2)^2 + (\Delta \mathscr{C}_2)^2 (\Delta \bar{n})^2}, \tag{E.7}$$

with

$$\Delta \mathscr{C}_1 = -\frac{2I_1}{(2\bar{n}+1)^2},$$ (E.8)

$$\Delta \mathscr{C}_2 = \frac{-2 + 2I_0 + \frac{4|\alpha_0|^2}{2\bar{n}+1} I_1}{(2\bar{n}+1)^2},$$ (E.9)

where the integrals are given by

$$I_0 = \frac{1}{2\pi} \int_0^{2\pi} d\varphi \exp\left[\frac{2|\alpha_0|^2}{2\bar{n}+1}(\cos\varphi - 1)\right],$$ (E.10)

$$I_1 = \frac{1}{2\pi} \int_0^{2\pi} d\varphi \exp\left[\frac{2|\alpha_0|^2}{2\bar{n}+1}(\cos\varphi - 1)\right](\cos\varphi - 1).$$ (E.11)

# Bibliography

[1] A. Kavokin, J. J. Baumberg, G. Malpuech, and F. P. Laussy, *Microcavities* (Oxford University Press, New York, 2008).

[2] H. Haug and S. W. Koch, *Quantum theory of the optical and electronic properties of semiconductors, fifth edition* (World Scientific Publishing Co., 2009).

[3] J. J. Hopfield, Theory of the Contribution of Excitons to the Complex Dielectric Constant of Crystals, Physical Review **112**, 1555 (1958).

[4] S. I. Pekar, The theory of electromagnetic waves in a crystal in which excitons are produced, Journal of Experimental and Theoretical Physics **6**, 785 (1958).

[5] V. M. Agranovich, Dispersion of electromagnetic waves in crystals, Journal of Experimental and Theoretical Physics **10**, 307 (1960).

[6] C. Weisbuch, M. Nishioka, A. Ishikawa, and Y. Arakawa, Observation of the coupled exciton-photon mode splitting in a semiconductor quantum microcavity, Physical Review Letters **69**, 3314 (1992).

[7] A. Kavokin, G. Malpuech, and M. Glazov, Optical Spin Hall Effect, Physical Review Letters **95**, 136601 (2005).

[8] C. Leyder, M. Romanelli, J. P. Karr, E. Giacobino, T. C. H. Liew, M. M. Glazov, A. V. Kavokin, G. Malpuech, and A. Bramati, Observation of the optical spin Hall effect, Nature Physics **3**, 628 (2007).

[9] Y. G. Rubo, Half Vortices in Exciton Polariton Condensates, Physical Review Letters **99**, 106401 (2007).

[10] S. Schumacher, Spatial anisotropy of polariton amplification in planar semiconductor microcavities induced by polarization anisotropy, Physical Review B **77**, 073302 (2008).

[11] E. Kammann, T. C. H. Liew, H. Ohadi, P. Cilibrizzi, P. Tsotsis, Z. Hatzopoulos, P. G. Savvidis, A. V. Kavokin, and P. G. Lagoudakis, Nonlinear Optical Spin Hall

Effect and Long-Range Spin Transport in Polariton Lasers, Physical Review Letters **109**, 036404 (2012).

[12] I. A. Shelykh, A. V. Kavokin, Y. G. Rubo, T. C. H. Liew, and G. Malpuech, Polariton polarization-sensitive phenomena in planar semiconductor microcavities, Semiconductor Science and Technology **25**, 013001 (2009).

[13] P. G. Savvidis, J. J. Baumberg, R. M. Stevenson, M. S. Skolnick, D. M. Whittaker, and J. S. Roberts, Angle-Resonant Stimulated Polariton Amplifier, Physical Review Letters **84**, 1547 (2000).

[14] R. M. Stevenson, V. N. Astratov, M. S. Skolnick, D. M. Whittaker, M. Emam-Ismail, A. I. Tartakovskii, P. G. Savvidis, J. J. Baumberg, and J. S. Roberts, Continuous Wave Observation of Massive Polariton Redistribution by Stimulated Scattering in Semiconductor Microcavities, Physical Review Letters **85**, 3680 (2000).

[15] J. J. Baumberg, P. G. Savvidis, R. M. Stevenson, A. I. Tartakovskii, M. S. Skolnick, D. M. Whittaker, and J. S. Roberts, Parametric oscillation in a vertical microcavity: A polariton condensate or micro-optical parametric oscillation, Physical Review B **62**, 16247(R) (2000).

[16] C. Ciuti, P. Schwendimann, and A. Quattropani, Theory of polariton parametric interactions in semiconductor microcavities, Semiconductor Science and Technology **18**, 279 (2003).

[17] R. Kheradmand, M. Sahrai, H. Tajalli, G. Tissoni, and L. A. Lugiato, All optical switching in semiconductor microresonators based on pattern selection, The European Physical Journal D **47**, 107 (2008).

[18] V. Ardizzone, P. Lewandowski, M. H. Luk, Y. C. Tse, N. H. Kwong, A. Lücke, M. Abbarchi, E. Baudin, E. Galopin, J. Bloch, A. Lemaitre, P. T. Leung, P. Roussignol1, R. Binder, J. Tignon, and S. Schumacher, Formation and control of Turing patterns in a coherent quantum fluid, Scientific Reports **3**, 3016 (2013).

[19] S. Schumacher, N. H. Kwong, R. Binder, and A. L. Smirl, Low intensity directional switching of light in semiconductor microcavities, Physica Status Solidi RRL **3**, 10 (2009).

[20] M. Romanelli, C. Leyder, J. P. Karr, E. Giacobino, and A. Bramati, Four Wave Mixing Oscillation in a Semiconductor Microcavity: Generation of Two Correlated Polariton Populations, Physical Review Letters **98**, 106401 (2007).

[21] D. Sanvitto, F. M. Marchetti, M. H. Szymańska, G. Tosi, M. Baudisch, F. P. Laussy, D. N. Krizhanovskii, M. S. Skolnick, L. Marrucci, A. Lemaître, J. Bloch, C. Tejedor,

and L. Viña, Persistent currents and quantized vortices in a polariton superfluid, Nature Physics **6**, 527 (2010).

[22] P. Lewandowski, S. M. H. Luk, C. K. P. Chan, P. T. Leung, N. H. Kwong, R. Binder, and S. Schumacher, Directional optical switching and transistor functionality using optical parametric oscillation in a spinor polariton fluid, Optics Express **25**, 31056 (2017).

[23] H. Deng, G. Weihs, C. Santori, J. Bloch, and Y. Yamamoto, Condensation of Semiconductor Microcavity Exciton Polaritons, Science **298**, 199 (2002).

[24] J. Kasprzak, M. Richard, S. Kundermann, A. Baas, P. Jeambrun, J. M. J. Keeling, F. M. Marchetti, M. H. Szymańska, R. André, J. L. Staehli, V. Savona, P. B. Littlewood, B. Deveaud, and L. S. Dang, Bose–Einstein condensation of exciton polaritons, Nature **443**, 409 (2006).

[25] H. Deng, H. Haug, and Y. Yamamoto, Exciton-polariton Bose-Einstein condensation, Reviews of Modern Physics **82**, 1489 (2010).

[26] I. Carusotto and C. Ciuti, Quantum fluids of light, Reviews of Modern Physics **85**, 299 (2013).

[27] S. Savasta, and R. Girlanda, Cavity polaritons beyond the boson approximation, Il Nuovo Cimento D **17**, 1705 (1995).

[28] S. Christopoulos, G. Baldassarri Höger von Högersthal, A. J. D. Grundy, P. G. Lagoudakis, A. V. Kavokin, J. J. Baumberg, G. Christmann, R. Butté, E. Feltin, J.-F. Carlin, and N. Grandjean, Room-Temperature Polariton Lasing in Semiconductor Microcavities, Physical Review Letters **98**, 126405 (2006).

[29] G. Christmann, R. Butté, E. Feltin, J.-F. Carlin, and N. Grandjean, Room temperature polariton lasing in a GaN / AlGaN multiple quantum well microcavity, Applied Physics Letters **93**, 051102 (2008).

[30] G. Lerario, A. Fieramosca, F. Barachati, D. Ballarini, K. S. Daskalakis, L. Dominici, M. De Giorgi, S. A. Maier, G. Gigli, S. Kéna-Cohen, and D. Sanvitto, Room-temperature superfluidity in a polariton condensate, Nature Physics **13**, 837 (2017).

[31] G. Roumpos, M. Lohse, W. H. Nitsche, J. Keeling, M. H. Szymańska, P. B. Littlewood, A. Löffler, S. Höfling, L. Worschech, A. Forchel, Y. Yamamoto, Power-law decay of the spatial correlation function in exciton-polariton condensates, Proceedings of the National Academy of Sciences **109**, 6467 (2012).

[32] W. H. Nitsche, N. Y. Kim, G. Roumpos, C. Schneider, M. Kamp, S. Höfling, A. Forchel, and Y. Yamamoto, Algebraic order and the Berezinskii-Kosterlitz-Thouless transition in an exciton-polariton gas, Physical Review B **90**, 205430 (2014).

[33] D. Caputo, D. Ballarini, G. Dagvadorj, C. S. Muñoz, M. De Giorgi, L. Dominici, K. West, L. N. Pfeiffer, G. Gigli, F. P. Laussy, M. H. Szymańska, and D. Sanvitto, Topological order and thermal equilibrium in polariton condensates, Nature Materials **17**, 145 (2018).

[34] P. Comaron, G. Dagvadorj, A. Zamora, I. Carusotto, N. P. Proukakis, and M. H. Szymańska, Dynamical Critical Exponents in Driven-Dissipative Quantum Systems, Physical Review Letters **121**, 095302 (2018).

[35] G. Dagvadorj, M. Kulczykowski, M. H. Szymańska, and M. Matuszewski, First-order dissipative phase transition in an exciton-polariton condensate, Physical Review B **104**, 165301 (2021).

[36] C. Schneider, K. Winkler, M. D. Fraser, M. Kamp, Y. Yamamoto, E. A. Ostrovskaya and S. Höfling, Exciton-polariton trapping and potential landscape engineering, Reports on Progress in Physics **80**, 016503 (2016).

[37] T. Boulier, M. Bamba, A. Amo, C. Adrados, A. Lemaitre, E. Galopin, I. Sagnes, J. Bloch, C. Ciuti, E. Giacobino, and A. Bramati, Polariton-generated intensity squeezing in semiconductor micropillars, Nat. Commun. **5**, 3260 (2014).

[38] J. C. López Carreño, C. Sánchez Muñoz, D. Sanvitto, E. del Valle, and F. P. Laussy, Exciting Polaritons with Quantum Light, Physical Review Letters **115**, 196402 (2015).

[39] Á. Cuevas, J. C. López Carreño, B. Silva, M. De Giorgi, D. G. Suárez-Forero, C. Sánchez Muñoz, A. Fieramosca, F. Cardano, L. Marrucci, V. Tasco, G. Biasiol, E. del Valle, L. Dominici, D. Ballarini, G. Gigli, P. Mataloni, F. P. Laussy, F. Sciarrino, and D. Sanvitto, First observation of the quantized exciton-polariton field and effect of interactions on a single polariton, Science Advances **4**, eaao6814 (2018).

[40] A. Delteil, T. Fink, A. Schade, S. Höfling, C. Schneider, and A. İmamoğlu, Towards polariton blockade of confined exciton–polaritons, Nature Materials **18**, 219 (2019).

[41] G. Muñoz-Matutano, A. Wood, M. Johnsson, X. Vidal, B. Q. Baragiola, A. Reinhard, A. Lemaître, J. Bloch, A. Amo, G. Nogues, B. Besga, M. Richard, and T. Volz, Emergence of quantum correlations from interacting fibre-cavity polaritons, Nature Materials **18**, 213 (2019).

[42] Y. Xue, I. Chestnov, E. Sedov, E. Kiktenko, A. K. Fedorov, S. Schumacher, X. Ma, and A. Kavokin, Split-ring polariton condensates as macroscopic two-level quantum systems, Physical Review Research **3**, 013099 (2021).

[43] C. Lüders, M. Pukrop, E. Rozas, C. Schneider, S. Höfling, J. Sperling, S. Schumacher and M. Aßmann, Quantifying quantum coherence in polariton condensates, PRX Quantum **2**, 030320 (2021).

[44] M. H. Luk, Y. C. Tse, N. H. Kwong, P. T. Leung, P. Lewandowski, R. Binder, and S. Schumacher, Transverse optical instability patterns in semiconductor microcavities: Polariton scattering and low-intensity all-optical switching, Physical Review B **87**, 205307 (2013).

[45] M. Lindberg and S. W. Koch, Effective Bloch equations for semiconductors, Physical Review B **38**, 3342 (1988).

[46] R. Takayama, N. H. Kwong, I. Rumyantsev, M. Kuwata-Gonokami, and R. Binder, T-matrix analysis of biexcitonic correlations in the nonlinear optical response of semiconductor quantum wells, The European Physical Journal B - Condensed Matter and Complex Systems **25**, 445–462 (2002).

[47] V. M. Axt and A. Stahl, A dynamics-controlled truncation scheme for the hierarchy of density matrices in semiconductor optics, Zeitschrift für Physik B - Condensed Matter **93**, 195–204 (1994).

[48] M. Lindberg, Y. Z. Hu, R. Binder, and S. W. Koch, $\chi^{(3)}$ formalism in optically excited semiconductors and its applications in four-wave-mixing spectroscopy, Physical Review B **50**, 18060 (1994).

[49] G. Panzarini, L. C. Andreani, A. Armitage, D. Baxter, M. S. Skolnick, V. N. Astratov, J. S. Roberts, A. V. Kavokin, M. R. Vladimirova, and M. A. Kaliteevski, Exciton-light coupling in single and coupled semiconductor microcavities: Polariton dispersion and polarization splitting, Physical Review B **59**, 5082 (1999).

[50] S. Schumacher, N. H. Kwong, and R. Binder, Influence of exciton-exciton correlations on the polarization characteristics of polariton amplification in semiconductor microcavities, Physical Review B **76**, 245324 (2007).

[51] M. Wouters and I. Carusotto, Excitations in a Nonequilibrium Bose-Einstein Condensate of Exciton Polaritons, Physical Review Letters **99**, 140402 (2007).

[52] F. Manni, K. G. Lagoudakis, T. C. H Liew, R. André, V. Savona, and B. Deveaud, Dissociation dynamics of singly charged vortices into half-quantum vortex pairs, Nature Communications **3**, 1309 (2012).

[53] A. Askitopoulos, K. Kalinin, T. C. H. Liew, P. Cilibrizzi, Z. Hatzopoulos, P. G. Savvidis, N. G. Berloff, and P. G. Lagoudakis, Nonresonant optical control of a spinor polariton condensate, Physical Review B **93**, 205307 (2016).

[54] F. Manni, K. G. Lagoudakis, T. C. H. Liew, R. André, and B. Deveaud-Plédran, Spontaneous Pattern Formation in a Polariton Condensate, Physical Review Letters **107**, 106401 (2011).

[55] G. Roumpos, M. D. Fraser, A. Löffler, S. Höfling, A. Forchel, and Y. Yamamoto, Single vortex–antivortex pair in an exciton-polariton condensate, Nature Physics **7**, 129 (2011).

[56] R. Dall, M. D. Fraser, A. S. Desyatnikov, G. Li, S. Brodbeck, M. Kamp, C. Schneider, S. Höfling, and E. A. Ostrovskaya, Creation of Orbital Angular Momentum States with Chiral Polaritonic Lenses, Physical Review Letters **113**, 200404 (2014).

[57] M. Wouters, I. Carusotto, and C. Ciuti, Spatial and spectral shape of inhomogeneous nonequilibrium exciton-polariton condensates, Physical Review B **77**, 115340 (2008).

[58] P. Cristofolini, A. Dreismann, G. Christmann, G. Franchetti, N. G. Berloff, P. Tsotsis, Z. Hatzopoulos, P. G. Savvidis, and J. J. Baumberg, Optical Superfluid Phase Transitions and Trapping of Polariton Condensates, Physical Review Letters **110**, 186403 (2013).

[59] M. Wouters and V. Savona, Stochastic classical field model for polariton condensates, Physical Review B **79**, 165302 (2009).

[60] H. Haug, T. D. Doan, and D. B. Tran Thoai, Quantum kinetic derivation of the nonequilibrium Gross-Pitaevskii equation for nonresonant excitation of microcavity polaritons, Physical Review B **89**, 155302 (2014).

[61] C. Sturm, D. Solnyshkov, O. Krebs, A. Lemaître, I. Sagnes, E. Galopin, A. Amo, G. Malpuech, and J. Bloch, Nonequilibrium polariton condensate in a magnetic field, Physical Review B **91**, 155130 (2015).

[62] G. Li, T. C. H. Liew, O. A. Egorov, and E. A. Ostrovskaya, Incoherent excitation and switching of spin states in exciton-polariton condensates, Physical Review B **92**, 064304 (2015).

[63] A. Sinatra, C. Lobo, and Y. Castin, The truncated Wigner method for Bose-condensed gases: Limits of validity and applications, Journal of Physics B: Atomic, Molecular and Optical Physics **35**, 3599 (2002).

[64] P. B. Blakie, A. S. Bradley, M. J. Davis, R. J. Ballagh, and C. W. Gardiner, Dynamics and statistical mechanics of ultra-cold Bose gases using c-field techniques, Advances in Physics **57**, 363 (2008).

[65] B. Opanchuk and P. D. Drummond, Functional Wigner representation of quantum dynamics of Bose-Einstein condensate, Journal of Mathematical Physics **54**, 042107 (2013).

[66] N. Bobrovska and M. Matuszewski, Adiabatic approximation and fluctuations in exciton-polariton condensates, Physical Review B **92**, 035311 (2015).

[67] M. J. Steel, M. K. Olsen, L. I. Plimak, P. D. Drummond, S. M. Tan, M. J. Collett, D. F. Walls, and R. Graham, Dynamical quantum noise in trapped Bose-Einstein condensates, Physical Review A **58**, 4824 (1998).

[68] A. Verger, I. Carusotto, and C. Ciuti, Quantum Monte Carlo study of ring-shaped polariton parametric luminescence in a semiconductor microcavity, Physical Review B **76**, 115324 (2007).

[69] J. D. Sau, S. R. Leslie, D. M. Stamper-Kurn, and M. L. Cohen, Theory of domain formation in inhomogeneous ferromagnetic dipolar condensates within the truncated Wigner approximation, Physical Review A **80**, 023622 (2009).

[70] D. Gerace and I. Carusotto, Analog Hawking radiation from an acoustic black hole in a flowing polariton superfluid, Physical Review B **86**, 144505 (2012).

[71] A. Zamora, G. Dagvadorj, P. Comaron, I. Carusotto, N. P. Proukakis, and M. H. Szymańska, Kibble-Zurek Mechanism in Driven Dissipative Systems Crossing a Nonequilibrium Phase Transition, Physical Review Letters **125**, 095301 (2020).

[72] A. M. C. Dawes, L. Illing, S. M. Clark, and D. J. Gauthier, All-optical switching in rubidium vapor, Science **308**, 672 (2005).

[73] X. Hu, P. Jiang, C. Ding, H. Yang, and Q. Gong, Picosecond and low-power all-optical switching based on an organic photonic-bandgap microcavity, Nature Photonics **2**, 185 (2008).

[74] T. Tanabea, M. Notomi, S. Mitsugi, A. Shinya, and E. Kuramochi, All-optical switches on a silicon chip realized using photonic crystal nanocavities, Applied Physics Letters **87**, 151112 (2005).

[75] T. Volz, A. Reinhard, M. Winger, A. Badolato, K. J. Hennessy, E. L. Hu, and A. İmamoğlu, Ultrafast all-optical switching by single photons, Nature Photonics **6**, 605 (2012).

[76] A. Amo, T. Liew, C. Adrados, R. Houdré, E. Giacobino, A. V. Kavokin, and A. Bramati, Exciton–polariton spin switches, Nature Photonics **4**, 361 (2010).

[77] D. Ballarini, M. De Giorgi, E. Cancellieri, R. Houdré, E. Giacobino, R. Cingolani, A. Bramati, G. Gigli, and D. Sanvitto, All-optical polariton transistor, Nature Communications **4**, 1778 (2013).

[78] M. C. Cross and P. C. Hohenberg, Pattern formation outside of equilibrium, Reviews of Modern Physics **65**, 851 (1993).

[79] H. Saito, T. Aioi, and T. Kadokura, Order-Disorder Oscillations in Exciton-Polariton Superfluids, Physical Review Letters **110**, 026401 (2013).

[80] A. Werner, O. A. Egorov, and F. Lederer, Exciton-polariton patterns in coherently pumped semiconductor microcavities, Physical Review B **89**, 245307 (2014).

[81] S. M. H. Luk, H. Vergnet, O. Lafont, P. Lewandowski, N. H. Kwong, E. Galopin, A. Lemaitre, P. Roussignol, J. Tignon, S. Schumacher, R. Binder, and E. Baudin, All-Optical Beam Steering Using the Polariton Lighthouse Effect, ACS Photonics **8**, 449 (2021).

[82] M. Pukrop (2018), Pattern Formation and Optical Control in Semiconductor Microcavities, (Unpublished Master's Thesis), Paderborn University.

[83] M. Pukrop and S. Schumacher, Externally controlled Lotka-Volterra dynamics in a linearly polarized polariton fluid, Physical Review E **101**, 012207 (2020).

[84] P. Lewandowski, O. Lafont, E. Baudin, C. K. P. Chan, P. T. Leung, S. M. H. Luk, E. Galopin, A. Lemaître, J. Bloch, J. Tignon, P. Roussignol, N. H. Kwong, R. Binder, and S. Schumacher, Polarization dependence of nonlinear wave mixing of spinor polaritons in semiconductor microcavities, Physical Review B **94**, 045308 (2016).

[85] Y. C. Tse, C. K. P. Chan, M. H. Luk, N. H. Kwong, P. T. Leung, R. Binder, and S. Schumacher, A population-competition model for analyzing transverse optical patterns including optical control and structural anisotropy, New Journal of Physics **17**, 083054 (2015).

[86] S. Wiggins, *Introduction to Applied Nonlinear Dynamical Systems and Chaos*, Texts in Applied Mathematics (Springer, New York, 2003).

[87] S. H. Strogatz, *Nonlinear Dynamics and Chaos: With Applications to Physics, Biology, Chemistry and Engineering* (Westview Press, Cambridge, Massachusetts, 2000).

[88] L. Brenig, Complete factorisation and analytic solutions of generalized Lotka-Volterra equations, Physics Letters A **133**, 378 (1988).

[89] J. Hofbauer, K. Sigmund et al., *The Theory of Evolution and Dynamical Systems: Mathematical Aspects of Selection* (Cambridge University Press, Cambridge, 1988).

[90] B. Hernández-Bermejo and V. Fairén, Lotka-Volterra representation of general nonlinear systems, Mathematical Biosciences **140**, 1 (1997).

[91] W. E. Lamb, Jr., Theory of an Optical Maser, Physical Review **134**, A1429 (1964).

[92] R. H. Hering, Oscillations in Lotka-Volterra systems of chemical reactions, Journal of Mathematical Chemistry **5**, 197 (1990).

[93] P. J. Wangersky, Lotka-Volterra population models, Annual Review of Ecology and Systematics **9**, 189 (1978).

[94] R. M. Goodwin, A growth cycle, in *Essays in Economic Dynamics* (Macmillan, London, 1982), pp. 165–170.

[95] J. Roughgarden, *Theory of Population Genetics and Evolutionary Ecology: An Introduction*, (Macmillan, London, 1979).

[96] P. Chesson, Mechanisms of Maintenance of Species Diversity, Annual Review of Ecology and Systematics **31**, 343 (2000).

[97] P. Chesson and J. J. Kuang, The interaction between predation and competition, Nature **456**, 235 (2008).

[98] T. Namba, Bifurcation phenomena appearing in the Lotka-Volterra competition equations: a numerical study, Mathematical Biosciences **81**, 191 (1986).

[99] B. S. Othman, Method of Centre Manifold from Bifurcation Theory, International Journal of Scientific Research and Management **7**, 173 (2019).

[100] Y. Huang, MATH44041/64041: Applied Dynamical Systems, Lecture notes (2019).

[101] K. V. I. Saputra, L. van Veen, and G. R. W. Quispel, The saddle-node-transcritical bifurcation in a population model with constant rate harvesting, Lotka-Volterra representation of general nonlinear systems, Discrete & Continuous Dynamical Systems B **14**, 233 (2010).

[102] B. Buchberger, Ein algorithmisches Kriterium für die Lösbarkeit eines algebraischen Gleichungssystems, Aequationes Mathematicae **4**, 374 (1970).

[103] A. Dhooge, W. Govaerts, and Y. A. Kuznetsov, MATCONT: A MATLAB package for numerical bifurcation analysis of ODEs, ACM Transactions on Mathematical Software **29**, 141 (2003).

[104] K. G. Lagoudakis, M. Wouters, M. Richard, A. Baas, I. Carusotto, R. André, L. S. Dang, and B. Deveaud-Plédran, Quantized vortices in an exciton–polariton condensate, Nature Physics **4**, 706 (2008).

[105] K. G. Lagoudakis, F. Manni, B. Pietka, M. Wouters, T. C. H. Liew, V. Savona, A. V. Kavokin, R. André, and B. Deveaud-Plédran, Probing the Dynamics of Spontaneous Quantum Vortices in Polariton Superfluids, Physical Review Letters **106**, 115301 (2011).

[106] N. B. Baranova, A. V. Mamaev, N. F. Pilipetsky, V. V. Shkunov, and B. Y. Zel'dovich, Wave-front dislocations: topological limitations for adaptive systems with phase conjugation, Journal of the Optical Society of America **73**, 525 (1983).

[107] L. Allen, M. W. Beijersbergen, R. J. C. Spreeuw, and J. P. Woerdman, Orbital angular momentum of light and the transformation of Laguerre-Gaussian laser modes, Physical Review A **45**, 8185 (1992).

[108] I. V. Basistiy, M. S. Soskin, and M. V. Vasnetsov, Optical wavefront dislocations and their properties, Optics Communications **119**, 604 (1995).

[109] L. Dominici, R. Carretero-González, A. Gianfrate, J. Cuevas-Maraver, A. S. Rodrigues, D. J. Frantzeskakis, G. Lerario, D. Ballarini, M. De Giorgi, G. Gigli, P. G. Kevrekidis, and D. Sanvitto , Interactions and scattering of quantum vortices in a polariton fluid, Nature Communications **9**, 1467 (2018).

[110] X. Ma and S. Schumacher, Vortex-vortex control in exciton-polariton condensates, Physical Review B **95**, 235301 (2017).

[111] E. A. Ostrovskaya, J. Abdullaev, A. S. Desyatnikov, M. D. Fraser, and Y. S. Kivshar, Dissipative solitons and vortices in polariton Bose-Einstein condensates, Physical Review A **86**, 013636 (2012).

[112] A. Askitopoulos, H. Ohadi, A. V. Kavokin, Z. Hatzopoulos, P. G. Savvidis, and P. G. Lagoudakis, Polariton condensation in an optically induced two-dimensional potential, Physical Review B **88**, 041308(R) (2013).

[113] E. Estrecho, T. Gao, N. Bobrovska, D. Comber-Todd, M. D. Fraser, M. Steger, K. West, L. N. Pfeiffer, J. Levinsen, M. M. Parish, T. C. H. Liew, M. Matuszewski, D. W. Snoke, A. G. Truscott, and E. A. Ostrovskaya, Direct measurement of polariton-

polariton interaction strength in the Thomas-Fermi regime of exciton-polariton condensation, Physical Review B **100**, 035306 (2019).

[114] X. Ma, U. Peschel, and O. A. Egorov, Incoherent control of topological charges in nonequilibrium polariton condensates, Physical Review B **93**, 035315 (2016).

[115] B. Berger, D. Schmidt, X. Ma, S. Schumacher, C. Schneider, S. Höfling, and M. Aßmann, Formation dynamics of exciton-polariton vortices created by nonresonant annular pumping, Physical Review B **101**, 245309 (2020).

[116] X. Ma, B. Berger, M. Aßmann, R. Driben, T. Meier, C. Schneider, S. Höfling, and S. Schumacher, Realization of all-optical vortex switching in exciton-polariton condensates, Nature Communications **11**, 897 (2020).

[117] B. Berger, M. Kahlert, D. Schmidt, and M. Aßmann, Spectroscopy of fractional orbital angular momentum states, Optics Express **26**, 32248 (2018).

[118] T. C. H. Liew, Y. G. Rubo, and A. V. Kavokin, Generation and Dynamics of Vortex Lattices in Coherent Exciton-Polariton Fields, Physical Review Letters **101**, 187401 (2008).

[119] K. G. Lagoudakis, T. Ostatnický, A. V. Kavokin, Y. G. Rubo, R. André, and B. Deveaud-Plédran, Observation of half-quantum vortices in an exciton-polariton condensate, Science **326**, 974 (2009).

[120] F. Manni, Y. Léger, Y. G. Rubo, R. André, and B. Deveaud, Hyperbolic spin vortices and textures in exciton–polariton condensates, Nature Communications **4**, 2590 (2013).

[121] T. C. H. Liew, O. A. Egorov, M. Matuszewski, O. Kyriienko, X. Ma, and E. A. Ostrovskaya, Instability-induced formation and nonequilibrium dynamics of phase defects in polariton condensates, Physical Review B **91**, 085413 (2015).

[122] L. Dominici, G. Dagvadorj, J. M. Fellows, D. Ballarini, M. De Giorgi, F. M. Marchetti, B. Piccirillo, L. Marrucci, A. Bramati, G. Gigli, M. H. Szymańska, and D. Sanvitto, Vortex and half-vortex dynamics in a nonlinear spinor quantum fluid, Science Advances **1**, e1500807 (2015).

[123] B. Ramachandhran, B. Opanchuk, X.-J. Liu, H. Pu, P. D. Drummond, and H. Hu, Half-quantum vortex state in a spin-orbit-coupled Bose-Einstein condensate, Physical Review A **85**, 023606 (2012).

[124] V. E. Lobanov, Y. V. Kartashov, and V. V. Konotop, Fundamental, Multipole, and Half-Vortex Gap Solitons in Spin-Orbit Coupled Bose-Einstein Condensates, Physical Review Letters **112**, 180403 (2014).

[125] S. W. Seo, S. Kang, W. J. Kwon, and Y. Shin, Half-Quantum Vortices in an Antiferromagnetic Spinor Bose-Einstein Condensate, Physical Review Letters **115**, 015301 (2015).

[126] S. W. Seo, W. J. Kwon, S. Kang, and Y. Shin, Collisional Dynamics of Half-Quantum Vortices in a Spinor Bose-Einstein Condensate, Physical Review Letters **116**, 185301 (2016).

[127] J. Jang, D. G. Ferguson, V. Vakaryuk, R. Budakian, S. B. Chung, P. M. Goldbart, and Y. Maeno, Observation of Half-Height Magnetization Steps in $Sr_2RuO_4$, Science **331**, 186 (2011).

[128] M. M. Salomaa and G. E. Volovik, Half-Quantum Vortices in Superfluid $^3$He-A, Physical Review Letters **55**, 1184 (1985).

[129] S. Autti, V. V. Dmitriev, J. T. Mäkinen, A. A. Soldatov, G. E. Volovik, A. N. Yudin, V. V. Zavjalov, and V. B. Eltsov, Observation of Half-Quantum Vortices in Topological Superfluid $^3$He, Physical Review Letters **117**, 255301 (2016).

[130] X. Ma and S. Schumacher, Vortex Multistability and Bessel Vortices in Polariton Condensates, Physical Review Letters **121**, 227404 (2018).

[131] M. Pukrop, S. Schumacher, and X. Ma, Circular polarization reversal of half-vortex cores in polariton condensates, Physical Review B **101**, 205301 (2020).

[132] V. E. Lobanov, Y. V. Kartashov, V. A. Vysloukh, and L. Torner, Stable radially symmetric and azimuthally modulated vortex solitons supported by localized gain, Optics Letters **36**, 85 (2011).

[133] M. D. Fraser, G. Roumpos, and Y. Yamamoto, Vortex–antivortex pair dynamics in an exciton–polariton condensate, New Journal of Physics **11**, 113048 (2009).

[134] H. Flayac, I. A. Shelykh, D. D. Solnyshkov, and G. Malpuech, Topological stability of the half-vortices in spinor exciton-polariton condensates, Physical Review B **81**, 045318 (2010).

[135] M. Toledo-Solano and Y. G. Rubo, Comment on "Topological stability of the half-vortices in spinor exciton-polariton condensates", Physical Review B **82**, 127301 (2010).

[136] H. Flayac, D. D. Solnyshkov, G. Malpuech, and I. A. Shelykh, Reply to "Comment on 'Topological stability of the half-vortices in spinor exciton-polariton condensates'", Physical Review B **82**, 127302 (2010).

[137] M. Toledo-Solano, M. E. Mora-Ramos, A. Figueroa, and Y. G. Rubo, Warping and interactions of vortices in exciton-polariton condensates, Physical Review B **89**, 035308 (2014).

[138] D. R. Gulevich, D. V. Skryabin, A. P. Alodjants, and I. A. Shelykh, Topological spin Meissner effect in spinor exciton-polariton condensate: Constant amplitude solutions, half-vortices, and symmetry breaking, Physical Review B **94**, 115407 (2016).

[139] M. Schneider, H. Hoffmann, and J. Zweck, Magnetic switching of single vortex permalloy elements, Applied Physics Letters **79**, 3113 (2001).

[140] Q. F. Xiao, J. Rudge, and B. C. Choi, Dynamics of vortex core switching in ferromagnetic nanodisks, Applied Physics Letters **89**, 262507 (2006).

[141] R. Hertel, S. Gliga, M. Fähnle, and C. M. Schneider, Ultrafast Nanomagnetic Toggle Switching of Vortex Cores, Physical Review Letters **98**, 117201 (2007).

[142] K. Yamada, S. Kasai, Y. Nakatani, K. Kobayashi, H. Kohno, A. Thiaville, and T. Ono, Electrical switching of the vortex core in a magnetic disk, Nature Materials **6**, 207 (2007).

[143] D. N. Krizhanovskii, D. M. Whittaker, R. A. Bradley, K. Guda, D. Sarkar, D. Sanvitto, L. Vina, E. Cerda, P. Santos, K. Biermann, R. Hey, and M. S. Skolnick, Effect of Interactions on Vortices in a Nonequilibrium Polariton Condensate, Physical Review Letters **104**, 126402 (2010).

[144] K. Guda, M. Sich, D. Sarkar, P. M. Walker, M. Durska, R. A. Bradley, D. M. Whittaker, M. S. Skolnick, E. A. Cerda-Méndez, P. V. Santos, K. Biermann, R. Hey, and D. N. Krizhanovskii, Spontaneous vortices in optically shaped potential profiles in semiconductor microcavities, Physical Review B **87**, 081309 (2013).

[145] M. Vladimirova, S. Cronenberger, D. Scalbert, K. V. Kavokin, A. Miard, A. Lemaître, J. Bloch, D. Solnyshkov, G. Malpuech, and A. V. Kavokin, Polariton-polariton interaction constants in microcavities, Physical Review B **82**, 075301 (2010).

[146] N. Takemura, S. Trebaol, M. Wouters, M. T. Portella-Oberli, and B. Deveaud, Heterodyne spectroscopy of polariton spinor interactions, Physical Review B **90**, 195307 (2014).

[147] A. Streltsov, G. Adesso, and M. B. Plenio, Colloquium: Quantum coherence as a resource, Reviews of Modern Physics **89**, 041003 (2017).

[148] E. Chitambar and G. Gour, Quantum resource theories, Reviews of Modern Physics **91**, 025001 (2019).

[149] F. P. Laussy, G. Malpuech, A. Kavokin, and P. Bigenwald, Spontaneous Coherence Buildup in a Polariton Laser, Physical Review Letters **93**, 016402 (2004).

[150] J. Keeling, F. M. Marchetti, M. H. Szymańska, and P. B. Littlewood, Collective coherence in planar semiconductor microcavities, Semiconductor Science and Technology **22**, R1 (2007).

[151] A. P. D. Love, D. N. Krizhanovskii, D. M. Whittaker, R. Bouchekioua, D. Sanvitto, S. Al Rizeiqi, R. Bradley, M. S. Skolnick, P. R. Eastham, R. André, and L. S. Dang, Intrinsic Decoherence Mechanisms in the Microcavity Polariton Condensate, Physical Review Letters **101**, 067404 (2008).

[152] T. Horikiri, P. Schwendimann, A. Quattropani, S. Höfling, A. Forchel, and Y. Yamamoto, Higher order coherence of exciton-polariton condensates, Physical Review B **81**, 033307 (2010).

[153] A. F. Adiyatullin, M. D. Anderson, P. V. Busi, H. Abbaspour, R. André, M. T. Portella-Oberli, and B. Deveaud, Temporally resolved second-order photon correlations of exciton-polariton Bose–Einstein condensate formation, Applied Physical Letters **107**, 221107 (2015).

[154] M. Klaas, E. Schlottmann, H. Flayac, F. P. Laussy, F. Gericke, M. Schmidt, M. v. Helversen, J. Beyer, S. Brodbeck, H. Suchomel, S. Höfling, S. Reitzenstein, and C. Schneider, Photon-Number-Resolved Measurement of an Exciton-Polariton Condensate, Physical Review Letters **121**, 047401 (2018).

[155] J. A. Hansen and C. Penland, Efficient Approximate Techniques for Integrating Stochastic Differential Equations, Monthly Weather Review **134**, 3006 (2006).

[156] T. Baumgratz, M. Cramer, and M. B. Plenio, Quantifying Coherence, Physical Review Letters **113**, 140401 (2014).

[157] W. Vogel and D.-G. Welsch, *Quantum Optics, third edition* (Wiley-VCH Verlag, Weinheim, 2006).

[158] J. Sperling and I. A. Walmsley, Quasiprobability representation of quantum coherence, Physical Review A **97**, 062327 (2018).

[159] D. F. McAlister and M. G. Raymer, Ultrafast photon-number correlations from dual-pulse, phase-averaged homodyne detection, Physical Review A **55**, R1609 (1997).

[160] G. Roumpos and S. T. Cundiff, Multichannel homodyne detection for quantum optical tomography, Journal of the Optical Society of America B **30**, 1303 (2013).

[161] J. Keeling and N. G. Berloff, Spontaneous Rotating Vortex Lattices in a Pumped Decaying Condensate, Physical Review Letters **100**, 250401 (2008).

[162] M. Richard, J. Kasprzak, R. Romestain, R. André, and L. S. Dang, Spontaneous Coherent Phase Transition of Polaritons in CdTe Microcavities, Physical Review Letters **94**, 187401 (2005).

[163] G. M. D'Ariano, U. Leonhardt, and H. Paul, Homodyne detection of the density matrix of the radiation field, Physical Review A **52**, R1801 (1995).

[164] U. Leonhardt, H. Paul, and G. M. D'Ariano, Tomographic reconstruction of the density matrix via pattern functions, Physical Review A **52**, 4899 (1995).

[165] T. Richter, Pattern functions used in tomographic reconstruction of photon statistics revisited, Physics Letters A **211**, 327 (1996).

[166] U. Leonhardt, M. Munroe, T. Kiss, T. Richter, and M. G. Raymer, Sampling of photon statistics and density matrix using homodyne detection, Optics Communications **127**, 144 (1996).

[167] A. I. Lvovsky and M. G. Raymer, Continuous-variable optical quantum-state tomography, Reviews of Modern Physics **81**, 299 (2009).

[168] D.-G. Welsch, W. Vogel, T. Opatrny, Homodyne Detection and Quantum State Reconstruction, Progress in Optics, Vol. XXXIX, ed. E. Wolf (Elsevier, Amsterdam, 1999), p. 63–211.

[169] J. Sperling, (private communication, 2021).

[170] K. E. Cahill and R. J. Glauber, Density Operators and Quasiprobability Distributions, Physical Review **177**, 1882 (1969).

[171] J. Sperling, W. Vogel, and G. S. Agarwal, Quantum state engineering by click counting, Physical Review A **89**, 043829 (2014).

[172] F. Arecchi, A. Berne, A. Sona and P. Burlamacchi, 1A4 - Photocount distributions and field statistics, IEEE Journal of Quantum Electronics **2**, 341 (1966).

[173] B. Berg, L. I. Plimak, A. Polkovnikov, M. K. Olsen, M. Fleischhauer, and W. P. Schleich, Commuting Heisenberg operators as the quantum response problem: Time-normal averages in the truncated Wigner representation, Physical Review A **80**, 033624 (2009).

# Danksagung

Ich bedanke mich bei Stefan Schumacher für die Möglichkeit zu dieser Arbeit in einem spannenden Themenbereich und seine intensive Betreuung sowie unserer ganzen Arbeitsgruppe für die Unterstützung. Insbesondere danke ich Xuekai Ma für die schöne Zusammenarbeit und seine große Hilfbereitschaft. Außerdem danke ich dem zweiten Gutachter Torsten Meier. Für die erfolgreiche Kooperation, Unterstützung und wertvolle Diskussionen danke ich Jan Sperling von der Universität Paderborn sowie Carolin Lüders und Marc Aßmann von der Technischen Universität Dortmund.